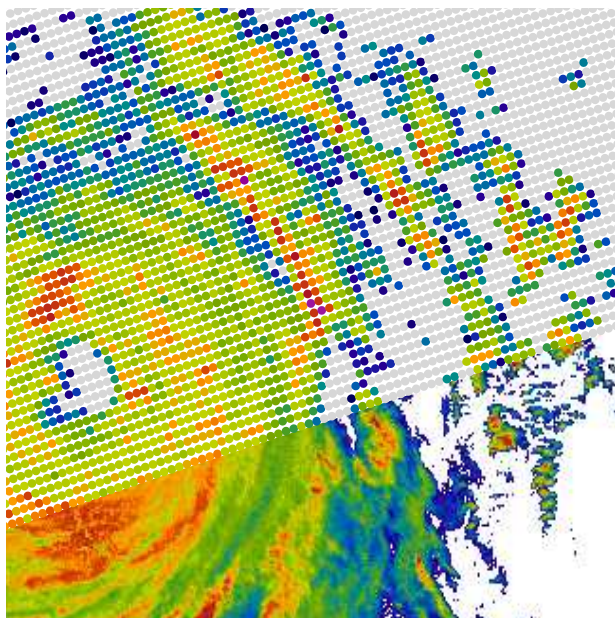# A study of the structure of radar rainfall and its errors

Tesi Doctoral
Programa d'Enginyeria Civil
Universitat Politècnica de Catalunya
Juny 2010

Autor: Xavier Llort i Pavon
Director de Tesi: Daniel Sempere Torres
Codirector de Tesi: Marc Berenguer i Ferrer

Centre de Recerca Aplicada en Hidrometeorologia
UNIVERSITAT POLITÈCNICA DE CATALUNYA

A la meva àvia

Agraïments

Aquesta tesi és el final d'un camí molt llarg i, en aquests moments al mirar enrere, me n'adono de la gran quantitat de gent que en major o menor mesura hi ha influït o contribuït. Fer una llista exhaustiva resulta realment complicat, però sí que hi ha un seguit de persones que m'agradaria anomenar.

En primer lloc m'agradaria donar les gràcies a en Daniel Sempere, director de la tesi. En tot moment ha fet el possible per a què el treball tirés endavant. La seva il·lusió per la feina ben feta, estusiasme i empenta inesgotable (i encomanadissa) han estat claus per a què aquesta tesi hagi arribat al final. També voldria agrair que s'hagi preocupat per mi, avantposant sempre la persona a la feina. De la mateixa manera vull agrair a en Marc Berenguer, codirector de la tesi, el seu ajut al llarg de tot el període, i sobretot en la recta final.

També m'agradaria agrair a tothom del CRAHI (o GRAHI) i HYDS la seva ajuda al llarg d'aquest període, en especial a en Rafa, de qui en vaig apendre molt els primers anys i sempre ha estat un referent a seguir; i als companys de doctorat Carles, Marc, Maria i Carlos que hagin estat sempre disposats a ajudar compartint el seu temps i coneixements. Al llarg d'aquests anys la relació amb els *informàtics* del CRAHI, HYDS i UPC ha fet que fossin molt més que companys de feina i s'integressin a la meva vida privada, especialment a en David F., Mercè, David L., Miquel Àngel, Antonio, Jordi G., René i Núria, els hi dec més que el temps que m'han dedicat. A la Montse i la Mireia també que sempre m'hagin ajudat en tots els sentits.

L'any 2003 vaig tenir l'oportunitat de realitzar una estada al Goddard Space Flight Center de la NASA, a Washington. M'agradaria agrair a l'Eyal Amitai la seva acollida a tots nivells. Va ser una oportunitat única per apendre i conèixer món. També aprecio que després de l'estada sempre hagi estat disposat a continuar col·laborant i discutir resultats. De la mateixa manera, l'any 2007 vaig realitzar una estada a McGill University, a Montreal. Aquí vull agrair a l'Isztar Zawadzki el seu temps i acollida; i a en Marc Berenguer de nou el seu suport.

També vull agrair el temps que en Geoff Pegram m'ha dedicat en les seves visites a Barcelona, que sempre hagi estat disposat a discutir idees entusiasmat, i la revisió de la primera versió d'aquest document.

Abstract

The principal objectives of this thesis are two: on one hand study the structure of the precipitation's variability at different spatial and temporal scales, and on the other hand study the structure of the errors in the quantitative precipitation estimates by radar.

In relation to the precipitation structure, a comparison framework for downscaling methods is proposed. Within this framework, the capability of each method reproducing the variability and multifractal behaviour observed in rainfall can be tested. A three-dimensional downscaling method to generate high-resolution precipitation fields from radar observations is proposed. The method is capable to reproduce the variability of rainfall at all scales and, at the same time, preserve the vertical structure of precipitation observed by the radar.

In this thesis the structure of the errors that remain after the correction chain in radar measurements (both ground- and space-borne) is also studied. Simulation of the radar physical measurement process over high-resolution precipitation fields is performed to characterize the error related with range. The overall error in quantitative precipitation estimates by radar is characterized through comparison of radar estimates with a reference product based on a radar-raingauges merging. The error structure is used to generate a radar ensemble of precipitation estimates that represents the uncertainty in the measurements and can be used in probabilistic applications.

Regarding the study of the errors associated to spaceborne radar measurements, comparisons of TRMM Precipitation Radar with ground equipment are performed to characterize the discrepancies between the precipitation estimates under different conditions.

Resum

Els objectius principals d'aquesta tesi són dos: d'una banda estudiar l'estructura de la variabilitat de la precipitació a diferents escales espacials i temporals, i de l'altra, estudiar l'estructura dels errors en les estimacions quantitatives de precipitació a través de radar.

Pel que fa a l'estudi de l'estructura de la precipitació es proposa un marc de comparació per a mètodes de downscaling basat en valorar el grau amb què cada mètode és capaç de reproduir la variabilitat observada a les diferents escales de la pluja i la seva estructura multifractal. Finalment es proposa un mètode de downscaling tridimensional per a generar camps de precipitació d'alta resolució. Partint de dades mesurades amb radar, és capaç de reproduir la variabilitat a totes les escales de la pluja, i a la vegada, conservar l'estructura vertical de la precipitació observada pel radar.

En aquesta tesi s'estudia també l'estructura dels errors associats a les mesures de radar, tant terrestre com embarcat en satèl·lit, que queden després de la cadena de correcció. Es realitza un estudi mitjançant simulació física de les observacions del radar, sobre un camp de precipitació d'alta resulució, per caracteritzar l'error relacionat amb la distància d'observació. També es caracteritza l'error total en les estimacions quantitatives de pluja dels radars terrestres mitjançant comparació contra un producte de referència basat en la combinació de radar i pluviòmetres. L'estructura de l'error trobada ha estat usada per generar un ensemble d'estimacions de pluja, que representa la incertesa en les estimacions, i pot ser emprat per aplicacions probabilístiques.

Pel que fa a l'estudi de l'estructura de l'error associat a les estimacions de radar embarcat en satèl·lit, s'han realitzat comparacions del radar embarcat en el satèl·lit TRMM contra equipament terrestre, per tal de caracteritzar, sota diverses condicions, les diferències en les mesures de precipitació.

Contents

CHAPTER 1

Introduction

1.1. General context

Water is necessary for life. Water is, with no doubt, the natural element that most influences and determines our society. All civilizations emerged in places where fresh water was available, its lack determined the end of empires, and still nowadays the availability of this element is a key point for the development of human communities.

Precipitation is one of the driving forces of the water cycle, and probably the one having greatest impact in everyday life. Rainfall can be received as a gift if water is needed, or as a punishment if it is too abundant and produces hazards. In an attempt to control its variability, infrastructures are built to store water for dry periods, and to prevent the potential damages of its abundance.

Precipitation is the fruit of the combination of numerous physical processes operating over a variety of scales in space and time. Precipitation can range from convective cells (extension of 1-10 km², and lifetimes of minutes) to frontal systems (extension of 10^4 km², and lifetimes of several days), all exhibiting a non-linear behaviour.

Several instruments have been developed to measure precipitation. Raingauges maybe the simplest, consisting in directly measuring the rainfall that falls into a small area of about 200 cm². Raingauges are point measurements that due to the variability of precipitation might not be representative of a large area and therefore not much useful for some applications. Despite networks of raingagues have been designed to increase the coverage and representativeness of their measurements, a large density would be necessary for some applications (one gauge every 50 km² for hydrological modelling (Sempere-Torres *et al.* 1999), one gauge per every 2 km² in the case of urban areas (Berne *et al.* 2004). This density however is rarely achieved in operational networks, for example, in Spain, the Sistema Automático de Información Hidrológica (SAIH) has an average density of one gauge every 300 km² with a maximum density of one gauge every 200 km².

To overcome the coverage limitations of raingauge networks one interesting instrument is the weather radar. Radars (developed for military uses in the World War II) remotely measure precipitation with a relatively high spatial and temporal resolution (around 2 km² and 10 minutes) up to a certain range (around 150 km) from the radar site. Usually this instrument measures at several elevation angles to obtain a volumetric scan of the atmosphere. The fact that this instrument does not measure precipitation directly (retrieves reflectivity of the intercepted objects) and that experiences several sources of error (signal attenuation, ground clutter, vertical variability of precipitation, etc. Zawadzki 1984) make its uses in Quantitative Precipitation Estimation [QPE] still limited. Several algorithms and also methodologies of radar-raingauge combination have been developed to improve the radar QPE estimates.

Similarly to what happened with raingauges, radar networks have been deployed to overcome the limitation of single radars used individually. In the United States the NEXRAD network (with 158 weather radars) covers all the country providing a rainfall field over the Continental part every 5 minutes with a resolution of 1 km². In Spain, the Spanish Meteorology Agency [AEMET] has 15 C-band radars to cover the country, and in Catalonia, the Servei Meteorologic de Catalunya [SMC] has a network of 4 C-band radars, which makes Catalonia a really high radar covered area.

A last step in the precipitation measurement is the use of satellite platforms. Many satellites have onboard radiometers (passive instruments) that can retrieve precipitation information, but since 1997 there is also the Tropical Rainfall Measurement Mission [TRMM] satellite (Simpson *et al.* 1988) which, in addition to the radiometers, also carries a Precipitation Radar onboard. TRMM covers between 35º S and 35º N with an average revisit time of 9 hours. The Global Precipitation Mission [GPM] is a TRMM follow-on mission that will be launched in 2013, and will increase spaceborne radar coverage up to the latitudinal range of 70ºS-70ºN with a shorter revisit time facing new challenges, like large areas dominated by light rain and snow.

Satellite platforms can provide global coverage and therefore precipitation estimates where no other instruments can (like oceans and large portions of inhabited land) which is useful in global climate models and many other applications. But at the same time, satellites have many limitations in the instruments design (size, weight, and resolution) that affect their measures.

To get the "best" rainfall field in the sense that it better represents the truth, ideally all the observations from the different instruments should be merged taking the better of each one of them. The structure of precipitation (temporal and spatial variability) influences in the measurements of all these instruments –each one of them observing at deferens scales–, and makes difficult their intercomparison and therefore their blending.

At the same time, regardless of all the efforts devoted to correct the radar precipitation retrievals (both from ground- and space-borne radars) by its characteristic problems (which in real-time

applications not always can be done as well as it could be), there is an uncertainty in the measurements.

This thesis deals with these two related subjects: the structure of precipitation and the characterization of the uncertainty in the radar measurements.

1.2. Structure of precipitation and scaling properties.

As mentioned above, precipitation is the product of the combination of numerous physical processes operating over a variety of scales in space and time that can range from few square kilometres and minutes to large extensions and days. Precipitation exhibits variability over a wide range of scales (Lima 1998; Fabry 1996; Lovejoy *et al.* 2008), and these temporal and spatial variability of precipitation are important in many studies (e.g. for comparing or combining instrument measures operating at different scales, for simulation of rainfall series, etc.).

Scaling properties (or what is the same: variability properties behaviour over the scales) can be investigated using fractal and multifractal theories. Fractal theory (Mandelbrot 1982) supposes that variability properties do not change with scale and try to describe complex phenomena by few scaling parameters. Multifractal theory (Hentschel and Procaccia 1983) is more general than fractals and allow for other behaviours rather than simple scaling.

The scaling properties of rainfall have an impact that is not always taken into account on applications such as the comparison or merging precipitation estimates retrieved by different instruments having different scales of observation. At the same time, simulating rainfall with the correct scaling properties at higher resolution than observed (*downscaling*) is useful for many quantitative applications of precipitation data:

- Enhancing the resolution of climate model outputs.

- Assessing the hydrological risk/water resources in small areas using Numerical Weather Prediction [NWP] or climate models (Deidda *et al.* 2006b).

- Generating high-resolution rainfall data for simulation studies.

- Combining estimates from instruments operating at different resolutions.

With the idea of extrapolating the variability observed in the recorded scales to the new generated ones, several downscaling methods have been proposed (Deidda 2000; Ferraris *et al.* 2003a; Menabde *et al.* 1999; Menabde *et al.* 1997; Pegram and Clothier 2001a, 2001b; Rebora *et al.* 2006; Rodriguez-Iturbe *et al.* 1986; Venugopal *et al.* 1999). Each method uses a different model to characterize the variability at the different scales and concentrates on particular aspects of the data. Few studies comparing the various methods have been performed to evaluate which method performs better and under which circumstances (see e.g. Ferraris *et al.* 2003a).

Spatial variability in different directions, and even temporal variability using the "Taylor Hypothesis" (Zawadzki 1973), can be treated in a similar manner. However, the structure of rainfall in the vertical is different from that in plan. As a result, the process of modelling precipitation in 3 dimensions must take into account the structure driven by the physical processes underlying the precipitation. If this is not done the result will be unrealistically modelled precipitation fields.

1.3. Sources of error in radar Quantitative Precipitation Estimates

Weather radars can provide three-dimensional precipitation measurements with a high temporal and spatial resolution from a single site (detailed explanation of the radar principles can be found in Doviak and Zrnic 1992), but its measures are affected by a series of errors (Joss and Waldvogel 1990; Wilson and Brandes 1979; Zawadzki 1984).

Errors arise from the electronic/mechanical parts of the radar, from the interaction of the radar beam with ground targets or from the precipitation itself. Zawadzki (1984) classified them into random, systematic and range-dependent. A brief description of the errors is given here. Further details can be found in Berenguer (2006); Sánchez-Diezma (2001) and references therein.

Radar measurements have to be calibrated. This can be done using targets with know reflectivity (passive spheres, *transponders*, the Sun, mountain echoes, etc.) or using external measures. The most common way is calibrating (adjusting) against raingauges (see e.g Rosenfeld *et al.* 1994; Wilson and Brandes 1979 as example of two methodologies), but this process is not free of uncertainty due to the variability of the Z-R transformation (relationship to transform reflectivity (Z) into rain rate (R)), sampling volume and time lag discrepancies between both instruments.

Interception of the radar beam with orography produces, in one hand clutter, and, on the other, reduces the energy that passes beyond. Several algorithms to mitigate the effects of ground clutter problem have arisen. "Clutter maps" obtained in clear-sky conditions can be used to eliminate clutter areas (Joss and Waldvogel 1990), but this methodology does not consider cases where the beam propagates in the atmosphere in non-standard conditions (*anomalous propagation*) and therefore produces different clutter areas. Doppler information of the targets can also be used if available (Doviak and Zrnic 1992), but the lack of precision and the fact that only the radial velocity respect the radar is retrieved can make the algorithm identify rainy areas as clutter, and some real clutter (like wind turbines) have non-zero Doppler velocities. More advanced techniques try to combine several factors to better identify clutter characteristics (see e.g. Berenguer *et al.* 2006) or use polarimetric measurements, if available (Hubbert *et al.* 2009a; Hubbert *et al.* 2009b). Once the ground clutter is eliminated the estimation of the radar in those areas is obtained preferably by reconstructing the Dopper spectra, if available or interpolating the surrounding values not

contaminated (e.g. Sánchez-Diezma *et al.* 2001a). On the other hand, the energy intercepted by orography can be estimated using Digital Elevation Models [DEM] (Delrieu *et al.* 1995), but this method is highly dependent on the beam propagation conditions.

Intercepted targets attenuate radar signal. Attenuation largely depends on the size of the intercepted targets, material, and on the wavelength of the radar. Attenuation by atmospheric gases can be considered negligible in the wavelengths at which weather radars usually operate, but not the attenuation produced by the precipitation itself. At S-band radars (wavelength of ~10 cm), attenuation by precipitation is relatively low, but at C-band radars (wavelength of ~5 cm) –most of the operative ground radars around the world are C-band radars– it can reach 12 dB in the extreme cases of strong convective cells. This problem is accentuated in spaceborne radars. The limitations in power, weight and size of the antennas plus the need of a narrow beam to reach an acceptable resolution forced the use of K_u-band (~1.5 cm) radars or even smaller wavelengths. There is an analytical solution to the correction of the attenuation (Hitschfeld and Bordan 1954) but it is extremely sensitive to radar calibration. Several techniques have been developed to improve the attenuation correction (e. g. "surface reference technique" developed for spaceborne radars and posterior improvements, Meneghini *et al.* 2004; and techniques involving dual wavelength radars –like the K_u/K_a-band radar that GPM will carry onboard– Meneghini *et al.* 1992), but the attenuation is still the major problem in spaceborne radars.

If we are interested in precipitation at ground, a large source of uncertainty in data from ground-based radars is due to the increasing height of measurement with range. The radar Bright Band (an enhancement of reflectivity values around the 0º isotherm) dominates precipitation vertical structure (the Vertical Profile of Reflectivity [VPR]). This leads to a severe underestimation at far distances (where the radar beam is above the bright band) and a severe overestimation at medium distances (where the radar beam intercepts the bright band). Several algorithms have been developed to estimate precipitation at ground taking into account the vertical structure of radar estimates and their variability (e.g. Franco 2008).

A last step in the estimation of precipitation by radar is usually the transformation of reflectivity factor retrieved by the radar (Z) into rain rate (R). These two variables are related through the Drop Size Distribution [DSD], that is, the distribution in sizes of the drops. Reflectivity is proportional to the 6th moment, and rain rate can be approximated with the 3.67^{th} moment of the DSD (see e.g Sempere-Torres *et al.* 1994). DSD is not a fixed function, and varies depending on precipitation type. Therefore the use of an incorrect DSD for the transformation, or even using the correct but considering it constant in time and therefore not depending on the precipitation regime, leads to errors in the rain rates obtained.

1.4. Study of errors

Weather radar precipitation estimates need to be corrected for the sources of error described above. A large effort has been devoted since the first uses of radar precipitation estimates in the 1940s to improve radar measurements, but even making the best effort in the correction algorithms, there is always a remaining uncertainty linked to the estimates.

In the last years many authors started paying attention to the uncertainty related to the precipitation estimates and tried to characterize it. A characterization of the uncertainty inherent in rainfall estimates by radar could lead to a better use of them: optimal merging of the estimations from different instruments, better assimilation of data into NWP models, etc.

As Germann *et al.* (2006) identified, there are two ways to characterize the error structure associated to radar precipitation estimates: the first one is to obtain the global structure of the error comparing against other measurements; the second is to study the characteristics of the error source by source. The first approach can provide a global description of the error, but includes errors in the reference. Meanwhile, the second approach is slower and needs the cross correlation between the errors, but provides more information of the errors themselves during the process.

Comparing against a raingauge network, Ciach *et al.* (2007); Germann *et al.* (2009) derived a characterization for the global error associated with the radar QPE. Germann *et al.* (2009) also used the error characterization obtained to generate an ensemble of radar-based precipitation fields representing the uncertainty in the estimates, and used it as input of a hydrological model.

Studying error by error and in relation with the sources of error explained above, Bellon *et al.* (2005) characterized the errors related to the extrapolation of the precipitation estimates to the ground in stratiform conditions, that is the errors related with the Vertical Profile of Reflectivity. Lee *et al.* 2007 modelled the variability of the DSD in space and time and characterized the errors related to the transformation of reflectivity into rain rate considering a fixed Z-R relationship. With the characterization of the errors related with the DSD and applying a stochastic model, Lee *et al.* (2007) generated an ensemble of plausible precipitation fields considering the uncertainty in the Z-R transformation through the spread of its members. In a second step in this framework, Berenguer and Zawadzki (2008, 2009) studied the cross correlation between these two sources of error (errors related with range and errors related with the variability of the DSD), using simulation of the radar measurement process over observed S-band radar data and a collocated disdrometric measurements.

1.5. Thesis outline

1.5.1. Antecedents

Several Ph.D. theses have been developed in the Centre de Recerca Aplicada en HIdrometeorologia [CRAHI] (formerly GRAHI) within the framework of radar Quantitative Precipitation Estimates for hydrological uses. Sánchez-Diezma (2001) studied the errors affecting radar measurements (explained in section 1.3), how to correct them to minimize their hydrological impact. Later on, Berenguer (2006) focused his studies on three important aspects in radar measurements: correction of non-meteorological echoes in radar scans, correction of the signal attenuation, and development of a nowcasting technique for hydrological purposes. Franco (2008) studied the classification of rainfall into different types according its physical characteristics and the related Vertical Profiles of Reflectivity [VPR] in radar data, towards the extrapolation of the radar precipitation measures to the ground (which is the interest of many applications like the hydrological models). In a recent step in the framework of obtaining the best rainfall field possible at ground in real time, Velasco-Forero (2009) studied how to obtain optimal rainfall fields as combinations of radar and raingauges measurements using geostatistical techniques.

The present thesis takes advantage of all this prior knowledge in the sense that radar precipitation fields used in this work have been corrected with the previously developed techniques (Berenguer 2006; Franco 2008; Sánchez-Diezma 2001) and that the blended rainfall product generated by Velasco-Forero (2009) is used as reference (benchmark) in one of the presented studies.

On the other hand this thesis is the natural continuation of the previous: after correcting as much as possible the radar rainfall retrievals, the question was how to characterize the error that remains after the correction chain, and how to deal with it.

1.5.2. Objectives

After what we have seen in previous sections about the structure of the precipitation, the errors in radar rainfall measurements and the efforts to correct and characterize them, the objectives of this thesis are two.

The first objective is to study the structure of the precipitation regarding its scaling properties. This will help to understand the precipitation phenomenon, to interpret the measurements of a given instrument (working at a specific scale) and to merge estimates from various instruments operating at different scales.

Several models to describe the variability of the precipitation over the scales appeared and have been used to simulate rainfall series or downscale them. In this first part, this thesis will propose a comparison framework where different downscaling methods can be tested to assess their

capabilities and compare between them to check which performs better. A 3D downscaling method will also be proposed with the aim of generate high-resolution precipitation fields based on radar observed measures. These fields will be useful for some studies, like the simulation studies performed in the second part of the thesis.

The second objective is to study the structure of the errors remaining in the radar QPE after the correction chain.

As seen in previous section, there are two ways to analyze the errors. This thesis will study the errors related with distance through physical simulation of the radar measurement process over high-resolution precipitation fields. But also will study the overall error in radar estimates comparing them with a benchmark product. This second way will provide a full description of the errors associated to the radar rainfall measurements. A methodology to generate radar rainfall ensembles from the errors description will be presented.

Errors in spaceborne radar rainfall measurement will also be studied through comparison with ground-based rainfall estimates. The discrepancies will be statistically characterized under different circumstances to assess for their origins. The differences in the estimations from spaceborne radar and from ground equipment will also be analyzed for extreme events.

1.5.3. Structure

After the present chapter, the work done in the thesis is presented as follows:

- Chapter 2 presents a study of the scaling properties of precipitation. Two downscaling methods are compared over rainfall series, and a 3D downscaling method over measured radar precipitation is proposed.

- Chapter 3 studies the error characteristics associated with radar QPE. Firstly a simulation study of the radar error characteristics related to range is performed, and secondly a study of the global error in radar QPE done by comparison against a predefined benchmark.

- Chapter 4 presents the study of the error characteristic of spaceborne radars. Comparisons of TRMM-PR precipitation estimates against ground equipment are shown under different circumstances to characterize the differences between both instrument measures.

General conclusions and future work are the subjects of the final chapter.

CHAPTER 2

Downscaling of precipitation data

2.1. Introduction

Rainfall exhibits scaling properties over a wide range of scales (Fabry 1996; Lovejoy *et al.* 2008). The characterization of these scaling properties is an important research topic with implications in hydrology and hydrometeorology. Also simulating rainfall at higher resolutions than observed (downscaling) is necessary for many quantitative applications of precipitation data (such as enhancing the resolution of climate model outputs, generating high-resolution rainfall data for simulation studies, ...). It has implications in the implementation and testing of stochastic rainfall models and is essential for assessing the hydrological risk/water resources in basins by means of numerical weather prediction or climate models (usually run at coarse resolutions; see e.g. Deidda *et al.* 2006b).

Downscaling methodologies should accurately reproduce the variability and the scaling properties of rainfall from real observations, the statistical characteristics of individual storms and, at the same time, correctly reproduce the characteristics of extreme rainfall as well. The structure of rainfall over the scales and the characterization of its fractal properties has been widely studied (starting in the 1980's -Lovejoy and Mandelbrot 1985; Zawadzki 1987- and until nowadays: Deidda *et al.* 1999; Deidda *et al.* 2006a; Ferraris *et al.* 2003a; Lovejoy *et al.* 2008). The fractal hypothesis assumes that precipitation fields are a hierarchical continuous structure between the scales rather than a set of objects with a characteristic scale.

Sivakumar (2001) studied the temporal structure of rainfall concluding that a multifractal approach is possible. Also in the temporal dimension Breslin and Belward (1999) did a calculus of the possible fractal dimensions of rainfall series. Lima (1998) did a larger study of the temporal structure of precipitation using rainfall series from different regions, comparing some model parameters between regions.

Based on these studies, several approaches have been proposed to downscale rainfall observations (among others, Deidda 2000; Ferraris *et al.* 2003a; Menabde *et al.* 1999; Menabde *et al.* 1997; Pegram and Clothier 2001a, 2001b; Rebora *et al.* 2006; Rodriguez-Iturbe *et al.* 1986; Venugopal *et al.* 1999), all of them based on extrapolating some structure model from the observed scales of rainfall down to the smaller ones.

Most of the models used to generate multifractal rainfall fields are based on random multiplicative *cascades*, that can be build in a discrete space (the so-called α-*model*, see e.g. Gupta *et al.* 1996) or in a continuous way (Lovejoy and Schertzer 1995).

A possible way of implementing a cascade α-model is using wavelets. Perica and Foufoula-Georgiou (1996a) studied the rainfall variability at different scales through wavelet decomposition and proposed a methodology to simulate it with the aim of comparing the output of Numerical Weather Prediction [NWP] models with observations. Venugopal *et al.* (1999) improved the methodology to improve the autocorrelation at the generated scales, and Harris and Foufoula-Georgiou (2001) applied this last model to study the performance of the "Goddard Profiling Algorithm" used to obtain rain retrievals from the Tropical Rainfall Measurement Mission [TRMM] Microwave Imager [TMI].

This chapter shows the comparison of two methods for downscaling time series of rainfall observations. The first one is a classical method based on extrapolating the Fourier Power Spectrum of observations, while the second is a representative of the α-models based on a Wavelet decomposition.

The second part of the chapter proposes a technique to generate 3D rainfall fields based on measured radar rainfall and on interpolation of the observed Vertical Profiles of Reflectivity [VPR] that preserves the vertical structure of the precipitation observed by the radar

2.2. Comparison of two downscaling methods on rainfall series

The aim of this work is to propose a comparison framework to analyze rainfall downscaling methods applied to a collection of one-dimensional time series of observed rainfall. Here, we have compared a method based on the analysis of the Fourier spectrum (described in Pegram and Clothier 2001a, 2001b) with a wavelet-decomposition method (proposed first by Perica and Foufoula-Georgiou 1996b and later on improved by Harris and Foufoula-Georgiou 2001; Venugopal *et al.* 1999).

Downscaling methods have been compared before (e.g Ferraris *et al.* 2003a). The present study aims to determine which downscaling method reproduces better the rainfall variability over different scales starting from an upscaled version of observations, to later on compare the resulting series with the original records. This analysis is conducted by testing the ability of each

downscaling procedure to reproduce the features of the other method, and analyzing the multifractal characteristics of the generated series in comparison with the high resolution records.

The multifractality hypothesis of the series is tested, and the multifractal analysis is done through the "multifractal spectrum" (α-$f(\alpha)$) which provides a full description of the scaling properties of data (Halsey *et al.* 1986).

2.2.1. The downscaling methods

Two relatively simple and commonly used downscaling methods (or methods to generate synthetic rainfall) will be compared in this study. Both are based on extrapolating the structure of rainfall measurements from the large scales to the (non-observed) finer resolution according to the scaling properties of the variance explained by each scale, and both preserve the total amount of precipitation and the location of large-scale structures. The main difference between them is the method used for decomposing the rainfall information into scales: the first method is based on classical Fourier analysis while the second method decomposes them by means of the Haar wavelet (Mallat 1989).

2.2.1.1 Fourier-based downscaling

Fourier decomposition has been commonly used for time series analysis and signal processing. A time series, for instance a Brownian motion, is said to be a self-affine fractal when the variation of the time variable exhibits an 'affine' simple scaling law; in the frequency domain, such time series are characterized by a power-law Fourier spectrum:

$$\Gamma(f) \propto f^{-\beta} \tag{2.1}$$

where $\Gamma(f)$ is the power density associated to a frequency f and β is the exponent of the power law. Because of this, self-affine fractals can be advantageously simulated in the Fourier domain.

Pegram and Clothier (2001a, 2001b) gave an easy-to-use recipe on how to construct and downscale rainfall fields assuming a power-law Fourier spectrum. It basically consists of convolving a Gaussian, white noise process with a power-law filter defined in the frequency domain as $F(f) \propto f^{-\beta/2}$.

This simple approach was first introduced by Bell (1987) to simulate rainfall fields based on the properties inferred from satellite imagery. We used the procedure described above for rainfall downscaling (similarly as Pegram and Clothier 2001b).

Since rainfall intensity is a strictly positive magnitude, we have chosen to process the logarithm of rainfall intensity rather than the time series of rainfall intensity itself. Additionally, this

transformation has the advantage of yielding the transformed fields to be nearly normally distributed.

The simulation of rainfall signals or, similarly, rainfall downscaling, is achieved with this method by extrapolating the power law exhibited by the experimental discrete Fourier Power Spectrum to the non-sampled scales (i.e. to the higher frequencies). With this aim, it is first necessary to estimate the exponent β of the best-fit power law to the Fourier spectrum of rainfall observations (i.e. up to the smallest observed scale). Afterwards, applying a power-law filter (with the required exponent β) to a random white noise process we reproduce a self-affine fractal (pink noise signal). The smallest non-observed scales of this simulation are added to the observations to reproduce the higher-resolution variability.

We observed (similarly as Pegram and Clothier 2001a) that the range of variability of the β parameter is relatively small for the different series of rainfall. In this study, the downscaled series have been generated using a value of β=−1.2 estimated from the average Fourier power spectrum of 120 rainfall series (see section 2.2.2.1).

2.2.1.2   Wavelet-based downscaling

The wavelet transform gives a representation of the signal as a function of both frequency and time, and allows us to study the local variability of fields at different scales (see, e.g., Foufoula-Georgiou and Kumar 1995). The second downscaling approach is based on the fact that the standard deviation of rainfall fluctuations standardized by the scaling component (defined via the wavelet transform) seem to obey a simple scaling law over the different available scales (Harris and Foufoula-Georgiou 2001; Llort *et al.* 2006; Perica and Foufoula-Georgiou 1996a; Venugopal *et al.* 1999). Extrapolating this law permits to simulate rainfall fluctuations over the non-observed smaller scales.

In this method, rainfall signals are decomposed using the wavelet transform (Mallat 1989) with the Haar base (Haar 1910). The sample distributions of the fluctuation components standardized by the scaling component are assumed to be Gaussian with zero mean (Llort *et al.* 2006; Perica and Foufoula-Georgiou 1996a). Moreover, standard deviations of those signals follow a simple scaling law. To generate the new scales we generate Gaussian-distributed random fields with standard deviations as dictated by the scaling-law; these fields will correspond to the standardized fluctuations at the new scales and, so, added to the observations in order to simulate the variability at smaller scales.

In this comparison, instead of generating the downscaled series with the scale-law observed, we used a scaling-law average of the 120 series used in this analysis (see section 2.2.2.1), which is more robust.

2.2.2. Comparison of the two methods

To assess the reliability of the two proposed methods, simulated (downscaled) rainfall signals of the same resolution as observed have been generated using both of them starting from an upscaled version. That is, the original data have been first upscaled up to a certain resolution, and then downscaled with each of the two methods back to the original resolution. Then the comparison is done at the original resolution of observations. Since both methods have a random component (see sections 2.2.1.1 and 2.2.1.2), this process can be done multiple times and the results analyzed statistically.
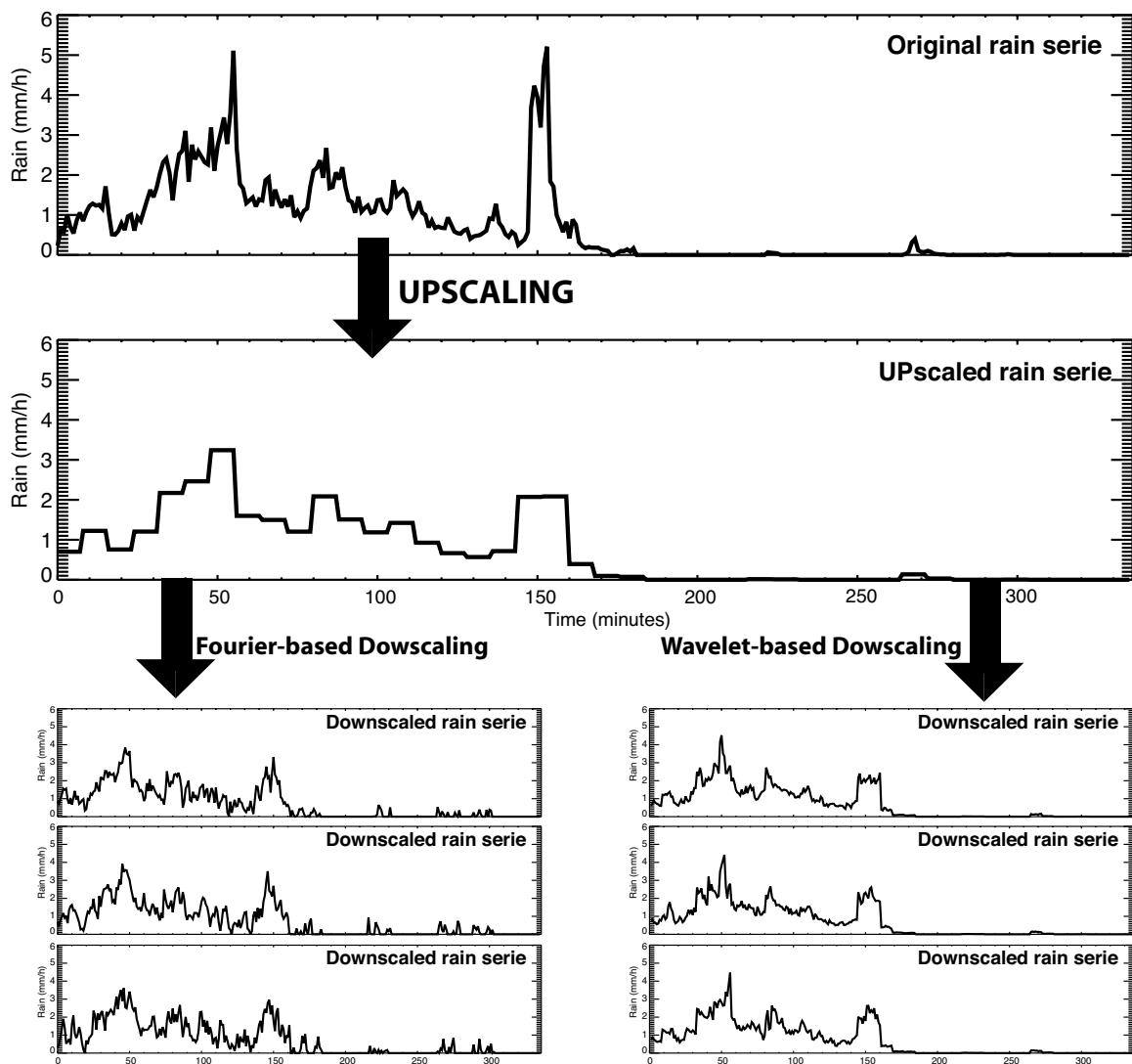
Figure 2.1: Schema of the comparison framework. The original data are first upscaled and then downscaled back to the original resolution with both methods. Since the downscaling has a random component, several realizations can be done. The comparison is done at the original resolution.

Figure 2.1 shows a schema of this comparison framework applied to time series of rainfall rate as observed with a disdrometer with a resolution of 1 minute. The figure also shows the rainfall series

upscaled to a resolution of 8 minutes and 3 examples of series downscaled with each of the analyzed methods back to the original 1-minute resolution.

Each of the proposed methods for rainfall downscaling (based on Fourier or Wavelet decomposition) only focuses on one aspect of rainfall variability: the first, on the distribution of power in the Fourier power spectrum, and, the second, on a scaling law model of the variance explained by each range of scales as decomposed via the Haar wavelet transform. Because of this, each procedure may reproduce the characteristic of rainfall variability on which it is focused, but it may not be able to reproduce that of the other method. On the other hand, both approaches may not fully reproduce other aspects of rainfall variability over the different scales like clustering.

Once we have the original data and the result of the two downscaling methods, two different comparisons have been performed:

- "Cross-verification" of the models assumed for rainfall scaling properties (i.e. the series downscaled by means of the Fourier spectrum have been evaluated in terms of their wavelet scaling properties, and we have also inspected the Fourier spectra of the series downscaled with the wavelet-based method).

- Analysis of the multifractal properties of the generated series, using the actual observations as reference.

These analyses try to solve the question of which is the downscaling method that best reproduces the properties of original observations.

2.2.2.1   Rainfall data used

Rainfall observations used here for the comparison of the two methods were time series of rain rate obtained from the Precipitation Occurring Sensor System [POSS] disdrometer located in Montreal (Canada) for 120 cases between 1994 and 1999. The POSS is a low-power, continuous-wave, X-band, bistatic, Doppler radar developed by the Atmospheric Environment Canada (see Sheppard 1990; Sheppard and Joe 1994) that retrieves the Drop Size Distribution from the average Doppler spectrum. Since our aim is to study the variability at different scales, we have not used series with gaps (i.e. interpolation has been strictly avoided) and we have imposed the series to be, at least, 32 minutes long. The study is done over rain rate (mm/h) series.

While Harris *et al.* (1997) discussed the different factors that may affect the analysis of rainfall scaling properties, in this work we have assumed that the intrinsic errors associated with disdrometer measurements of rainfall do not change the fundamental statistical scaling properties of rain fields. We have also considered that the scale characteristics are constant within the records of each event.

2.2.2.2 Cross comparison

Similarly as described above for the example of Figure 2.1, the study has been done over 119 POSS time series first upscaled to a resolution of 8 minutes. These time series have been downscaled 3 times to the original 1-minute resolution with each of the methods presented above. The procedure has been repeated 20 times with each method, and these are the simulations over which the analysis is carried out.
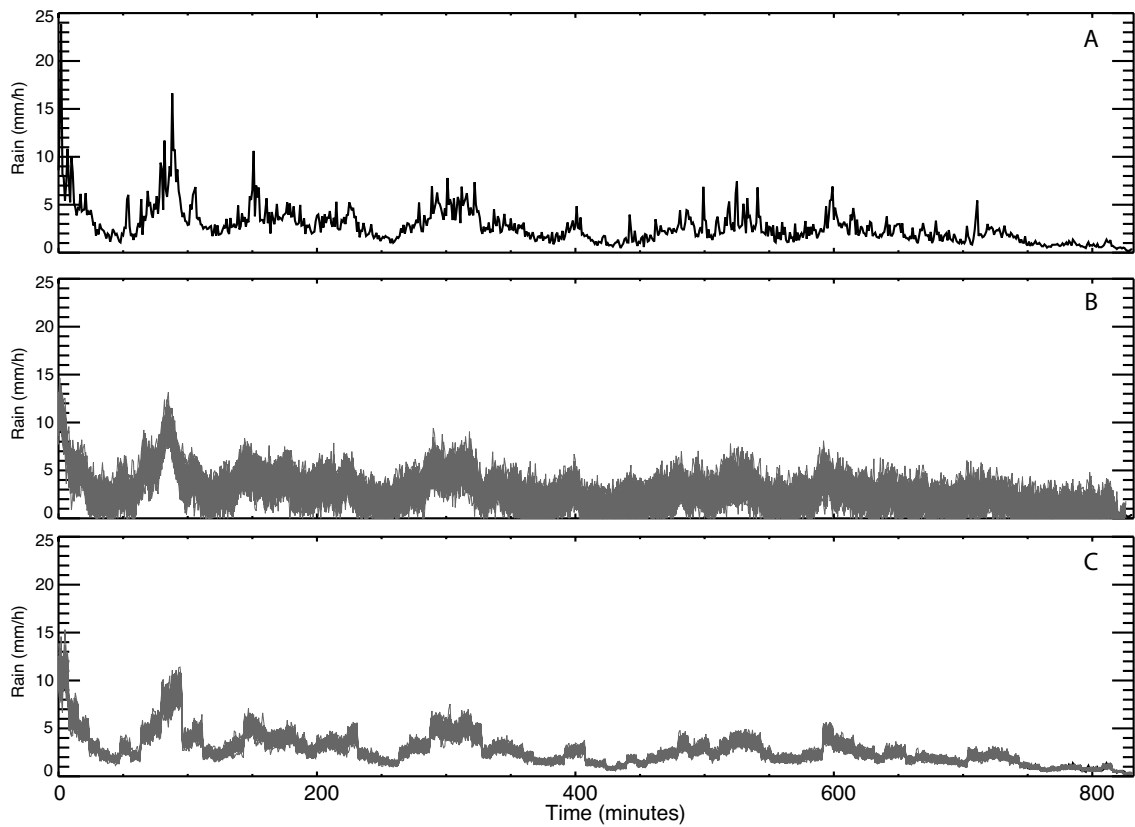

Figure 2.2: Case 1. Original recorded rainfall series on May 2nd, 1998 from 08:12 to 21:58 UTC (A), 20 downscaling series obtained using Fourier based downscaling method, starting from an upscaled version of the original data (B); and 20 downscaling series obtained with the wavelet based downscaling method (C) starting from the same upscaled version.
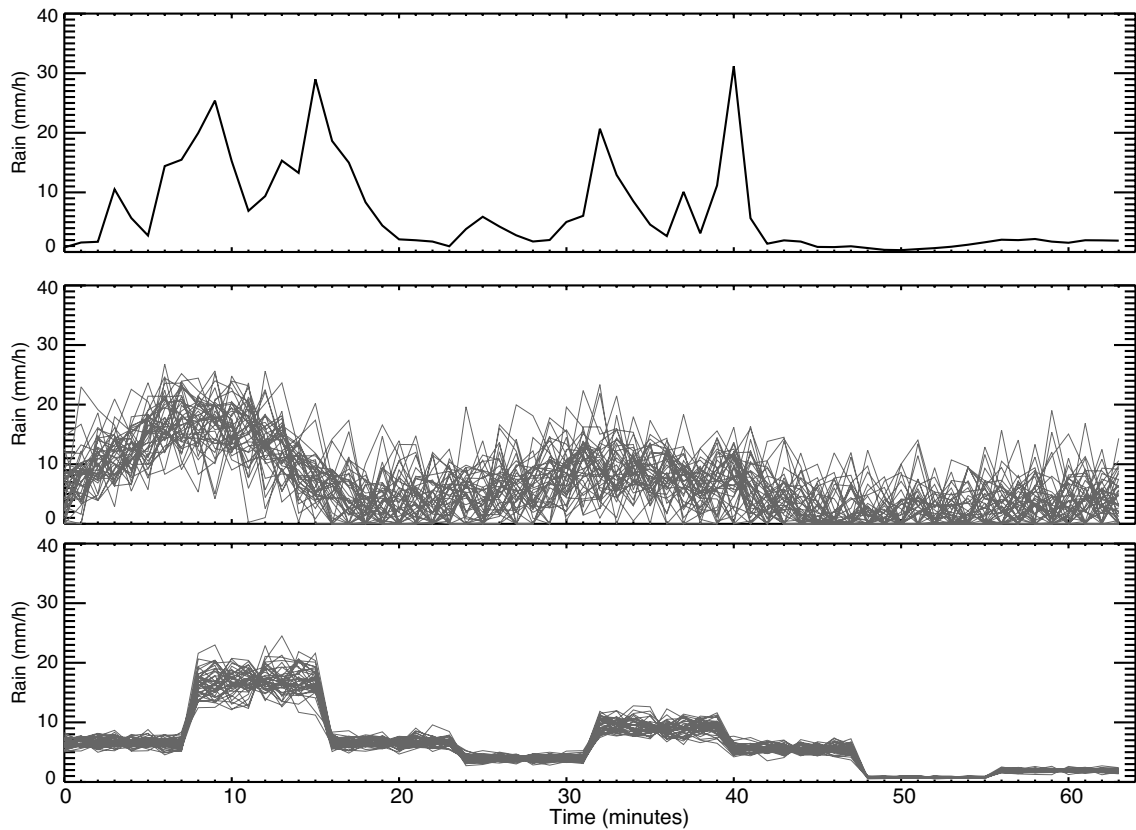
Figure 2.3: Case 2. Same as Figure 2.2 but for a shorter event recorded on August 10th, 1999 from 15:10 to 16:14 UTC.

Although the study has been done over 120 rain rate series, two representative cases are presented in detail here. Figure 2.2 (Case 1) shows a long series of rainfall but with relatively low intensities. The first panel shows the original rainfall records and panels B and C show 20 downscaled series generated with the Fourier- and wavelet-based methods, respectively. It can be observed how the Fourier-based method generates a higher dispersion between the members than the wavelet based. Figure 2.3 (Case 2) shows a shorter event with higher intensities. Again, it can be seen how the Fourier downscaled series show more scatter between them than those generated with the wavelet method. It can also be seen how, for both cases, the series obtained with the wavelet method perform closer to the starting upscaled series than those generated with the Fourier method, and that the latter do not have as many extremes as the former.
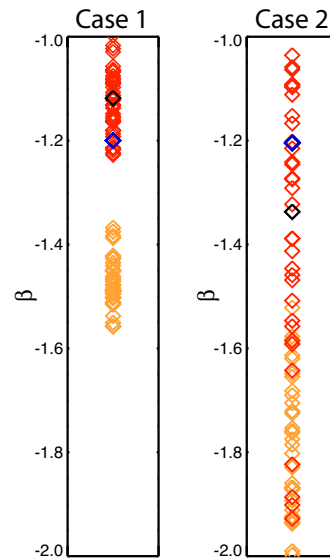
Figure 2.4: Distribution of the β parameter of the downscaled series. Fourier-based series are plotted in red, and wavelet-based series, in orange. β=1.2 is the parameter used by the Fourier-based method, and it is plotted in black. On the left panel, for the first case (see Figure 2.2), and on the right panel for the second case (see Figure 2.3).

Figure 2.4 shows the distribution of the exponent of the Fourier power spectrum, β (see equation 2.1), for the 20 replicas obtained with the two downscaling methods and for the cases of Figure 2.2 and Figure 2.3. It can be seen that the Fourier method reproduces well this parameter (it is not exact since there is a random component in the method). On the other hand the wavelet-based method produces series with lower exponents β, which suggests that for these series large scales explain a significantly large part of the total variance (as can also be speculated from eye inspection of the simulated series).

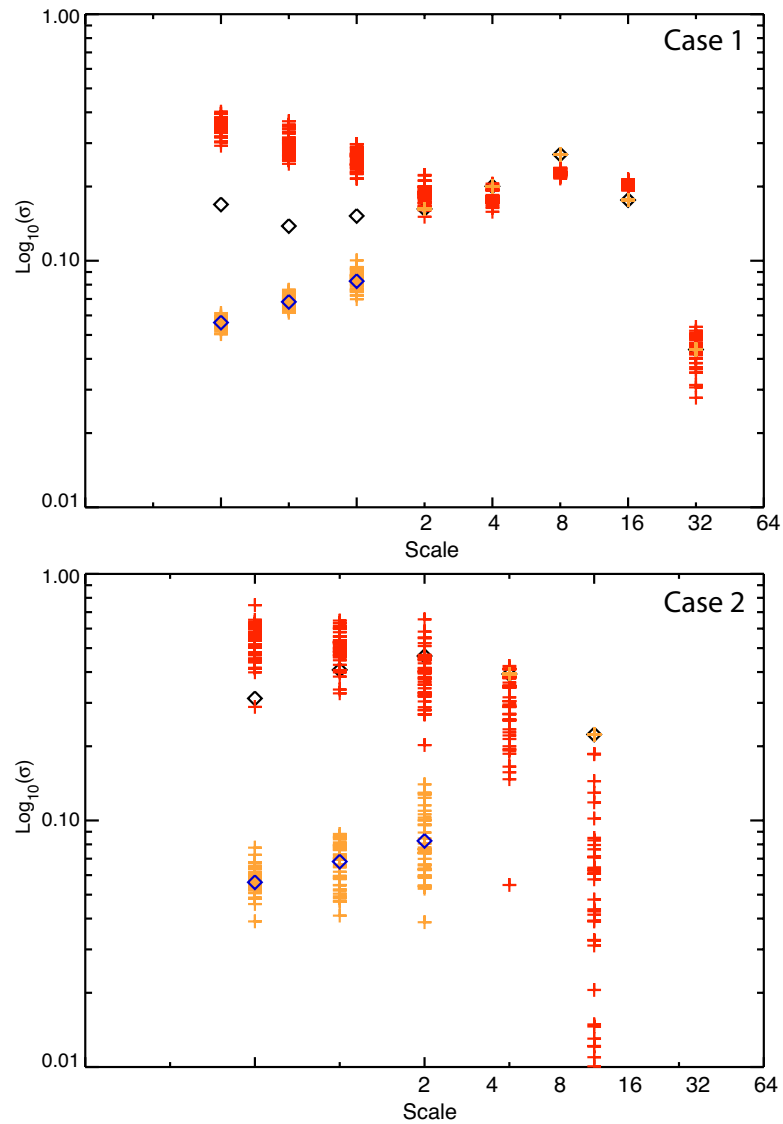Figure 2.5: Wavelet scaling laws of the different series. Downscaled series using the Fourier-based method in red, downscaled series using the wavelet-based method in orange, original data in black. Used in the method in blue. On the top panel, for the first case (see Figure 2.2), and on the bottom panel for the second case (see Figure Figure 2.3).

By performing wavelet decomposition of the series downscaled with the Fourier-based method, we can observe that the standard deviations of the standardized fluctuation of the simulations are systematically higher than those observed. This indicates that modelling rainfall as a self-affine fractal (i.e. with the Fourier-based method) overestimates the amplitudes associated with the small-scale rainfall fluctuations. Figure 2.5 shows the wavelet scaling laws for all the downscaled series for the two cases presented in Figure 2.2 and Figure 2.3. Scales over 8 min are observed and, thus, not changed by the wavelet-based technique (all the values of the standardized deviation -in orange-collapse to the value of the original field –in black-). It can be seen how the wavelet series have coefficients in the new generated scales around the imposed ones (based in several series -in blue-), which are different from these of the original series (in black). For the series generated with the

Fourier-based method, the standard deviation values are different from those of the original data over all scales and also show higher scatter among them (this effect is bigger in the second case, corresponding to the series with higher intensities).

The wavelet model produces series with a scaling-law performing around the imposed one, thus if the imposed one is close to the original series, the resulting downscaled series will have similar scaling-laws as the original data.

2.2.2.3   Multifractal analysis

In order to compare the series generated with both the Fourier- and the wavelet-based methods, we have also analyzed the observed and simulated series in terms of their multifractal characteristics.

For a data set to be multifractal, it should verify the following properties: (i) every moment of the data should exhibit scaling properties, and (ii) the scaling properties of moments of different order should also be different. Unlike for multifractals, monofractals show the same scaling properties for all moments. The hypothesis of multifractality of rainfall was tested by Ferraris *et al.* (2003b) using radar data. Their study concluded that the hypothesis that rainfall is monofractal (i.e. not multifractal) could not be rejected. Here, we will discuss this hypothesis based on a significantly different data set.

The usual multifractal analysis is performed with a modification of the box-counting method (Mandelbrot 1982) that is used to define the generalized fractal dimensions $D(q)$ (Hentschel and Procaccia 1983). The box-counting method involves sequential partitioning of the study area and upscaling processes to form measures $\mu(\varepsilon)$ at different scales, ε. Then $\tau(q)$ is defined by equation 2.2:

$$\tau(q) = \lim_{\varepsilon \to 0} \frac{Log(\sum \mu^q(\varepsilon))}{Log\varepsilon} \tag{2.2}$$

And the generalized fractal dimension is defined as equation 2.3:

$$D(q) = \frac{\tau(q)}{q-1} \tag{2.3}$$

In this study we have used the algorithm proposed by Block *et al.* (1990) which is less demanding in terms of computer resources without increasing numerical problems.

In this context, if the fractal dimension is the same for all moments ($D(q)=D(0)$ for every q) then the data are said to be monofractal instead of multifractal.
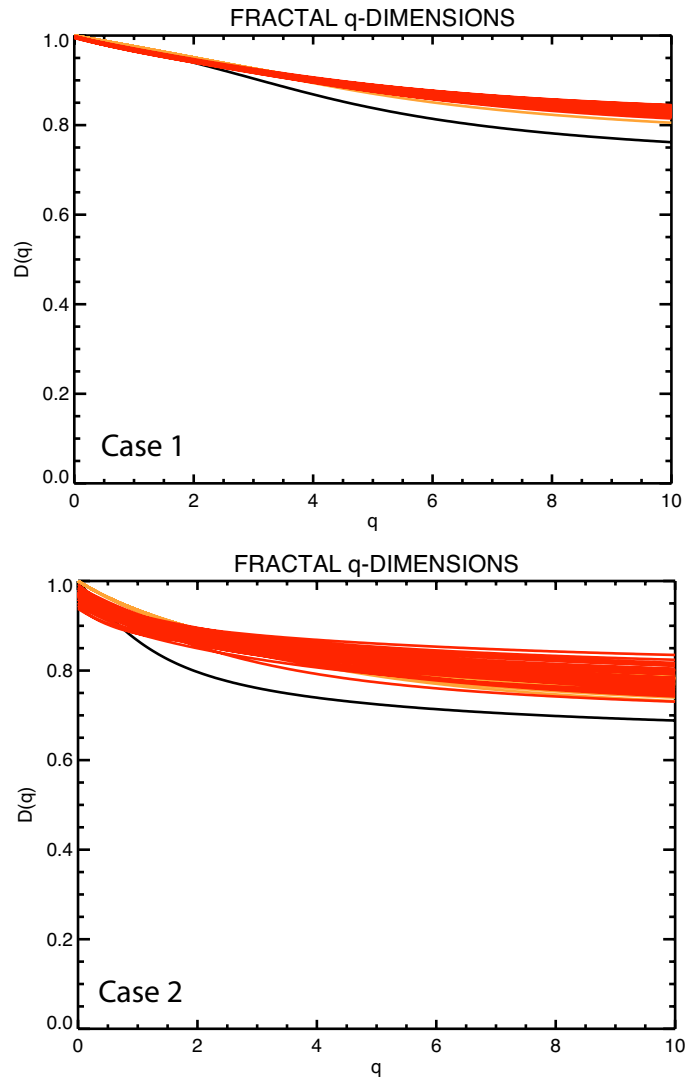
Figure 2.6: Fractal q-Dimensions ($D(q)$) of the different series. Downscaled series using the Fourier-based method in red, downscaled series using the wavelet-based method in orange, and original rainfall series in black. On the top panel, for the first case (see Figure 2.2), and on the bottom panel for the second case (see Figure 2.3).

Figure 2.6 shows the *q-D(q)* plot for the observations and for the downscaled series using the downscaling methods previously introduced. It can be seen how, in both cases, $D(q)$ is not constant but it decreases with *q*. This means that all the series could be considered multifractal. This implies that the rainfall peaks have different behaviour depending on their intensity: the more intense rainfall peaks are, the more clustered. In the case of the series having rain rate values greater than zero over the entire sequence, $D(0)$ (known as fractal dimension or support dimension) is equal to one.

Analyzing Figure 2.6 in more detail, we can see that none of the two methods is able to reproduce the "multifractality" that the original series exhibit. However, the series generated with the wavelet-based method seem to perform closer to the observations, having lower values of $D(q)$ for all *q*.

A global description of the scaling properties of multifractals can be done through the determination of the continuous spectrum of scaling indices $\alpha(q)$ (Lipschitz-Hölder exponents) and their densities $f(\alpha(q))$ (Halsey *et al.* 1986). The multifractal spectrum $f(\alpha(q))$ provides detailed distribution of the singularities of the signal and is considered to be more general than the generalized fractal dimensions $D(q)$. The multifractal spectrum (Halsey *et al.* 1986) is defined through the Legendre transform, that is using the equations 2.4 and 2.5.

$$\alpha(q) = \frac{\partial}{\partial q}\big[(q-1)D(q)\big] = \frac{\partial}{\partial q}\tau(q) \tag{2.4}$$

$$f(\alpha(q)) = q \cdot \alpha(q) - (q-1) \cdot D(q) \tag{2.5}$$

However, in this study we have used the direct determination of the spectrum proposed by Chhabra and Jensen (1989) which is simpler to apply on experimental data. In order to overcome the numerical instabilities involved in the calculus of the multifractal spectrum (it requires the computation of $D(q)$ for high values of q) we have implemented the computation solution of Chen *et al.* (2004). This method allows us to increase the range of q in the calculations and, therefore, to get a better description of the curve $\alpha(q)$-$f(\alpha(q))$ and a full description of the range of $\alpha(q)$.
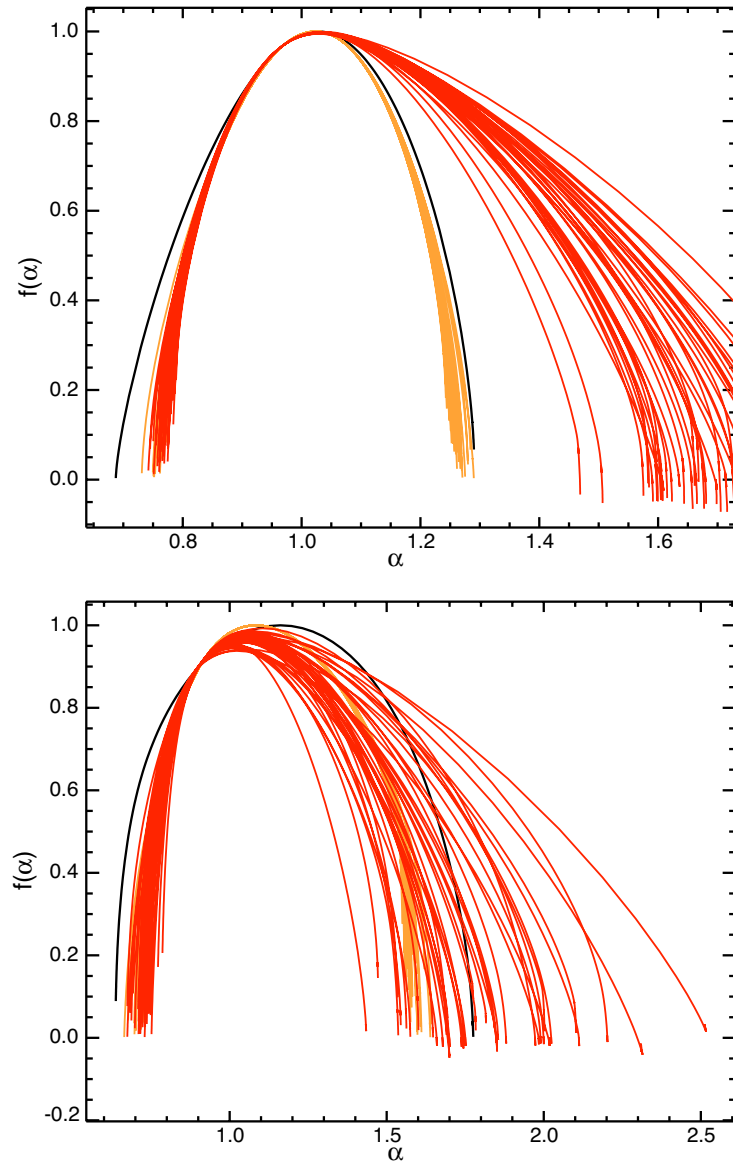
Figure 2.7: Multifractal Spectrum of the different series. Downscaled series using the Fourier-based method in red, downscaled series using the wavelet-based method in orange, and original rainfall series in black. On the left panel, for the first case (see Figure 2.2), and on the right panel for the second case (see Figure 2.3).

Figure 2.7 shows the multifractal spectrum of the observed rain rate series and those of the series downscaled using the methods described above. The maximum of $f(\alpha(q))$ coincides with the fractal dimension of the series ($D(0)$). In both cases it is exactly equal to one for the original series, but since some of the generated series for the second case do have some zero values, their corresponding $\alpha(q)$-$f(\alpha(q))$ curves do not reach this value. This happens more often in the Fourier-based downscaled series than in those downscaled with the wavelet-based method.

The spectrum range of α-values is related to the distribution of the singularities (or, alternatively, the amount of clustering of the different values present in the series of rainfall intensities): A narrow range of α-values indicates homogeneity of the distribution of the singularities and the

larger the range, the more heterogeneity in the distribution. In the presented cases we can see that the range of α is wider than that of the original data for almost all the Fourier downscaled series (being in the first case presented really far from the observations). This implies that the series generated with the Fourier-based method are more heterogeneous than the original records. On the other hand, the series downscaled with the wavelet based technique have a multifractal spectrum performing much closer to the one of the original data, and also exhibit less dispersion between the different members.

The region $\alpha < \alpha(0)$ of the multifractal spectrum (corresponding to positive-order moments, $q>0$), that is the left half of the spectrum, highlights the properties of the regions with high intensities (the positive-order moments are dominated by the behaviour of the high values). The region $\alpha > \alpha(0)$ (corresponding to negative-order moments, $q<0$) refers to the low intensity regions because the negative-order moments give more weight to the low intensities. For both downscaling methods we observe that the left tail of the spectrum (the regions dominated by higher intensities) is not well reproduced, so none of the methods is fully able to generate the distribution and clustering of the high values present in the original records. Looking to the right tail (regions dominated by the lower intensities) we see that, for the first event, the wavelet technique results in a much closer spectrum to that of the original records, while the series downscaled with the Fourier-based technique have a significantly longer tail. This might indicate that the series generated with the Fourier-technique do not reproduce well the characteristics of the regions dominated by low intensities. Analyzing the second case, the left tail of the multifractal spectrum for the observations falls within the range of the spectra of the series downscaled with the Fourier-based technique. However, the dispersion between the different members is rather high.

2.3. 3D downscaling of precipitation

High-resolution 3D rainfall fields may be very useful for some studies. In particular, they may be used as reference in simulation studies quantifying the uncertainty introduced by the different sources of error affecting radar measurements (e.g. Anagnostou and Krajewski 1997; Borga *et al.* 1997; Zhang *et al.* 2004), and to assess the hydrological effects of these errors (Sánchez-Diezma *et al.* 2001b; Sharif *et al.* 2002, 2004).

Traditionally, these rainfall fields have been obtained through two main approaches: 1) using pure stochastic rainfall models or 2) downscaling real precipitation measurements.

Stochastic models can provide a wide range of spatial and temporal rainfall patterns for many resolutions and with acceptable computational speed. The main problem involved in the stochastic simulation is the lack of physical consistency between atmospheric processes and the simulated rainfall fields.

On the other hand, for downscaling techniques, synthesizing rainfall fields with higher resolution than observed and reproducing the rainfall variability at all scales is quite a challenge due to the complexities of rainfall (Lanza *et al.* 2001). Typically, radar measurements (and also satellite imagery) have been used in this framework. A straightforward approximation to this problem is downscaling rainfall measurements by tri-linear interpolation (i.e. precipitation values of the 3D Cartesian high-resolution field are obtained through linear interpolation of the "*n*" closest neighbours, see Sánchez-Diezma 2001). However, this technique does not preserve the real variability in the new created scales, which may be a significant limitation for some studies.

The first techniques introducing variability proposed to impose random noise to a given high-quality radar-rainfall field. Krajewski and Georgakakos (1985) changed the noise level from point to point depending on the local original field characteristics such as the magnitude and the horizontal gradient of reflectivity. During the last few decades more advanced downscaling techniques that exploit the fractal behaviour of rainfall have been proposed (reviews of the state-of-the-art may be found in Lovejoy and Schertzer 1995 and Ferraris *et al.* 2003a).

Among fractal techniques, Perica and Foufoula-Georgiou (1996a) proposed a 2D wavelet implementation of a cascade model based on a variability analysis of rainfall at different scales. This technique was later improved by Venugopal *et al.* (1999) and used by Harris and Foufoula-Georgiou (2001) to evaluate the performance of the Goddard Profiling rainfall retrieval algorithm used in the Tropical Rainfall Measuring Mission [TRMM] Microwave Imager [TMI].

Another set of downscaling techniques is based on modelling rainfall fields through the analysis of its Fourier spectrum (see the Strings of beads model, Pegram and Clothier 2001a, 2001b).

The previous section compared both methods using rainfall series, concluding that the wavelet model seems to perform closer to the reality. Therefore, an equivalent wavelet model will be used in this section for downscaling of 2D precipitation fields.

In this study we propose a 3D downscaling technique for radar data, based on modelling precipitation fields using a combination of wavelets for 2D downscaling and homotopic techniques (continuous deformation of functions) for the vertical dimension. This approach has as its main advantage the fact that it keeps the 3D structure of the rainfall patterns measured by the radar without imposing a vertical structure like Anagnostou and Krajewski (1997).

The proposed 3D downscaling process is composed of three independent steps:

- Downscaling of the lowest radar scan up to the requested resolution using a two-dimensional wavelet model.

- Downscaling of the remaining tilts based on a homotopy (continuous deformation) of the observed Vertical Profiles of Reflectivity (VPR).s

- Transforming the downscaled polar values to the requested Cartesian grid.

This scheme has been implemented over radar data measured by the C-band radar of the Spanish Meteorology Agency (AEMET; formerly INM) located in Corbera de Llobregat (close to Barcelona, Spain). The 20-elevation volume scans provided by this radar have a resolution of 0.9° in azimuth and 2 km in range.

This study has been carried out on a 64 x 64 polar bin area extracted from the radar's lowest elevation, located near the radar (at ranges between 20 and 148 km) in a region little affected by ground clutter and corrected for the common radar problems (ground clutter, orographic screening and speckle: Sánchez-Diezma 2001).

2.3.1. 2D Downscaling of radar images. Wavelet Model.

The discrete orthogonal wavelet decomposition (Mallat 1989) allows us to study the local variability of the rainfall field at different scales and, at the same time, the process is fully reversible. In this study we have chosen the Haar wavelet base (Haar 1910) for simplicity.
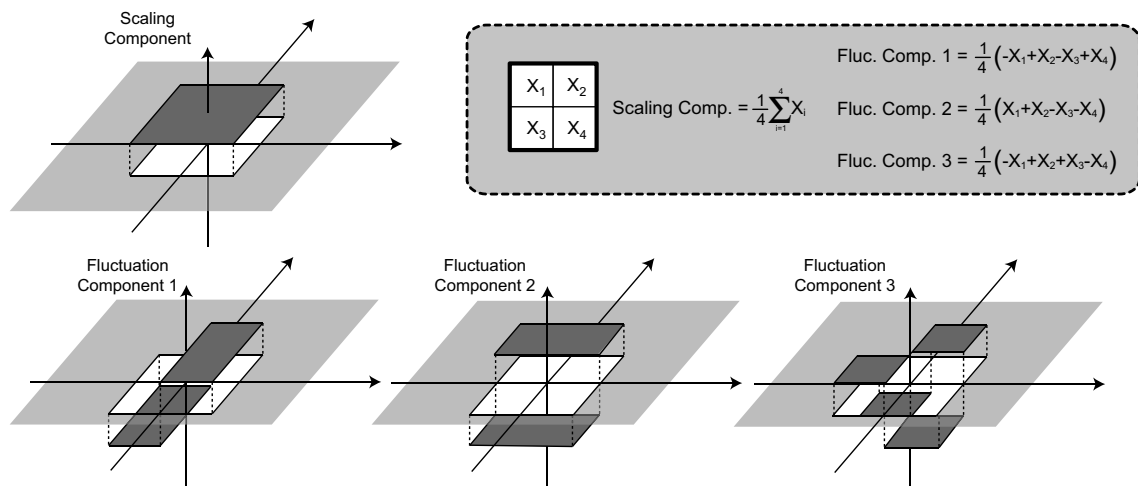

Figure 2.8: Graphical scheme and mathematical expression of the 2D wavelet transform using the Haar base.

The 2D Haar wavelet transform breaks down the discrete rainfall field observed at a certain scale (*m*) into four components at the next larger scale (*m+1*), where *m=1* is the lowest observed scale. These components are: the average component (scaling component, Sc_{m+1}) and three fluctuation components (one in each direction: $Fl_{m+1,1}$, $Fl_{m+1,2}$; and a crossed one: $Fl_{m+1,3}$). In Figure 2.8 there is a graphical scheme of the wavelet components and the exact mathematical expression. The wavelet decomposition can be iterated up to the largest possible scale: the entire rainfall field. In this study, the first fluctuation component corresponds to the variability between azimuths, the second to the variability between ranges, and the third to the crossed variability.

2.3.1.1 Scale variability analysis

The proposed wavelet model is based on the hypothesis (verified by Perica and Foufoula-Georgiou 1996a) that sample distributions of the standardized fluctuations ($X_{m,i}$, see equation 2.7) are Gaussian distributed with zero mean, and standard deviation of those fields follow a simple scale-law.

$$X_{m,i} = \frac{Fl_{m,i}}{Sc_m} \sim N(0,\sigma^2_{m,i}) \tag{2.6}$$

$$\sigma_{m,i} \propto 2^{(m-1)\cdot H_i} \sigma_{1,i} \tag{2.7}$$

In particular, equation 2.7 relates the standard deviation at the scale m with the one at the smallest observed scale, $\sigma_{1,i}$, where H_i is the scaling parameter for the standardized fluctuation i, $X_{m,i}$ (i=1,2,3) fitted for the range of observed scales.
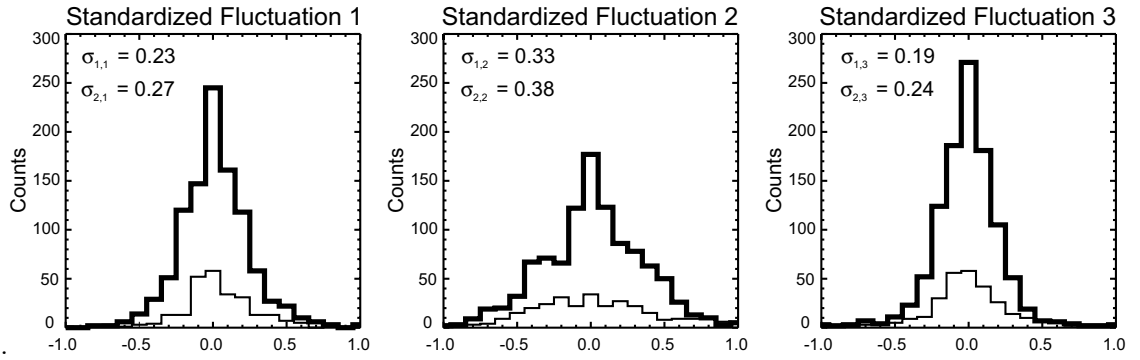
Figure 2.9: Experimental distribution of the standardized fluctuations in a stratiform case. Thick line corresponds to the scale m=1 and thin line to m=2.

Figure 2.9 shows the sample distributions of the three standardized fluctuations of the reflectivity factor (Z: mm^6·m^-3) at two consecutive scales for a stratiform case not affected by bright band. It should be noted that an increase in the scale by on step results in a reduction in the number of samples by a factor of 4 (the number of samples of the second scale-up distributions, m=2, is therefore, smaller than in the first scale, m=1).

Figure 2.10: Standard deviations of the three standardized fluctuations at various scales based on 100 radar images containing a mix of rainfall situations.

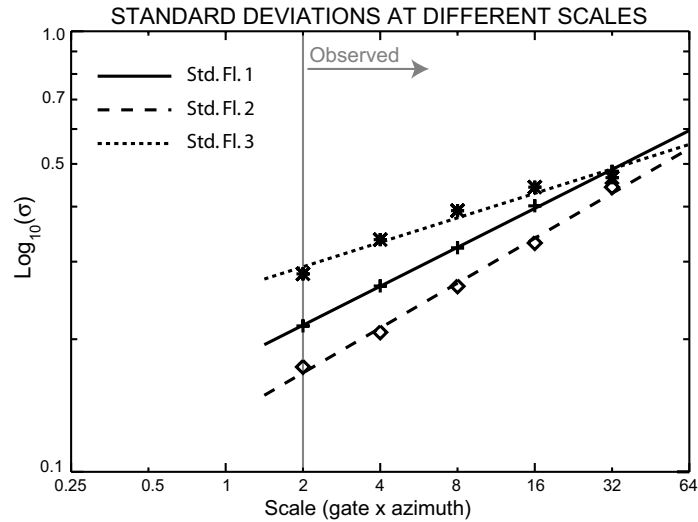Figure 2.10 shows the standard deviations of the three standardized fluctuations over several scales derived from 100 radar reflectivity fields containing a mix of rainfall situations. In this figure it can be observed how well the scaling-law hypothesis is verified working on a large dataset.

2.3.1.2 Downscaling process

Once the scale variability analysis is completed (see Figure 2.10), it is possible to simulate the fluctuations at smaller scales. It is first necessary to extrapolate the standard deviations of the three standardized fluctuations to the current scale, using the experimental scaling-law fitted to the observed scales (equation 2.7).

The standard deviations are used to generate random Gaussian fields with zero mean and the appropriate standard deviation (to avoid obtaining negative reflectivity values in the final result, these Gaussian distributions are truncated between –1 and 1), to generate the fields corresponding to the three standardized fluctuations at the current scale.

The next step is to obtain the fluctuation values from equation 2.7 (i.e., the standardized fluctuation components are denormalized by the scaling component). Finally, simulated reflectivity values are obtained by means of the inverse wavelet transform, that is, through the following equations (linear system):

$$
\begin{aligned}
p_{m-1,1} &= Sc_m - Fl_{m,1} + Fl_{m,2} - Fl_{m,3} \\
p_{m-1,2} &= Sc_m + Fl_{m,1} + Fl_{m,2} + Fl_{m,3} \\
p_{m-1,3} &= Sc_m - Fl_{m,1} - Fl_{m,2} + Fl_{m,3} \\
p_{m-1,4} &= Sc_m + Fl_{m,1} - Fl_{m,2} - Fl_{m,3}
\end{aligned}
\tag{2.8}
$$

Where $p_{m-1,1}$, $p_{m-1,2}$, $p_{m-1,3}$ and $p_{m-1,4}$ are the four generated pixels at the downscaled scale, *m-1*.

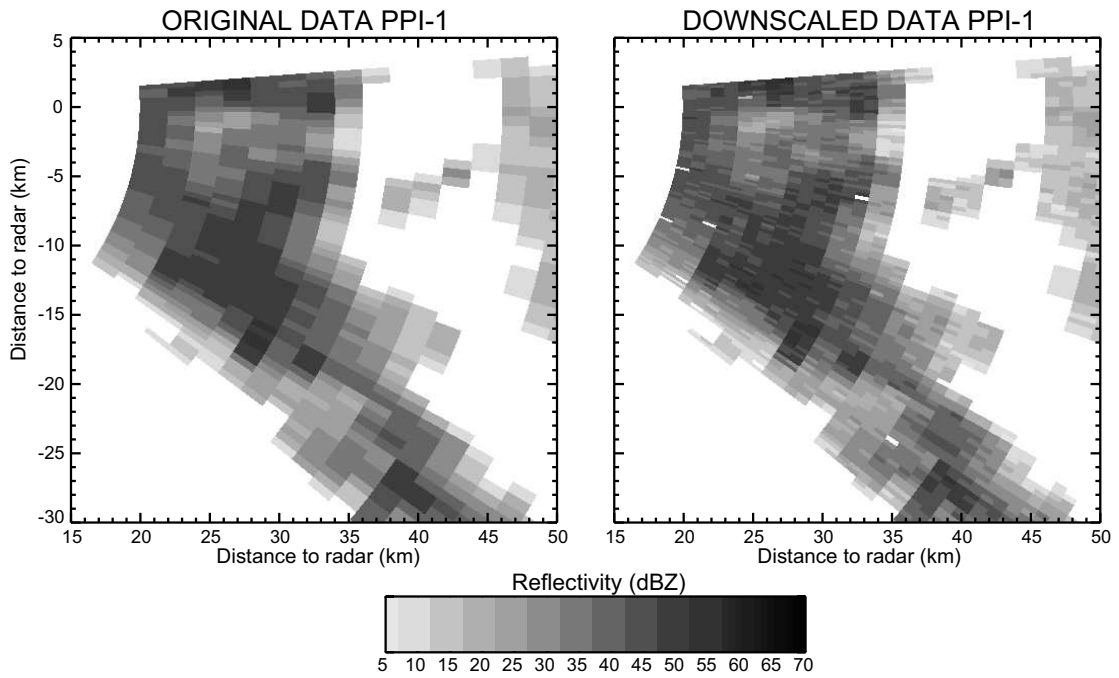The whole process can be iterated up to the requested resolution.

Figure 2.11: Downscaling of the first radar Plan Position Indicator [PPI] iterating once the wavelet process.

Figure 2.11 shows an example of this downscaling process, iterating once, over a section of a reflectivity map showing a convective case. In this figure we can see how the downscaling method, while preserving the observed pixel structure (by construction), introduces new extreme rainfall values (both high and low) into the field. This can be clearly seen in the areas where new zero-values have been generated.

2.3.1.3   Fourier analysis of the downscaled fields

In the scheme proposed above, fluctuations are generated randomly, assuming that they are not correlated. Thus, no structure is added in the new generated scales. In the analysis of the Fourier spectra of the downscaled fields, this implies that the high frequency components change with respect to the ones that can be observed in real rainfall fields (as observed by Harris and Foufoula-Georgiou 2001).

To study this problem, and to compare the various spectra at the same resolution, the radar reflectivity maps have been first upscaled twice, and afterwards, the technique has been applied twice to reach the original resolution (similarly as previous subchapter). In order to quantify this phenomenon, we suppose that a power-law can be fitted to the radially averaged Fourier power spectrum of the reflectivity fields (Pegram and Clothier 2001a, 2001b):

$$\Gamma(f) \propto f^{-\beta} \tag{2.9}$$

where $\Gamma(f)$ is the Fourier power density associated to a frequency f and β is the exponent of the best fit. This exponent (β) –as explained in previous subchapter– condenses the field autocorrelation at the various scales, being zero the value of no correlation at any scale (random noise).
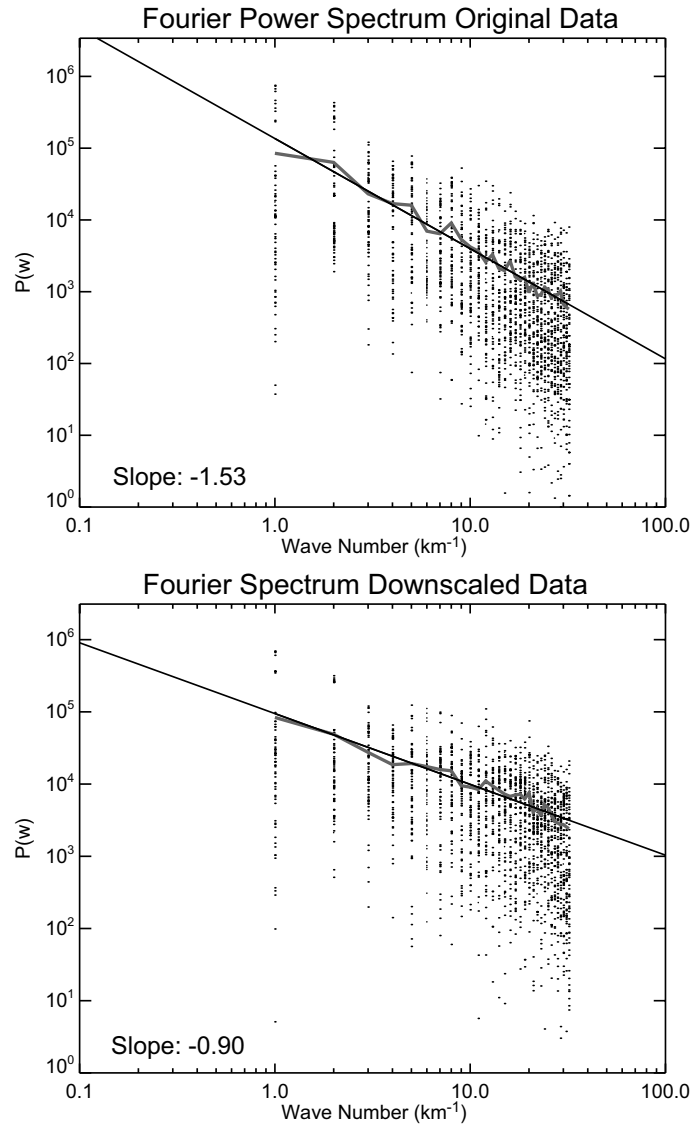
Figure 2.12: Fourier power spectrum radially averaged for a stratiform image (upper plot), and for the same images after the up-scaling and down-scaling process. The grey line represents the mean radially averaged spectrum and the black line its best fit. The slope (β) of that line is plotted inside each graph.

To illustrate how the spectrum changes after the downscaling, Figure 2.12 shows the Fourier power spectrum for a stratiform image and for the same image downscaled (with two iterations starting from the image upscaled twice). Mean spectrum is plotted with its best fit for both graphs. In this figure we can see how, after the downscaling process, the exponent (β) gets closer to zero (less correlation between pixels). We can observe in this figure that β corresponding to the downscaled field are lower than the original, is the same effect observed in the previous section.

In order to mitigate this phenomenon, Harris and Foufoula-Georgiou (2001) proposed a sorting of the generated rain values within a pixel according to their neighbours' intensities. Downscaled pixels are sorted at each wavelet iteration by shifting the high value to the place surrounded by higher values and the lowest to the place surrounded by lower values. This pixel readjustment succeeds in partially correcting the β values in the downscaling process (recovering the "lost" correlation), but not completely.

With the idea of not only simulating the right distribution of the standardized wavelet fluctuations when downscaling, but also their autocorrelation, we studied the Fourier power spectrum of the fluctuations field. But using this information in the simulation process did not much influence the final field's final autocorrelation (see Llort *et al.* 2006).

In order to visually notice the effect of the downscaling method and the pixel sorting, Figure 2.13 shows an example of downscaling of the first radar PPI with two iterations starting from the data upscaled twice from the observations. The bottom-left plot shows the result of only applying the wavelet technique, and the bottom-right plot after the pixel sorting. From a qualitative point of view it can be observed that, when applying both techniques, the result is closer in "texture" to the original rainfall field.
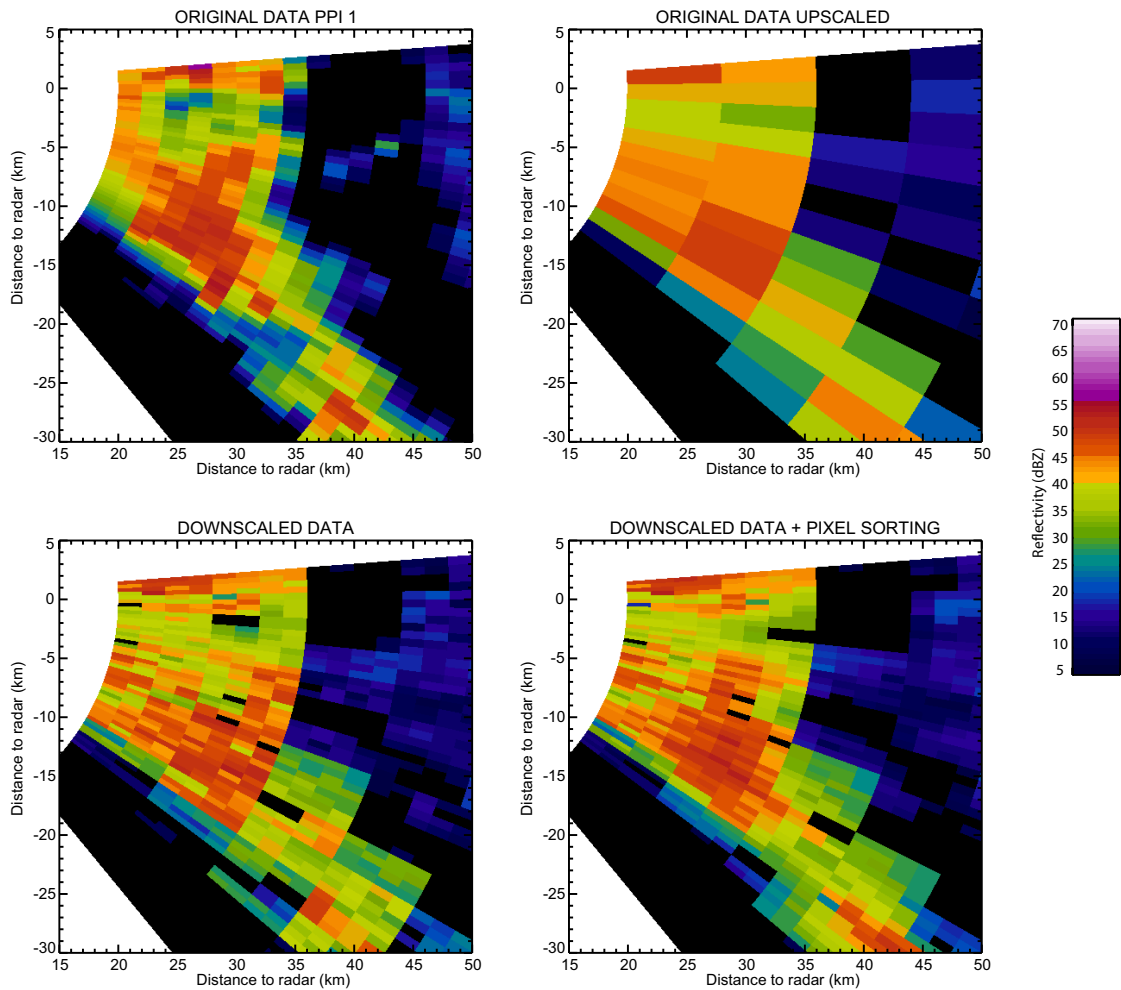
Figure 2.13: Downscaling example. The upper plots represent the original data (top-left) and the original data upscaled two iterations (top-right). The second row graphs represent the fields obtained after two wavelet iterations (bottom-left) and after two wavelet iterations performing a pixel sorting (bottom-right).

2.3.2. 3D Downscaling: Vertical structure

Once the lowest radar PPI is downscaled to the required resolution with the 2D wavelet model described above, it is used to downscale the rest of PPIs through a homotopy of the original observed VPRs.

The homotopy is performed over the VPR normalized by their value in the first radar tilt, so they all have the same value at the bottom and represent the profile shape independently of their lowest value. The VPRs are considered to be piecewise-linear functions of the observed values (i.e. between the observed values at each elevation we interpolate linear functions).

To obtain the reflectivity corresponding to a downscaled target location at a certain height, we first obtain the VPR at this point, and after we take the value of the profile at the corresponding height. To obtain the necessary VPR, we perform a homotopy of the normalized observed VPRs

surrounding the point of interest, as shown in the scheme of Figure 2.14. In this study, for its simplicity, linear homotopy is used, whose mathematical expression is as follows:

$$G : [0,1]^2 \times H \longrightarrow C(H)$$
$$(i,j,h) \longrightarrow G(i,j,h) = Vp_{i,j}(h)$$

(2.10)

Where H is the height, $[0,1]^2$ is the 2D unit interval (base of the homotopy), $C(H)$ denotes the continuous functions in height (the vertical profiles) and $Vp_{i,j}$ is defined as:

$$Vp_{i,j}(h) = \left\{ i \cdot Vp_{1,0}(h) + (1-i) \cdot Vp_{1,0}(h) \right\} \times (1-j) + \left\{ i \cdot Vp_{1,1}(h) + (1-i) \cdot Vp_{0,1}(h) \right\} \times j \quad (2.11)$$

Where $Vp_{0,0}$, $Vp_{0,1}$, $Vp_{1,0}$ and $Vp_{1,1}$. are the normalized observed profiles surrounding the point of interest. The i and j index are the normalized distance of the point to the surrounding observations. In particular the homotopy recovers the original normalized profiles in the interval extremes, that is, $G(0,0,\cdot)= Vp_{0,0}$, $G(0,1,\cdot)= Vp_{0,1}$, $G(1,0,\cdot)= Vp_{1,0}$ and $G(1,1,\cdot)= Vp_{1,1}$.
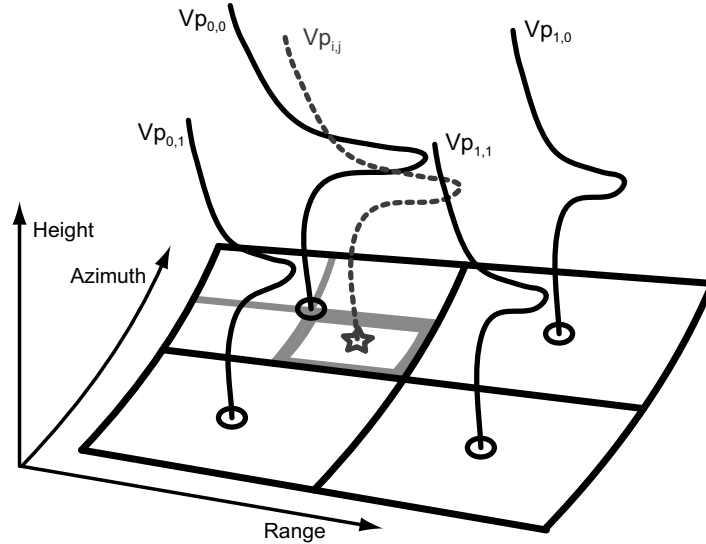
Figure 2.14: Homotopy scheme. The points marked with a circle correspond to the original data and the solid lines, their profiles. The star point is that obtained through 2D downscaling of the first PPI and its vertical profile is the dashed one, obtained through the homotopy.

Once the normalized VPR at the point of interest is calculated, it is denormalized. This is done using the downscaled value of the base scan in the column of interest (obtained using the 2D wavelet model explained in section 2.3.1). In the last step the value in the desiderated height is taken from the VPR calculated.

Figure 2.15 shows the downscaled fields obtained through this technique when applied to two different upper PPIs. The downscaled first PPI used (base for the homotopy) is that shown in Figure 2.13 (bottom-right). In this figure it can be observed that the homotopy reintroduces the variability lost after averaging, preserving the observed pixel structure. Details of the field used as a

base in the homotopy can be recognized in the upper elevations (as extreme values or pixels with zero rain amount).

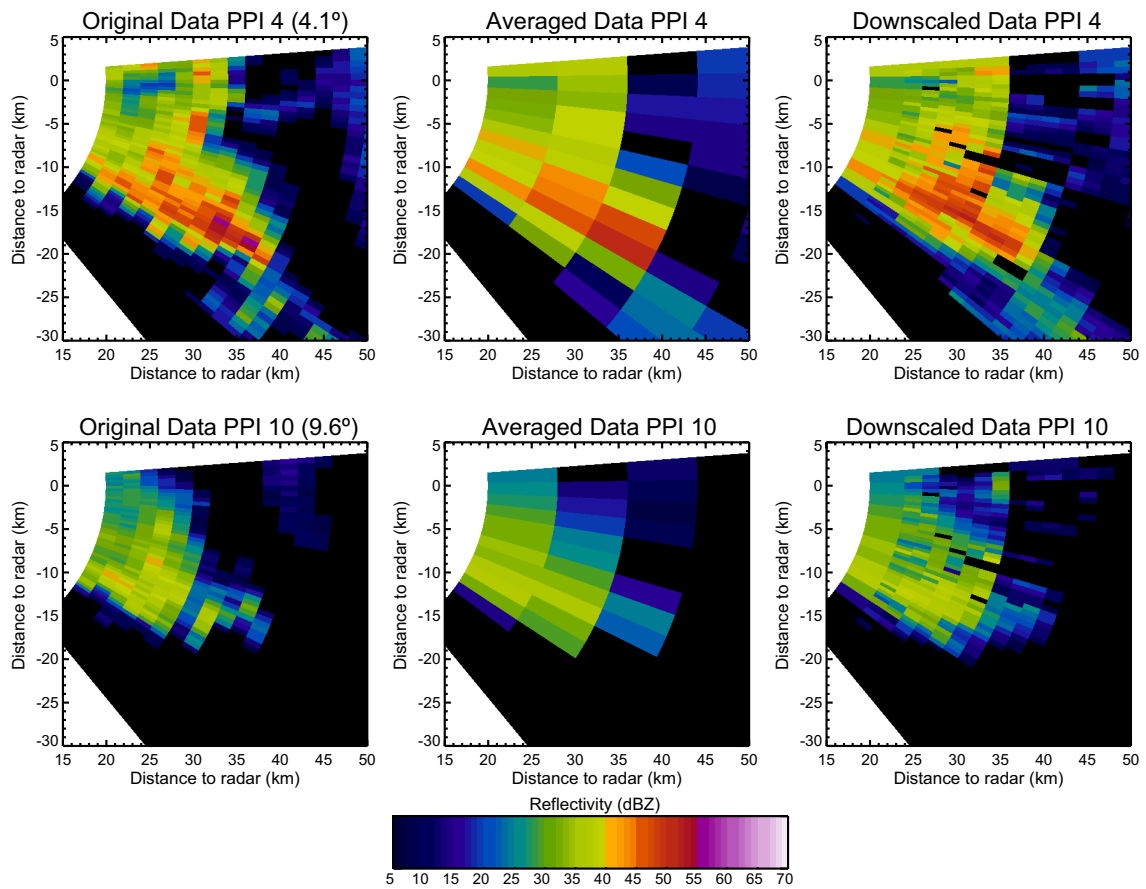Figure 2.15: Downscaling of the upper elevations example. The first column represents the original data of two different elevations (4.1° and 9.6°), the second column the same data upscaled twice, and the third column the result after the 3D downscaling technique.

The homotopy technique described in this chapter also allows us to create "artificial" elevations between the observed by taking the value of the obtained VPRs at different heights. This property allows us to increase the vertical density of the values further away from radar and, thus, improves the results in the transformation of downscaled fields to Cartesian values.

2.3.3. From spherical to Cartesian values

Many applications need high-resolution rainfall fields in Cartesian coordinates. In this sense, the last step of the proposed 3D downscaling process consists in transforming the dense spherical values obtained in the downscaling process into a Cartesian grid. Trapp and Doswell (2000) studied the various techniques for this transformation concluding that, to preserve the extreme values and the small-scale variability, the best choice is the "nearest neighbour" algorithm. Therefore this has been the choice in this work.

Previous to the transformation, the positions of the densified spherical radar bins are calculated from equations that describe the propagation of electromagnetic waves in the atmosphere using the 4/3 equivalent Earth model (see e.g. Doviak and Zrnic 1992).

2.4. Summary, conclusions and future work

First we presented a framework for the objective comparison of downscaling methods. It is based on first upscaling rainfall observations to, then, downscale them with different methods. This allows us to compare of the resulting simulations against actual measurements at the original resolution of the observations. In the presented study, the comparison is done through (1) "cross comparison" of the results, that is all downscaled data are evaluated in terms of the rest of the models used to characterize rainfall variability, and (2) the analysis of the multifractal properties of observations and simulations.

We have analyzed two methods for rainfall downscaling, both based on modelling the scaling properties of rainfall, being the main difference between them the base functions used to describe the rainfall variability with scale: the first uses the Fourier decomposition, and the second uses the Haar wavelet. Both methods are relatively simple and widely used to generate synthetic rainfall, but both provide only a partial description of the scaling properties of the rainfall. The analysis of the distribution of the values generated with each of the methods, shows us that the series downscaled using the wavalet-based method reproduce the structure of heavy rain rates better than those obtained using the Fourier-based method. Also, we have shown that the wavelet-based method is able to better reproduce the multifractal properties of self-similarity exhibited by observed rainfall time series. Since the complexity of such a downscaling method is rather limited and not time consuming, this can be considered a good tool for downscaling rainfall data.

Although the presented results only show time series of rainfall up- and downscaled from 1 to 8 minutes and viceversa, very similar results were obtained at different resolutions (from 2-minutes to 32-minutes averaged data). The subjective choice of 8 minutes (3 up- and downscaling iterations with respect to the original records) has been chosen as a compromise between enough iterations of the process to test the methods and enough remaining scales to calculate the respective scale laws.

The parameters used for the scaling-laws of the two downscaling methods (i.e. the β exponent –in the Fourier-based method– and the scaling law of the fluctuation's standard deviation –in the wavelet-based method–) are the average values as fitted over 120 time series of rainfall. Therefore, they are more robust than if we had fitted them to individual events and the results could be extrapolated to the case of simulating rainfall series, where no knowledge of the larger scales is known.

The results presented here are valid in the range where scaling of precipitation is relatively constant. The use of these methods at larger scales, where the processes involved in precipitation genesis and evolution are different (as discussed by Fabry 1996; Lovejoy *et al.* 2008), should be carefully tested. In the range of scales analyzed in this study, we observed similar values of β as reported by other authors (Nikolopoulos *et al.* 2008; Pegram and Clothier 2001a). Also our dataset shows a very similar behaviour of the order-*q* moments as function of the scale as that presented by Nikolopoulos *et al.* 2008 for rainfall observed with a Parsivel disdrometer.

After this comparison study, the chapter proposes a technique to generate 3D rainfall fields based on measured radar rainfall. In this study a 2D downscaling technique based on a wavelet model is used to downscale the first radar tilt. This technique is able to reproduce the extreme values of the rain and, in addition, improve the correlation between the generated values in the new scales. Nevertheless (as we had already seen in section 2.2 for rainfall series) it is not capable of fully recovering the field correlation in terms of the Fourier power spectrum slope.

The 2D dimensional downscaling process is complemented with a vertical homotopy of VPR in order to obtain a complete 3D downscaling algorithm. This vertical downscaling preserves the vertical structure of rainfall observed by the radar and allows us to increase the vertical values density.

It is worth noting that this study has been done in polar data, which implies that not all the pixels have the same area. Therefore, the standard deviations and the fluctuations structure obtained at the different scales will change depending on the distance to the radar of the pixels used for its calculation. Further investigation of this point is required.

The presented technique is unable to fully represent the characteristics observed in measured precipitation, but produces a plausible 3D rainfall field useful for many applications (e.g. radar simulation studies).

Future work might consist of studying the variability of the VPR inside a radar field and therefore the introduction of a random component in the vertical component of the 3D downscaling scheme.

CHAPTER 3

The structure of errors affecting radar rainfall estimates

3.1. Introduction

Radar precipitation estimates are affected by inherent errors of different sources: ground clutter, orographic screening, signal attenuation due to precipitation, beam broadening, etc. (Zawadzki 1984). Although technological advancements produced in the last years, as well as the better knowledge of the physics underlying radar measurements, allowed for better algorithms and methodologies to improve radar Quantitative Precipitation Estimates [QPE] by radar, some uncertainty remains affecting the result. The study of the errors affecting radar rainfall estimates is becoming as important as the retrieval estimates themselves for many applications –e.g. data assimilation in Numerical Weather Prediction [NWP] models and flow forecasting by hydrological models– (Krajewski and Ciach 2004, Borga 2002).

A classical classification of the errors regarding the measurements of a physical variable by an instrument (as rainfall by a weather radar) can be (see e.g. Bevington 1969):

- Random errors: Related to the characteristics of the instruments used (electronics, precision, etc.). Typically unbiased and can be reduced upon averaging the sample.

- Systematic errors due to temporal sampling: Errors due to the measurement instrument temporal frequency of the sampling and related to the temporal variability of the precipitation. Those are high e.g. in Low Earth Orbiting [LEO] satellites (like the Tropical Rainfall Measurement Mission [TRMM]) because of the revisit time of the instrument. In ground radars, that typically produce a full volume scant every 5-10 minutes, these errors can be considered negligible for most of the applications.

- Systematic errors due to spatial sampling: Errors due to the spatial resolution of the instrument. In weather radars these are related to the sampling volume (spatial resolution) of the radar. These errors are related with the variability of the precipitation at different

scales (representativeness of the measurements at a given scale), see Chapter 2 of this document for studies about the scaling properties of precipitation.

Despite this classification of errors, when measuring precipitation with weather radars many errors appear from the measurement process itself (Zawadzki 1984) which, at the same time, are affected by the previously described errors. This Chapter focuses on this last kind of error (those related with the measurement process of radars), which is the most important in ground radar precipitation estimates. We are interested in characterizing the errors remaining after all the corrections applied to the precipitation estimates. Germann *et al.* (2006) identified two ways to characterize the error structure associated to radar precipitation estimates: a) Study the different sources of error independently (Bellon *et al.* 2005; Lee *et al.* 2007) and their interaction (Berenguer and Zawadzki 2008, 2009), and b) Compare the estimates against a "reference" and obtain the characteristics of the composed errors (Ciach *et al.* 2007; Germann *et al.* 2009). The first approach provides more information of the errors themselves, but needs the study of the covariance between the different errors for a correct composition, while the second approach is simpler and provides an estimation of the total uncertainty.

This chapter presents a study of each class: a simulation study of the uncertainty associated with range to the radar, complemented with the study of satellite errors by simulation, and the estimation of the total uncertainty obtained by comparison against a "benchmark".

One possible way to express the uncertainty in precipitation estimates is through the use of ensembles (set of equiprobable scenarios) generated taking into account the structure of errors (Germann *et al.* 2009). In this framework, precipitation estimates can be used for probabilistic applications. This chapter also presents an example of radar-based ensembles generated using the global description of the error obtained through the comparison against a benchmark.

3.2. Simulation study of the error associated with range

One possible way to study the errors affecting radar measurements and obtain their characteristics is through simulation. Physically based simulation of radar measurements has its main advantage in knowing the "truth", but simplifications and assumptions have to be made in the models used.

First works on simulations of radar precipitation estimates were based on establishing a Drop Size Distribution [DSD] field (based on disdrometer measurements) and simulate which would be the radar observations of that field (Chandrasekar and Bringi 1987). The same authors later on studied, also by simulation, the errors related to attenuation and the errors in polarimetric variables (Chandrasekar and Bringi 1988a, 1988b; Chandrasekar *et al.* 1990).

Anagnostou and Krajewski (1997) simulated the observations of radar over a 3D precipitation field (obtained generating 2D precipitation fields from stochastic models and adding a vertical structure) to obtain the characteristics of the errors associated with the measurements.

Physical simulation of the radar measurement process also has been used to study the orographic beam blockage using Digital Elevation Models [DEM] (Kucera *et al.* 2004); the Non Uniform Beam Filling [NUBF] effects on attenuation correction by spaceborne radars (Zhang *et al.* 2004); the errors related with attenuation and its correction (Uijlenhoet and Berne 2008); the residual errors in the Vertical Profile of Reflectivity [VPR] correction (Zawadzki and Bellon 2003)…

A last step in the study of the errors by simulation has been to analyze its impact on the flow estimates through a hydrological model (Borga *et al.* 1997; Sharif *et al.* 2002, 2004; Sánchez-Diezma 2001).

In this increasing interest for uncertainty in radar rainfall estimates, we propose a simulation approach to study the characteristics of the errors affecting radar estimates. It consists of three consecutive steps: (1) the generation of 3D high-resolution reference precipitation fields; (2) the simulation of radar measurements of these reference fields; and (3) the comparison between the simulations and the reference fields for the characterization of the differences. In this section we focused on the study of radar errors related to range (distance to the radar). A set of reference fields has been generated from radar data using the downscaling technique presented in Chapter 2 of this document. Afterwards, simulation of radar observations at different ranges has been performed. The resulting errors have been characterized as a function of range, showing the potential of this approach. Simulation of radar estimates against a raingauge network has also been performed to evaluate the radar-raingauge comparisons at different distances. In a last step, simulation of spaceborne radar has been performed to compare the estimates of this instrument against radar at different distances.

3.2.1. Simulation framework

This section introduces the simulation framework used in this study. It is based on the following two consecutive steps:

3.2.1.1 Generation of reference fields

The aim of this first step is to obtain three-dimensional high-resolution precipitation fields over a Cartesian grid with the appropriate small scale variation (in order to statistically reproduce, as much as possible, realistic rainfall features). Different approaches have been adopted in other works in the literature. From the point of view of the stochastic models, the spatial and temporal structure of rainfall from storm events can be generated using Poisson processes; cells are born randomly

through the storm and then rain is spread in time and space according to functions which may include random parameters (Rodriguez-Iturbe and Eagleson 1987). Also Anagnostou and Krajewski (1997) used space-time stochastic models to generate rainfall fields, but in this work the two-dimensional rainfall field is completed with a vertical structure of hydrometeors by choosing a precipitation cloud type model in order to obtain a three-dimensional rainfall field. In this last paper the stochastic model is improved in order to generate more realistic rainfall patterns and, not only storm events, but also squall lines and stratiform events. Willems (2001) proposes a hierarchical model for small scales calibrated with historical series from a network of raingauges. This model improves the generation of small-scale precipitation cells, but does not consider the vertical structure.

Stochastic models can provide a wide range of spatial and temporal rainfall patterns for many resolutions and with acceptable computational speed. The main problem involved in the stochastic simulation is the lack of physical consistency between atmospheric processes and generated rainfall. Lanza *et al.* (2001) did a review of the different techniques and problems involved.

Another way to deal with the generation of high-resolution precipitation is downscaling measured precipitation data. First guess of this approach is imposing random noise (Gaussian and isotropic) on a given high-quality radar-rainfall field (Krajewski and Georgakakos 1985). In this work, certain conditions are imposed on the resultant rainfall field (the mean, the variance, the autocorrelation, and the variance of the logarithmic ratio of the resulting field to the original field) so that determine the parameters of the generated noise. This method does not suppose known characteristics of radar-rainfall error as Rodriguez-Iturbe and Eagleson (1987) do. The noise characteristics vary from point to point based on the local original field characteristics such as magnitude and gradient.

In the present work the simulation procedure to generate the three-dimensional high-resolution precipitation field is that initially proposed by Sánchez-Diezma (2001) that uses an approach similar to the one proposed by Krajewski and Georgakakos (1985), and volumetric data from ground weather radar is taken and interpolated into a Cartesian grid up to a certain resolution. This allows us to obtain 3D high-resolution fields from real radar observations, with adequate variability and correlation at small scales without imposing a vertical structure.

To generate these reference fields, we use reflectivity information measured close to the radar as the starting point of a downscaling technique. The downscaling technique used (described in detail in Llort *et al.* 2006 and in Chapter 2 of this document) is based on a combination of wavelet scale-analysis and homotopic techniques. In this technique, the first radar tilt is downscaled using a 2D wavelet model: by means of a given Haar-base wavelet scale variability analysis, the observed variability at large scales is extrapolated to the new small scales created. Once the first radar elevation (PPI) is downscaled up to the requested resolution, the other tilts are downscaled by a

homotopy (continuous deformation) of the observed VPRs in order to preserve the vertical structure measured by the radar. In a last step, the dense polar values are fitted to a Cartesian grid using the "nearest neighbour" algorithm.

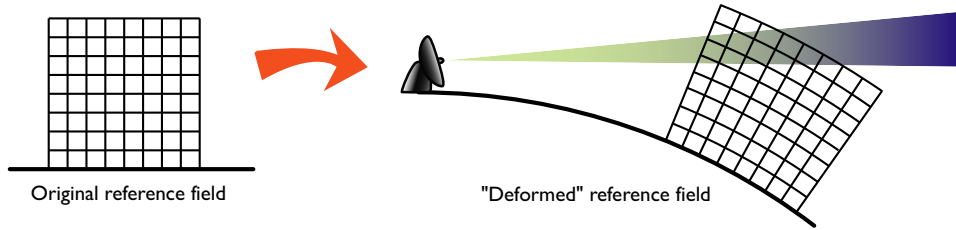Original reference field   "Deformed" reference field

Figure 3.1: Deformation of the Cartesian field (Courtesy of Sánchez-Diezma 2001).

In order to capture as much as possible the highest resolution and quality, the radar data source for the interpolation is taken close to the radar (reducing the effect of loss of power with distance and rain, attenuation, sampling volume, etc.). Previous to the interpolation, the three-dimensional position of the radar data are determined by considering the beam refraction in the atmosphere and the curvature of the Earth, so the Cartesian grid deformed accordingly (see Figure 3.1). Thus the elevation above the ground of each sampling volume is calculated from equations that describe propagation of electromagnetic waves in the atmosphere (using a 4/3 equivalent Earth model proposed by Doviak and Zrnic 1992). Therefore, the height for each radar volume scan above the ground can be obtained according to equation 3.1 where ρ_E is the radius of the Earth, h_{rad} is the height of the radar above sea level, θ_e is the scan elevation angle, and s is distance along the surface (see Figure 3.2).

$$h_s = \frac{4}{3}\rho_E\left(\frac{\cos\theta_e}{\cos\left(\theta_e + s/\left(\rho_E\, 4/3\right)\right)} - 1\right) + h_{rad}\frac{1}{\cos\left(s/\left(\rho_E\, 4/3\right)\right)} \tag{3.1}$$
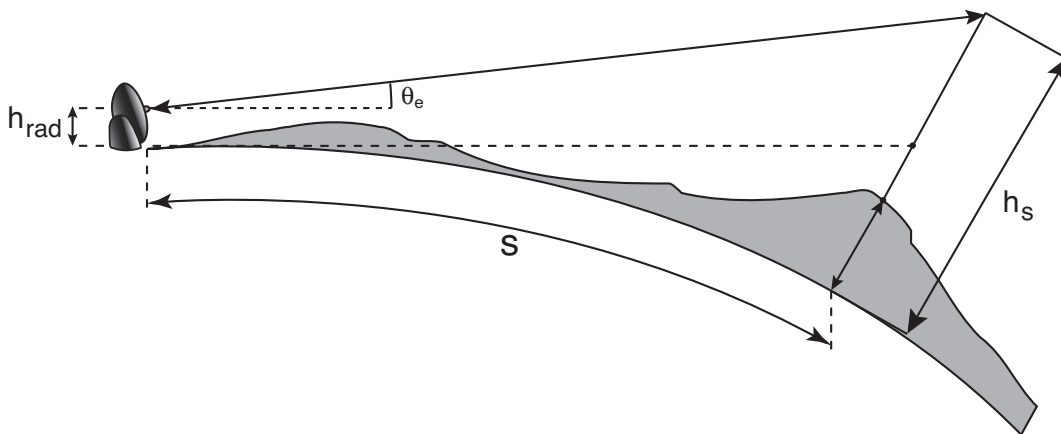

Figure 3.2: Beam height over the Earth (Adapted from Sánchez-Diezma 2001).

A final resolution after the downscaling process of 250 meters was chosen as a compromise between computational resources, ability of the downscaling technique to reproduce variability at

small scales, and the resulting resolution of the simulated observed fields (1x1 km^2 and 4x4 km^2 for ground based and satellite based radar respectively that will be simulated in this work).

3.2.1.2   Simulation of radar observations

The second step of this framework consists of simulating radar measurements over the given reference precipitation fields located at a certain distance from the radar. This degraded field is obtained as the convolution between the power distribution within the radar beam and the 3D reflectivity field according to the radar equation (similarly as Anagnostou and Krajewski 1997 and following the implementation of Sánchez-Diezma 2001).

The radar equation (3.2) expresses the power received by the antenna from range r_0, $\overline{P}(r_0)$, and the reflectivity of the target (Probert-Jones 1962). In this equation, the first part ($C = \dfrac{P_t g^2 \pi^2}{64 \lambda^2}$) is a constant related to the radar characteristics (transmitted power, P_t, antenna gain, g, and wavelength, λ).

$$\overline{P}(r_0) = C \int \frac{|W_s|^2 f^4 Z}{r^2} dV \tag{3.2}$$

The second term is the integral of the contribution ($\dfrac{|W_s|^2 f^4}{r^2} Z$) of the particles in dV through its reflectivity, Z, to the total received power (Figure 3.3).
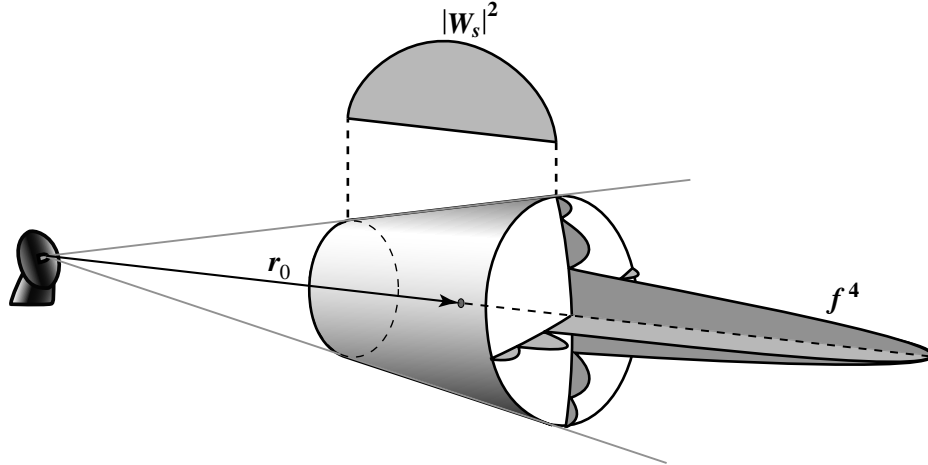

Figure 3.3: Energy distribution inside the radar beam (Adapted from Sánchez-Diezma 2001).

The range weighting function $\left|W_s(r)\right|^2$ describes the relative contribution of power along the range from radar within the sampling volume. For this simulation tool, the equation for $\left|W_s(r)\right|^2$ used is the proposed again in Doviak and Zrnic (1992):

$$\left|W_s(r_0)\right|^2 = (\frac{1}{2}\left[erf(s+b) - erf(s-b)\right])^2 \tag{3.3}$$

Where $erf(y) = \frac{2}{\sqrt{\pi}}\int_0^y e^{-t^2}dt$ and $b = B_6\tau\pi/(4(Ln(2)^{1/2}))$; $s = (2aB_6/c)r_b$; $a = \pi/(2(Ln(2)^{1/2}))$. B_6 is the 6-dB width of the receptor, τ is the pulse width of the transmitter, $r_b = r - r_0$ and c is the speed of light.

The normalized power (f^4) is approximated by a Gaussian function (where ϕ_3 is the 3 dB power angle), see equation 3.4. Side lobes are not taken into account in the simulation.

$$f^4(\phi) = \exp\left(-\frac{8Ln(2)\phi^2}{\phi_3^2}\right) \tag{3.4}$$

At the end of this process, only the *n* bigger weights and their coordinates are taken to narrow down the use of computer resources. Hence, only the *n* most contributing cells (of the reference field) are taken into consideration. For studying the influence of the number of weights taken Sánchez-Diezma (2001) compared the numerical solution and the analytical one in a predefined precipitation field. He obtained that for *n*>400 the error is less than 0.001%, in this study we use *n*=500. This procedure to simulate the observations of an instrument (calculating separately the contribution of the cells and after applying the convolution between the weights and the precipitation field) allows us to reduce the computation time if several simulations are done with the same radar specifications and location, and for different high-resolution precipitation fields. The final step is to calculate the convolution between the weights and the corresponding values of the high-resolution precipitation field in order to obtain the simulated measurements.

After obtaining both the reference and the radar-simulated reflectivity fields, we can study the differences (that can be interpreted as the sampling errors affecting radar measurements, if we assume the reference fields to be "the truth"). This approach allows us to separately study the errors and characterize their statistical properties, which can be later used, for example, in the generation of ensembles.

3.2.2. Application to the study of the errors related to range in ground radars

With the simulation procedure described in the previous section (3.2.1), we have characterized the errors related to range for ground radars. These errors are mainly due to the change in the beam width and the variation of reflectivity with height (VPR).

The data used for this study is a set of 291 rainy volume scans measured with the C-band radar of the Spanish Meteorology Agency [AEMET] (located in Corbera de Llobregat, close to Barcelona) between October 12th, 2005 - 00:00 UTC and October 16th, 2005 - 23:50 UTC. This event contains a mix of rainfall types, but stratiform precipitation, showing a bright band at a height around 3.3 km (as estimated with the algorithm by Sánchez-Diezma *et al.* 2000), was predominant. This radar operates in a 20-elevation protocol providing a full volume scan every 10 minutes. Its measurements have a resolution of 2 km in range, and 0.9° in azimuth (see Table 3.1 for a complete description).

Table 3.1. Specifications of the AEMET C-band radar located near Barcelona

Latitude	41° 24' 33"
Longitude	1° 53' 9"
Height (a.m.s.l.)	664 m
Transmitted Power	250 KW
PRF	250 Hz
Frequency	5.60 GHz
Beam width	0.9°
Pulse duration	2 μs
Number of azimuths	420
Antenna speed	6 rpm
Number of elevations (volumetric scan)	20 (between 0.5 and 25 deg.)
Time resolution (between volumes)	10 minutes

Reflectivity observations in polar coordinates from a section of 20 x 20 x 10 km³, measured close to the radar and over the sea (to keep a good resolution and avoid ground clutter), have been downscaled with the described technique. We have performed three iterations of the wavelet technique using a variability scale-law based on an event containing 100 rainy radar scans (with a mix of rainfall types). The final resolution for the Cartesian field has been set to 250 m in the three dimensions.

Observations of a radar located at ranges between 15 and 140 km (every 5 km) from the centre of the reference fields (see Figure 3.4) have been simulated using a constant elevation angle of 0.5°. It is worth noting that the errors induced in these simulations are only due to beam broadening and the height increasing with range.
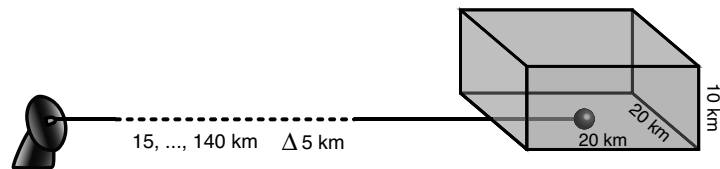
Figure 3.4: Simulation scheme. Reference volumes are located at distances between 15 and 140 km from the radar.

3.2.3. Results

For comparison purposes reference and simulated reflectivity fields have been transformed into rain rates, R, using Marshall-Palmer Z-R relationship (Z=200·R[1.6]; Marshall and Palmer 1948).

In a first instance we have calculated the correlation between simulated and reference fields. Figure 3.5 depicts this score as a function of range, and clearly shows how it decreases with distance.
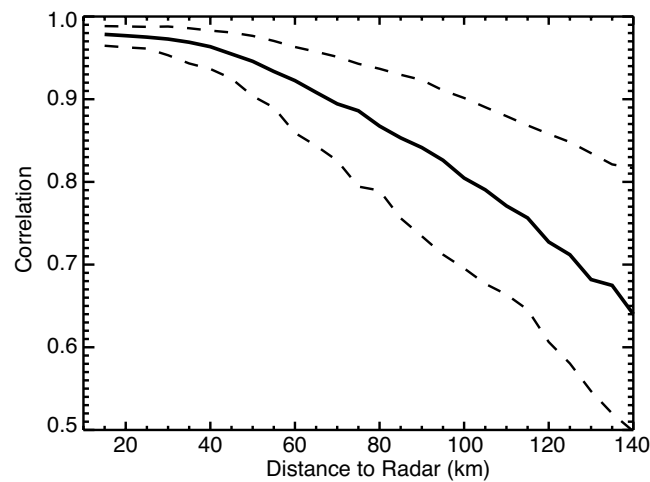

Figure 3.5: Correlation between simulated and reference fields as a function of range. Solid line corresponds to the median of the 291 fields, and dashed lines correspond to the 25 and 75 percentiles.

Some statistics of the residual fields (i.e. difference between reference and simulated fields) have also been calculated: their probability distribution function and their spatial correlation. Figure 3.6 shows the differences in the error distribution with range. In this figure it can be seen that the error distribution is similar for all ranges (close to a Gaussian, but slightly skewed to overestimation) but wider at farther ranges as expected and less skewed.
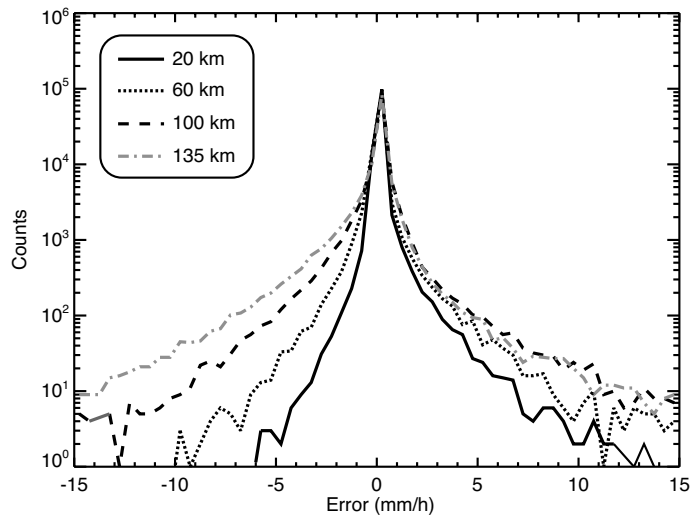
Figure 3.6: Histograms of the error simulated at different ranges.

The variation of the mean error and standard deviation of the error with range are presented in Figure 3.7. In this figure we can see how the radar overestimates the reference field up to a certain distance from which the bias becomes close to zero.
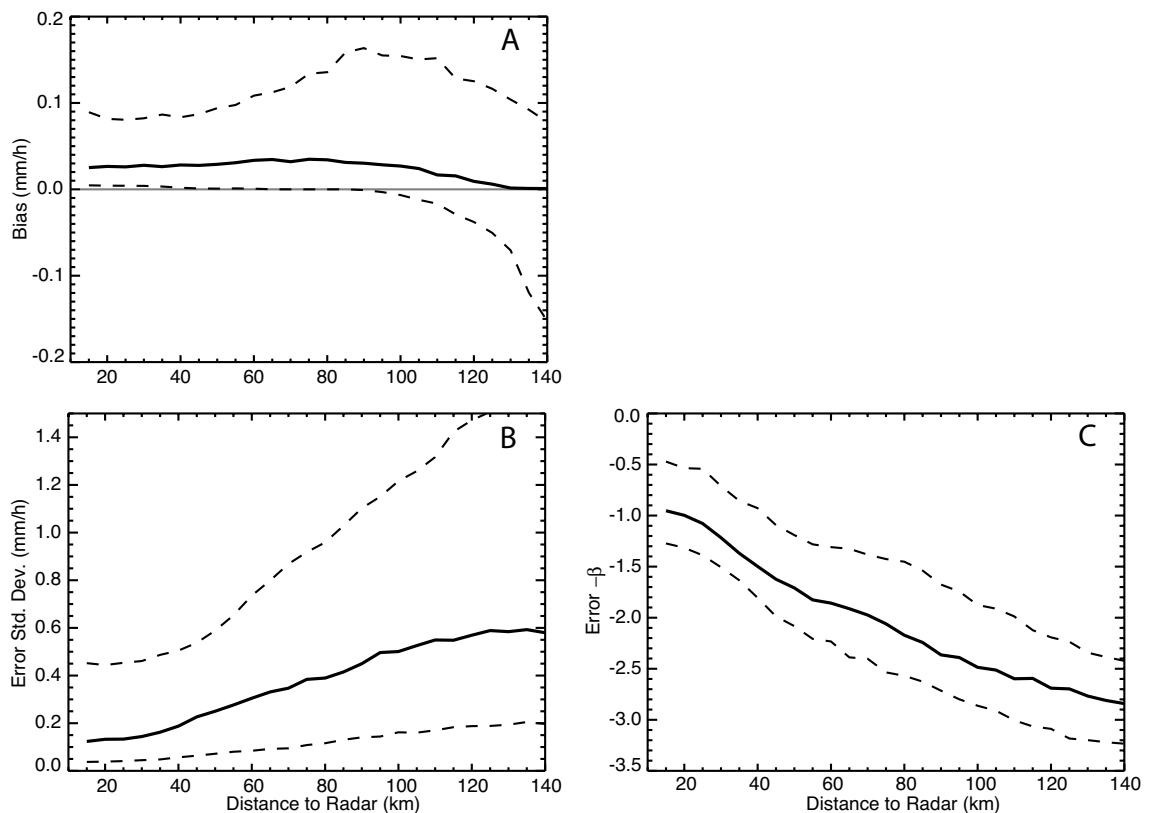

Figure 3.7: Statistics of the error fields as function of range. Bias (panel A), standard deviation (panel B), and parameter $-\beta$ (panel C). The solid line corresponds to the median of the 291 fields, and dashed lines to the 25 and 75 percentiles.

This phenomenon (enhanced in the accumulated fields; see Figure 3.8) can be explained by the interception of the beam with the bright band. At farther ranges, the beam is over the bright band

(in the snow region), which results in an underestimation of rainfall at ground. This effect should be further investigated using rain type classification in a future work. On the other hand, there is a general trend of the standard deviation of the error fields to increase with range.
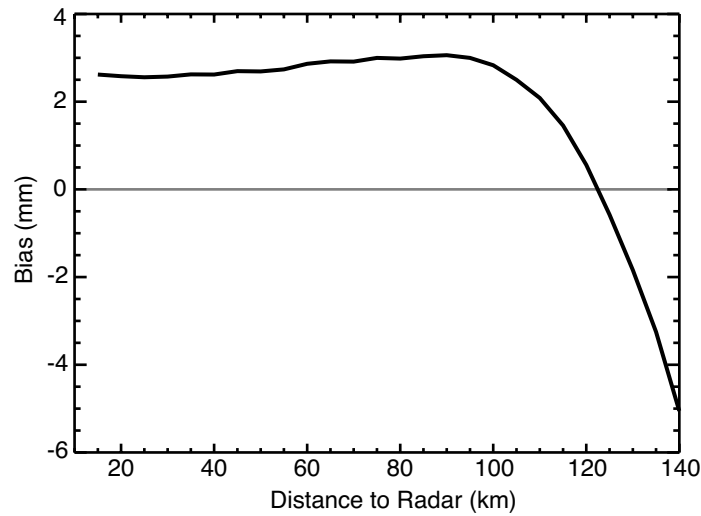

Figure 3.8: Bias of the accumulated fields as function of range.

In order to study the spatial correlation of the error fields, we calculate the Fourier power spectrum and we assume that can be fitted to a power-law (see Pegram and Clothier 2001a and equation 3.5) and we fit β to the radially averaged power spectrum.

$$\Gamma(f) \propto f^{-\beta} \tag{3.5}$$

The β parameter represents the degree of autocorrelation of the field, the higher, the smoother is the field. The dependence of the parameter β with distance to the radar of the simulated observations is also presented in Figure 3.7. It can be seen how it clearly decreases with distance (i.e. the spatial correlation of the errors is higher at farther ranges). This trend might be due to the beam broadening with distance (smoothing of the precipitation field) and indicated that the autocorrelation observed at far distances is due to the observation process, not the rainfall field itself.

Figure 3.9 shows the comparison of total time accumulation from ground radar and from reference fields for different distances to the radar (20, 40, 65, 90 and 115 km). It can be seen how the scatter increases with distance (decreasing the corresponding correlation and Nash efficiency, Nash and Sutcliffe 1970).
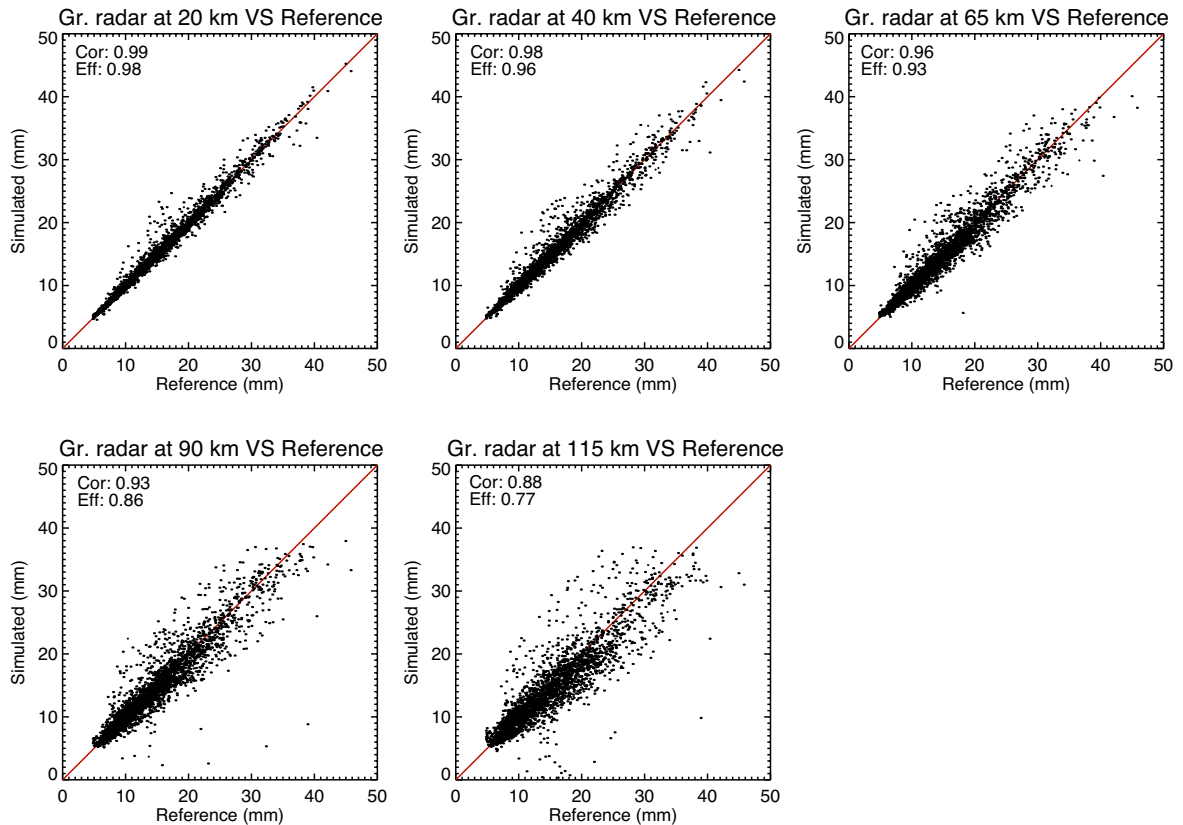
Figure 3.9: Ground radar simulated observations at 20, 40, 65, 90, 115 km accumulated for the full event compared to the reference accumulated fields. The correlation and Nash Efficiency between the two fields are written in each plot.

Figure 3.10 shows rainfall fields accumulated over the whole event estimated from the reference fields and from the simulated fields at three different ranges (20, 100 and 135 km), and the corresponding error fields. The error field at 20 km shows how the radar overestimates the reference in almost the entire domain. In the 100 km error field, we can see that, although the bias is more or less the same as that at 20 km (approx. 3 mm; see Figure 3.8), the standard deviation of the error field increased and now there are some areas where the radar underestimates. The 135 km error field shows that the radar is underestimating in the entire domain except in small areas where it overestimates, increasing the standard deviation of the error field. At this distance the radar beam is over the bright band, and the radar underestimates the reference precipitation at ground (see in Figure 3.8 the bias).
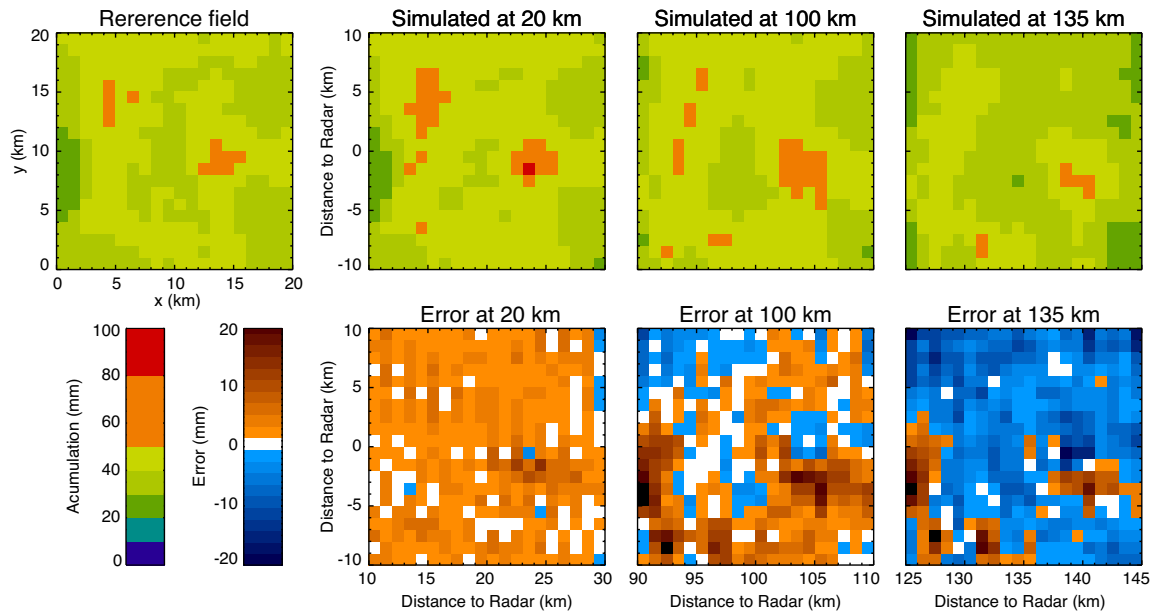
Figure 3.10: Accumulated fields estimated from the reference fields and from the simulations at 20, 100 and 135 km (first row), and their residuals (second row).

Regarding the temporal evolution of the characteristics of the error field, Figure 3.11 shows the bias and the standard deviation as a function of time for each distance. In the same figure the mean areal rainfall for the reference fields as function of time is also shown. In this figure we can see that the standard deviation of the error fields, not only increases with range as seen before, but it also is correlated to the mean rainfall. The temporal evolution of the bias shows that for a given time step, this parameter diverges from zero at farther ranges. It can also be seen that in some parts of the event (e.g. scan times between 80 and 120 or scan times between 240 and 255), the bias becomes more negative at farther ranges; and in some regions (e.g. scan times between 220 and 235) the bias becomes more positive at farther ranges. There is also evident correlation between the temporal evolution of the bias and the mean rainfall, but positive in some regions (scan times [220-235]) and negative in others (scan times [80-120] or [250-255]). This phenomenon might be due to the distinct rain types observed at different parts of the event.
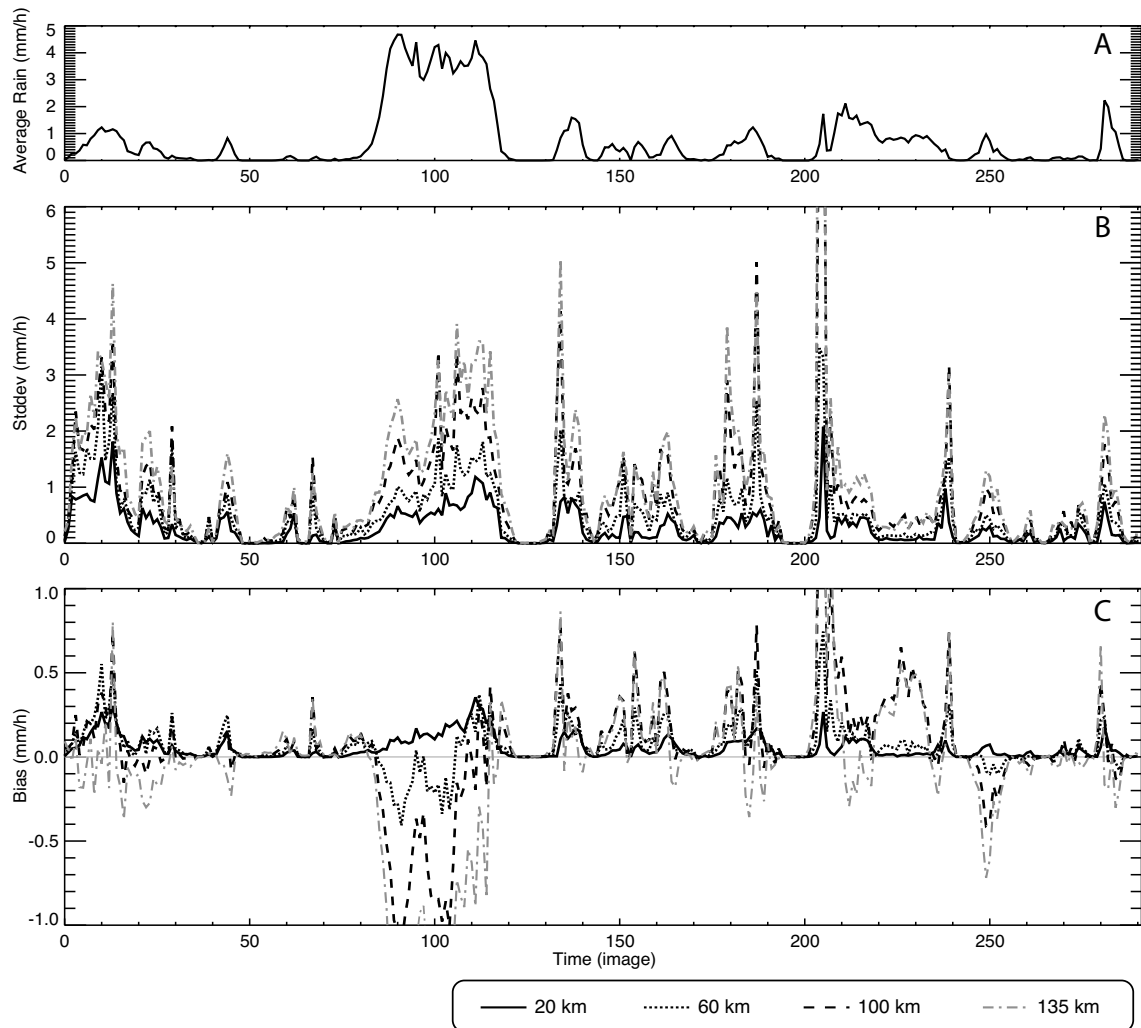
Figure 3.11: Temporal evolution of the reference mean areal precipitation (panel A), standard deviation of the error (panel B) and bias (panel C).

3.2.4. Simulation of raingauge measurements

In this study radar errors with distance are also analyzed by means of comparison of radar data against a simulated network of raingauges. The network of raingauges has been simulated by randomly setting a number of raingauges locations over an area of 50x50 km². We have chosen to make the number of raingauges change from 2 to 250. These values have been selected to match what could be considered an urban area (density of one raingauge every 10 km²) to lightly covered areas (density of one raingauge every 1250 km²). The position of the raingauges inside the reference field is set randomly following a uniform probability density function, and remains constant for the entire event. Several realizations (50 in this study) for each density have been done in order to avoid possible artefacts due to extreme configurations, and to provide a more general description of the radar error structure with distance.

In a first approach, the raingauge measures have been obtained taking the corresponding value of the reference rainfall field at the lowest height in its initial resolution (250x250 m²).
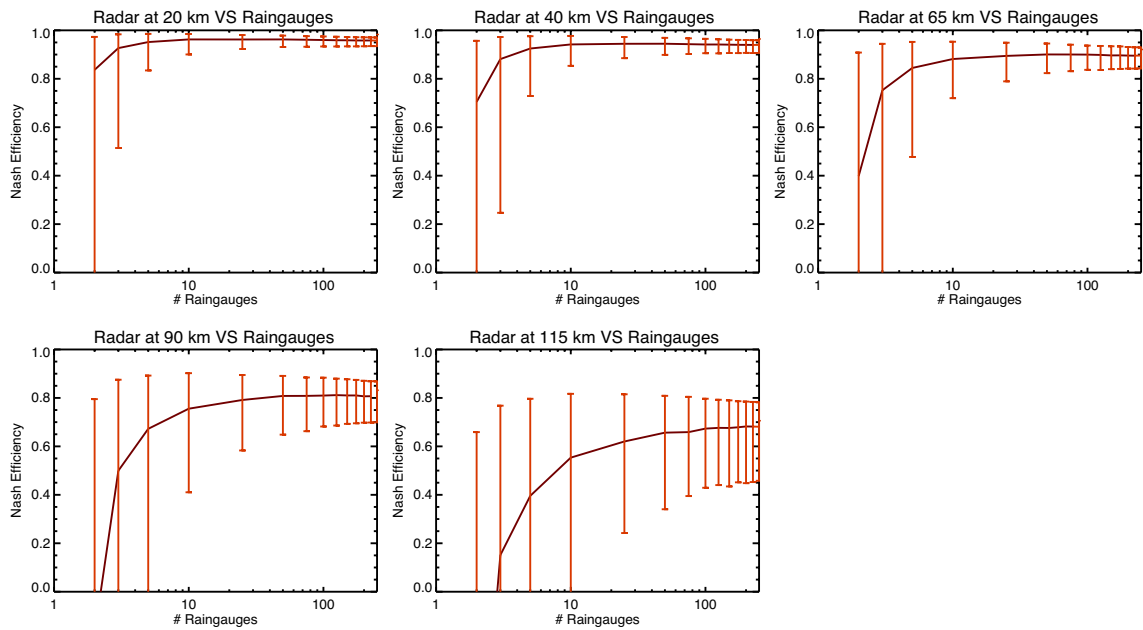
Figure 3.12: Comparison of the ground radar rain rate estimates simulated at different distances and raingauges mesurements for various densities of the raingauge network. The dark red line represents the median Nash efficiencies (between simulated radar and raingauge estimates) for all rainy fields in the event and for all the realizations (50). The lower and upper limits of the vertical bars (in red) represent the 25 and the 75 percentiles respectively.

Figure 3.12 shows the comparisons of radar simulations at different distances of observation, against a raingauge network in terms of the Nash efficiency. As expected, this figure shows how the median of the efficiencies decreases with the distance to the radar increases the number of raingauges. An interesting result is that up to 90 km from the radar all plots show that the median efficiency remains almost stable when the number of gauges reaches a value between 10 and 25 (densities of 1 gauge/250 km² and 1 gauge/100 km²). At far distances a large number of raingauges would be necessary to obtain a good estimation of the efficiency between the radar estimates and the reference (50 gauges: 1 gauge/50 km²). Regarding the deviation, all distances to the radar show that the confidence interval plotted decreases with the number of raingauges until it reaches a quite stable value around 100 raingauges (1 gauge/25 km²). Similar effects to the previous plots can be observed when we perform the same comparison in terms of rainfall accumulations (Figure 3.13). However, the median values obtained are higher than before (in agreement with the higher value of the efficiencies for accumulated fields of the radar simulations against the reference fields), and the confidence intervals constrain. The oscillations of the median value observed in the 90 km plot and (amplified) in the 115 km plot are probably due to the small number of values used for the analysis (only 50 realizations for each distance).
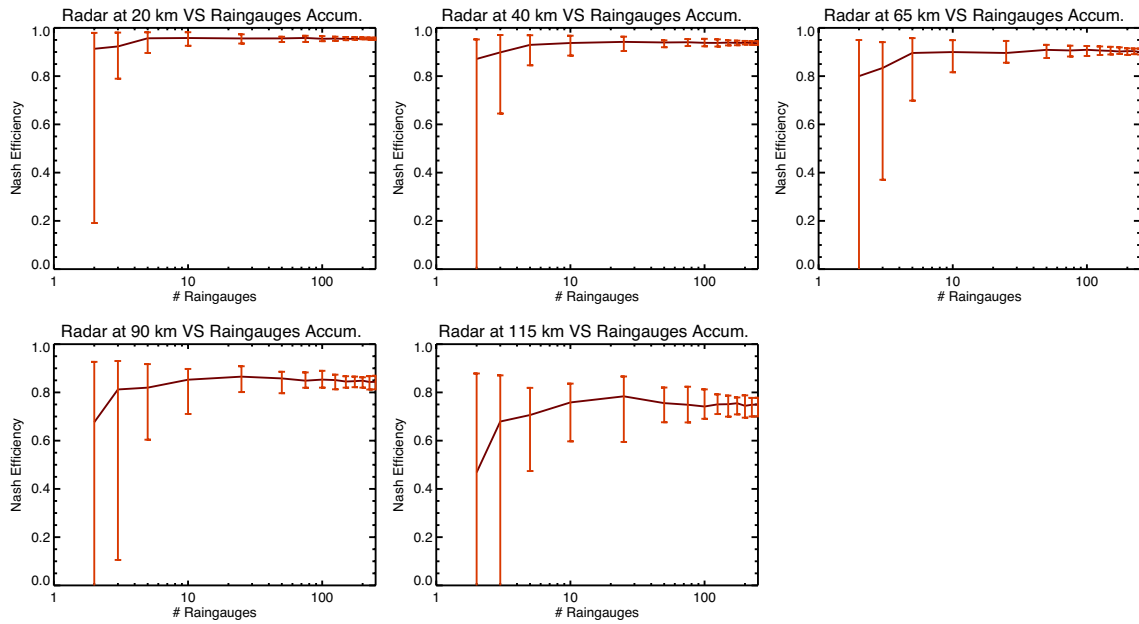
Figure 3.13: As in Figure 3.12 but in accumulation terms (accumulation of the entire event).

In order to study how the efficiency values change inside the event for the same comparing conditions (number of gauges in the network and radar distance), Figure 3.14 shows the comparison of the raingauge network estimates against the radar estimates at 90 km for different numbers of gauges.   Due to the fact that we have several realizations for the raingauge positions we can plot the median and an interval representing the deviation. In this figure we can observe how the efficiency of the radar versus the raingauge network changes along the event, probably due to the characteristics of the VPR, and therefore the representativeness of the raingauges point values. It can also be seen that increasing the number of gauges from 10 to 150 the median efficiency does not increase much (also see Figure 3.12, first plot of the second row) but the confidence interval becomes narrower.

These comparisons of radar observation simulations at different distances against the simulation of a network of raingauges, show the decrease of efficiency with distance to radar, but at the same time gives a "threshold" (depending on the distance and the network of raingauges density) of the necessary number of raingauges to obtain a good estimation of the efficiency between the radar estimates and the real precipitation field.
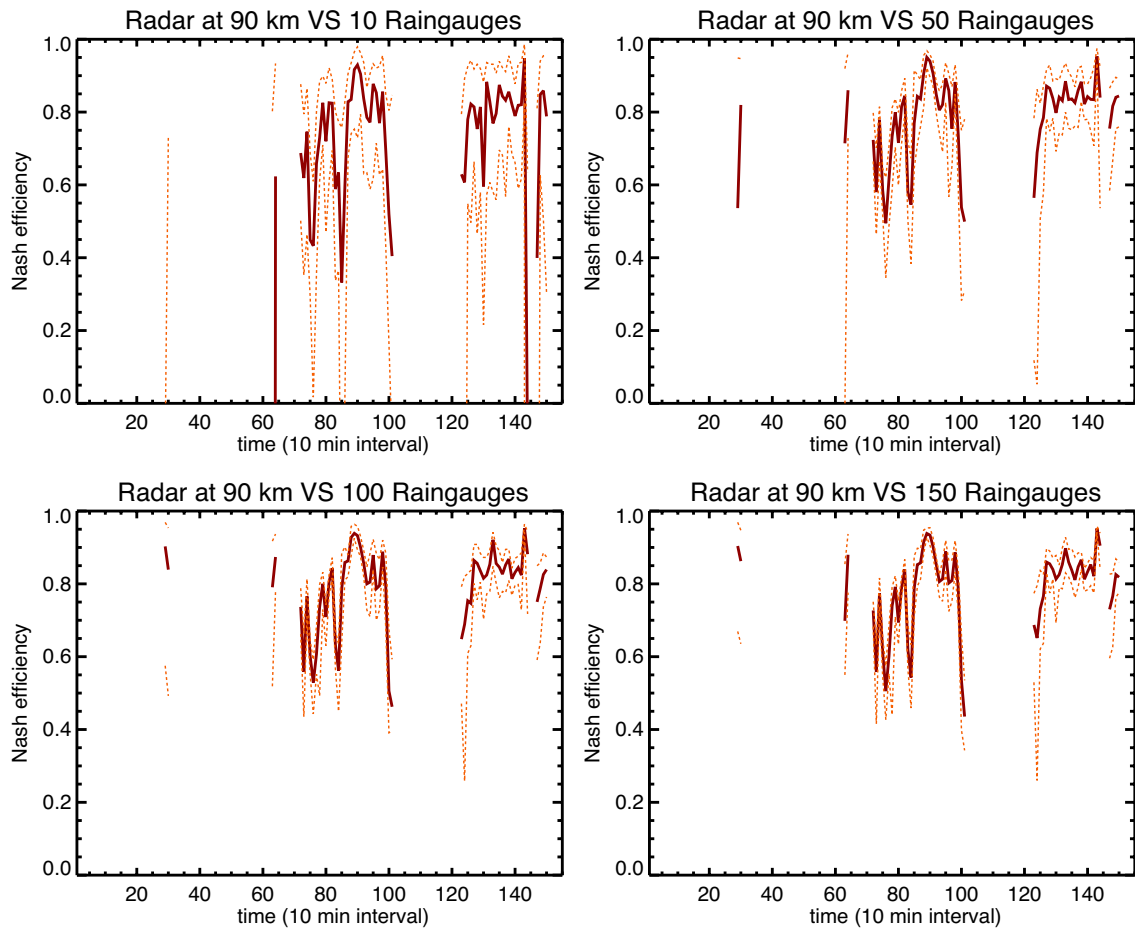
Figure 3.14: Evolution inside the event of the efficiency between the raingauges network (for 10, 50, 100 and 150 gauges) estimates and the radar estimates at 90 km. The dark red line represents the median of all the realizations and the lower and upper orange dotted lines the 25 and the 75 percentiles respectively.

3.2.5. Spaceborne radar simulation

Spaceborne radar measurements can also be simulated over the three-dimensional high-resolution precipitation fields. The simulation process is similar to the simulation of ground radar measurements (see section 3.2.1.2) with few differences due to the special characteristics of spaceborne radars. In this case the radar is considered to be a cross-track instrument and only a single swath is simulated. To get the full volume scan of the spaceborne radar, several simulations have to be done with different satellite positions each time (to simulate an overpass over the high-resolution precipitation field) (see Figure 3.15). Due to the process of simulation used (described in section 3.2.1.2) and the geometry of the satellite observations, this does not represent an additional difficulty: the weights of each cell only need to be calculated once, and then, the convolution between the weights and the precipitation field is done once for each satellite position. The beam range start and the number of gates (different for each beam) and the different angles (spaceborne radars typically do not have a circular beam) is taken into account.
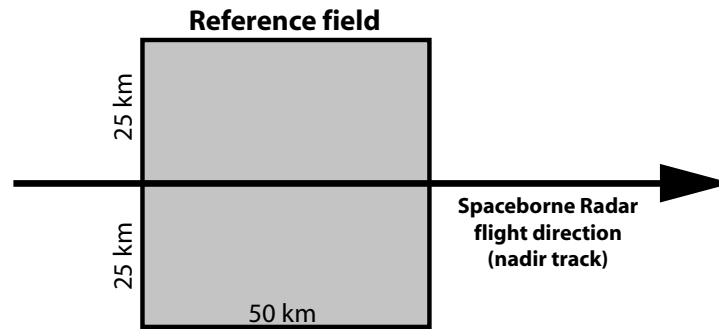
Figure 3.15: Scheme of the spaceborne radar simulation. Satellite is supposed to fly right across the middle of the reference field in horizontal direction.

Figure 3.16 shows the two reference fields used for the spaceborne radar simulations. First case corresponds to a convective and the second to a widespread stratiform one. They have been generated using the technique described in section 3.2.1.1. and have a resolution of 250 m.
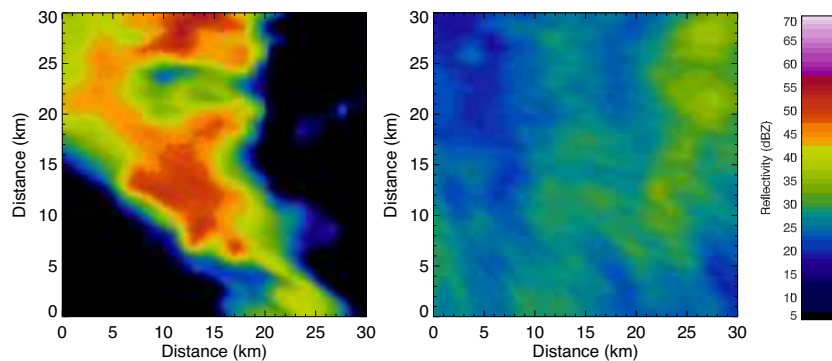
Figure 3.16: Reference fields used in the spaceborne radar simulations.

Figure 3.17 shows the simulations over the reference fields of Figure 3.16 of a ground radar located at 25 and 85 km away, and the simulations of a spaceborne radar over-flying the reference fields with the configuration shown in Figure 3.15. We can see the increasing smoothing with the distance (as observed above) and the degradation of the fields in the simulated observations for a spaceborne radar. Figure 3.18 shows the scatterplot of simulated fields against the reference fields (Figure 3.17 and Figure 3.16 respectively). We can observe how the scatter increases with distance for the ground radar (as observed above) and that the scatter for the spaceborne radar is much higher for the convective case than for the stratiform case. This might be due to the high horizontal gradients present in the convective case that in the observations of the spaceborne radars are smoothed.
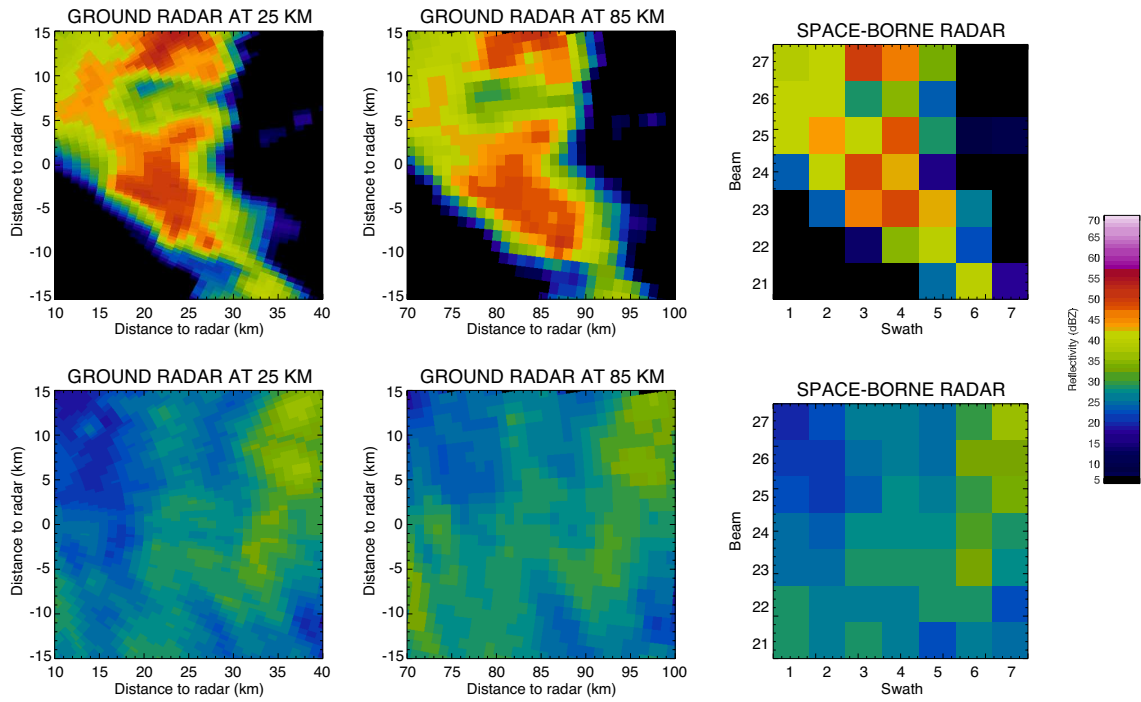
Figure 3.17: Simulation of the measurement of ground- and space-borne radar over the fields shown in Figure 3.16. The ground radar simulations have been performed locating the radar at 25 km (first column) and 85 km (second column) from the reference field. The last column shows the spaceborne radar simulation.
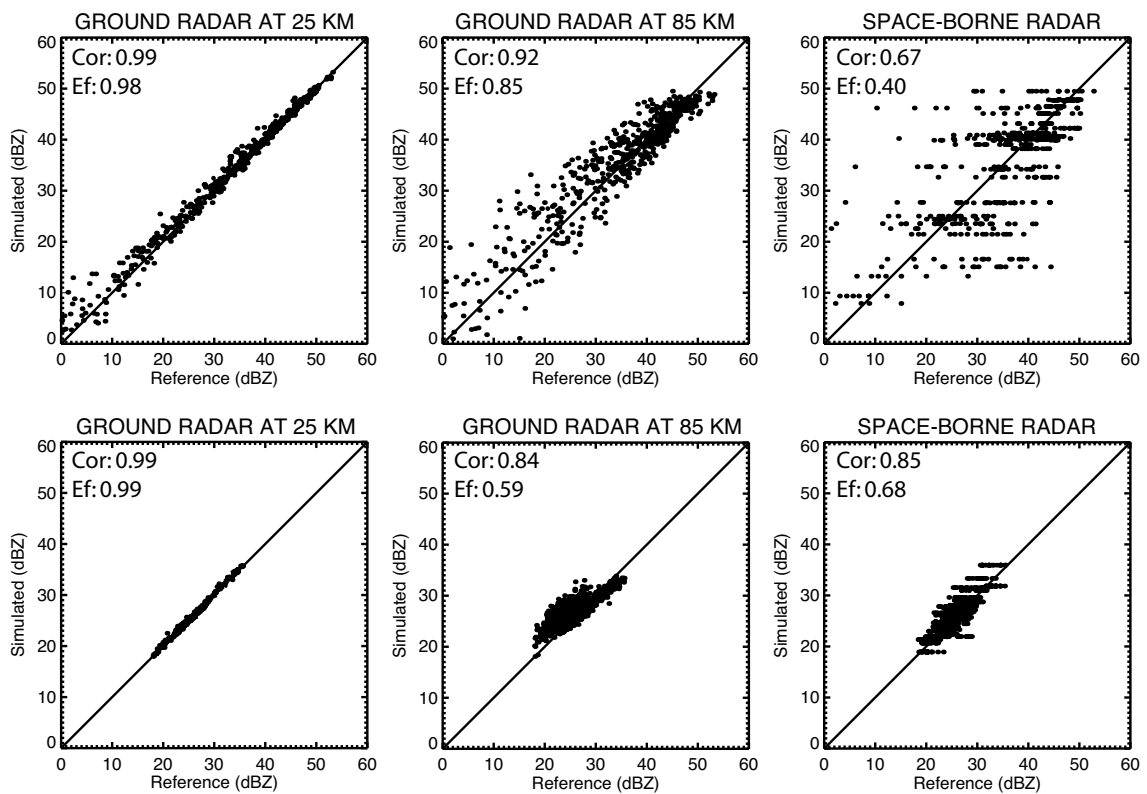
Figure 3.18: Comparison in terms of scatter-plots of the simulated observed fields (shown in Figure 3.17) against the references fields (Figure 3.16). The correlation between the both fields and the Nash Efficiency are plotted in each plot.

Figure 3.19 shows the comparison of the accumulated simulated measurements of this instrument against the accumulation of the reference fields for the same event of Figure 3.9. In this figure it can be seen that the scatter is higher than the one of ground radar estimates at any distance (Figure 3.9) and the correlation and Nash efficiency values are much lower. The "horizontal cluster" effect is due to the fact that one satellite pixel (4x4 km²) is compared to the corresponding reference pixels (1x1 km²) so, for each satellite pixel there are 16 reference pixels.
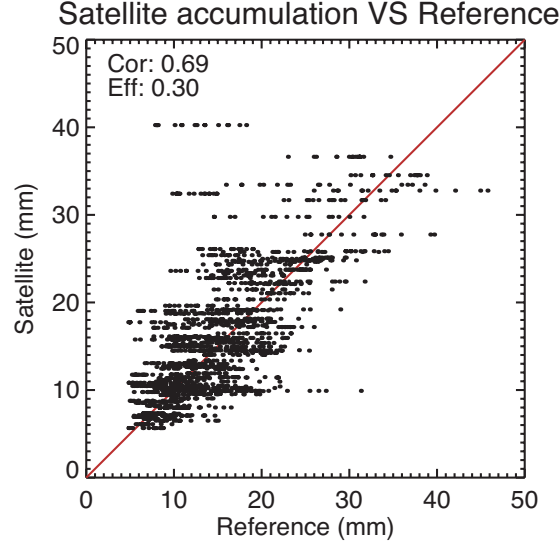
Figure 3.19: Spaceborne radar simulated observations accumulated for an entire event compared to the reference. The correlation and Nash Efficiency between the two fields are written in the plot.

Ground- and space-borne radars simulations have been also compared in terms of their probability density functions [pdf]. The pdfs used in this work represent the distribution of rain volume by rain rate (see equation 3.6; advantages of such kind of pdfs are discussed below in section 4.2.1.3 where are used extensively).

$$PDF(R_i) = \frac{\sum_{R_i - \Delta R}^{R_i + \Delta R} R}{\sum_{0}^{\infty} R} \tag{3.6}$$

Figure 3.20 shows the pdf for the ground radar simulations at several distances (5, 25, 50, 75 and 100 km), the spaceborne radar simulations, and the reference field. We can see that the spaceborne radar performs better than the ground radar below certain distance in those terms. That effect is probably related to the fact that the spaceborne radar is measuring closer to ground (reference) than the ground radar (which may be affected by the VPR). In this figure we can also see again the distance effect in the ground radar pdf, underestimating the high values and overestimating the low ones when increasing the distance.

Figure 3.20. Ground- and space-borne radar simulations pdf compared to the reference field pdf.

3.3. Global errors affecting radar rainfall estimates.

The present study shows a methodology (in the framework of comparing the rainfall estimates against a reference) to characterize the global error affecting radar-based precipitation estimates and t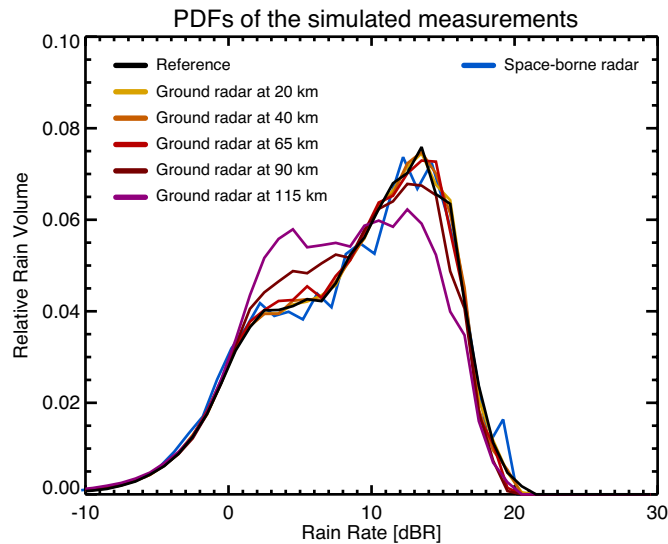o propose an appropriate probabilistic model to describe this uncertainty. In a first step, we merge radar and raingauges using all information available offline, obtaining blended rainfall fields that are assumed to represent the best available estimation of the 'true' precipitation field (reference). Then the error in radar estimates is defined as the ratio between the reference and radar estimates in logarithmic scale. The distribution, as well as autocorrelation of this error has been studied for several events using the String of Beads model (Pegram and Clothier, 2001a, 2001b), and the parameters of the model characterized.

Finally, the obtained error structure is used to generate, via a probabilistic simulation approach, ensembles (set of equiprobable scenarios), compatible with the observations, and ready to be used in probabilistic applications (for example, to drive hydrological models: see e.g. Schröter *et al.* 2010; Schröter *et al.* 2008; Germann *et al.* 2009).

3.3.1. Data used in this study

The radar data used in this study were recorded by the Spanish Meteorological Agency [AEMET] radar located in Corbera de Llobregat (close to Barcelona). The radar data are corrected for ground clutter, orographic screening and speckle before its use (with the algorithms of Berenguer *et al.* 2006; Sánchez-Diezma *et al.* 2001a). Also, radar data are multiplied by a climatological correction factor derived from a comparison with raingauges, in order to eliminate the systematic bias due to electronic miscalibration of the radar (Franco 2008). Radar reflectivity values are transformed into

rain using Marshall-Palmer Z-R relationship (Marshall and Palmer 1948). The final resolutions of the radar product data are 1 km^2 in space and 10 minutes in time. The accumulation of the rainfall rate within 10-minute intervals is based on a morphing of instantaneous observations of precipitation fields (Sánchez-Diezma 2001).

The raingauge data used come from the Hydrological Information and Alert System (SAIH) network belonging to the Catalan Water Agency (ACA). A total number of 125 raingauges have been considered, reporting data in 10 minutes intervals.

The following study is performed over a Cartesian sector of 64x64 km^2, located close to the radar and in an area well covered by the raingauge network. Figure 3.21 shows the area selected for the study, as well as the raingauge network and the location of the radar.
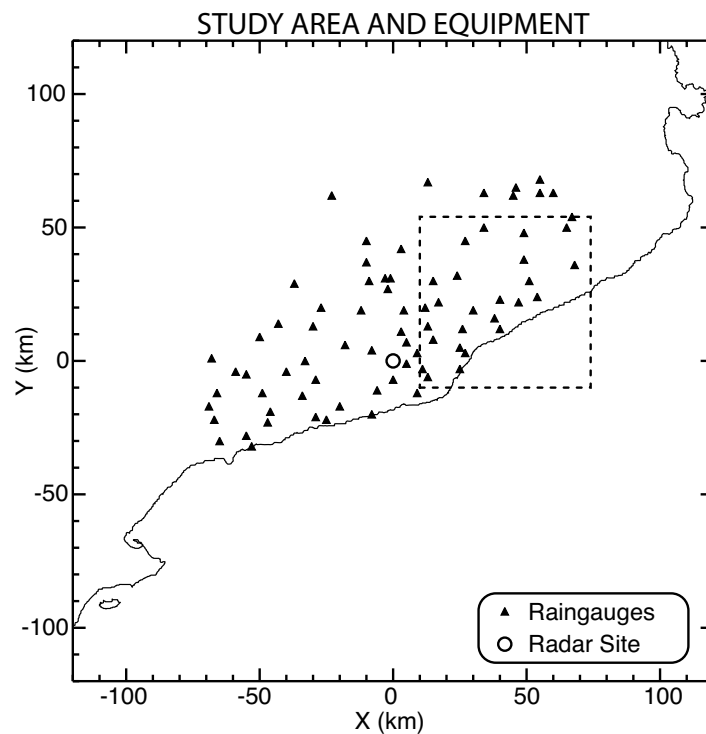
Figure 3.21: Map showing Catalunya area and the 64x64 km^2 area used for the study (dashed line). Radar location is marked with a circle and the raingauge network with triangles.

3.3.2. Methodology

In the present study, the association of an uncertainty field to the radar QPE consists in quantifying the degree of confidence in the fact that these estimates represent the unknown true precipitation field. Therefore, the error field is defined on a relative comparison between the radar QPE field available in real time, and the best QPE field that can be obtained (which we will refer as "Benchmark") using all the information available off-line, as well as expert post processing analysis.

In this study, the benchmark fields are defined as the combination of the best radar estimates (corrected as in real time) blended with raingauge data using Kriging with external drift and anisotropic correlation maps (Velasco-Forero *et al.* 2009).

This approach, despite it is subject to errors in the benchmark estimates, it allows us to define a 2D error field, and studying its structure.

Since radar errors are mainly multiplicative (Germann *et al.* 2009; Lee *et al.* 2007), the error field at time t (E(t)) is defined as the ratio between benchmark rainfall ($R_{bench}(t)$) and radar rain estimates ($R_{rad}(t)$) in logarithmic scale:

$$E(t) = 10 \cdot Log_{10} \frac{R_{bench}(t)}{R_{rad}(t)} \qquad (3.7)$$

A threshold in rain is applied in order to avoid considering pixels where no rain is recorded, and to avoid problems with the transform to the logarithm transform. For this study a pixel threshold of 1 mm/h has been used and pixels below this threshold not considered.

The histogram of the error fields is assumed to be Gaussian distributed. As example Figure 3.22 shows the error distribution for an entire event recorded on October 8th, 2002 from 00:00 UTC and lasting for more than two days.
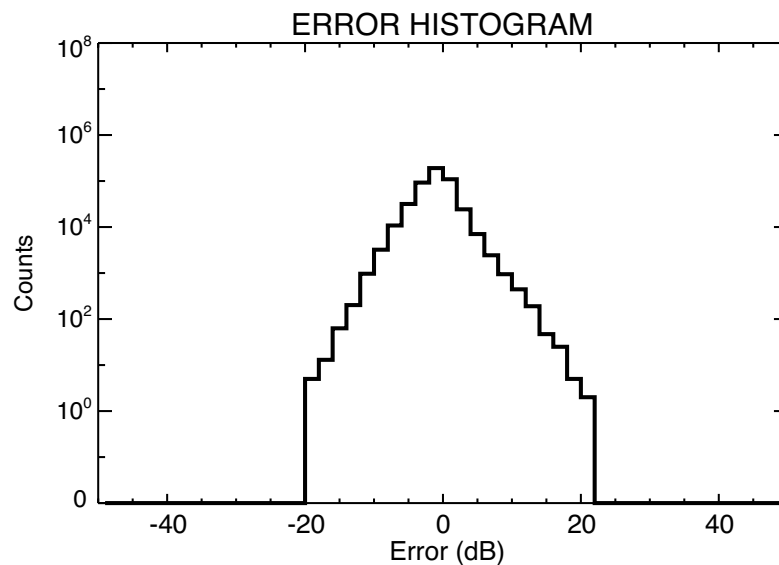
Figure 3.22: Histogram of error field values E(t) for a whole event registered starting on October 8th, 2002 at 00:00 UTC and lasting more than 70 hours.

As parameters describing the error distribution we used the mean ($\mu(t)$) and the standard deviation ($\sigma(t)$) of the error field E(t), at each time step t. We suppose that a power-law can be fitted to the radially-averaged Fourier Power Spectrum of the error fields (as in the String of Beads Model, see equation 3.5; Pegram and Clothier 2001a, 2001b). Then, spatial autocorrelation is characterized using the exponent β (slope of the best fit to the Fourier Power Spectrum). Therefore, steeper

spectra (more negative values of β) correspond to fields having a greater spatial autocorrelation (smoother fields).

Parameters $\mu(t)$, $\sigma(t)$ and $\beta(t)$ are calculated at each time step t along the entire event and then average parameters ($\overline{\mu}$, $\overline{\sigma}$ and $\overline{\beta}$) for the event are derived using only the time steps with rain over a given threshold.

Using the described methodology, the uncertainties in radar QPE for several case study events have been characterized. Error fields have been calculated for each time step and statistically analyzed to study the parameters of the probabilistic model.

Figure 3.22 shows the error field distribution for the entire event recorded on October 8th, 2002 from 00:00 UTC. The probabilistic model assumes the error distribution as Gaussian (notice that y-axis in Figure 3.22 is in logarithmic scale). Individual error distributions for each time step do not diverge much in shape from the entire event one.

Model parameters $\mu(t)$, $\sigma(t)$ and $\beta(t)$ evolution during the same event are shown in Figure 3.23. The same figure shows for reference purposes a plot of the rainfall mean (mean of the rainfall field in the area of study at each time step) as seen from radar and from benchmark. In order to calculate average parameters for the event, only time steps with average mean rainfall over a threshold (1 mm/(10 min) has been chosen as a compromise) have been considered. In this figure it can be seen that the variation of the model parameters remains relatively small during the event.
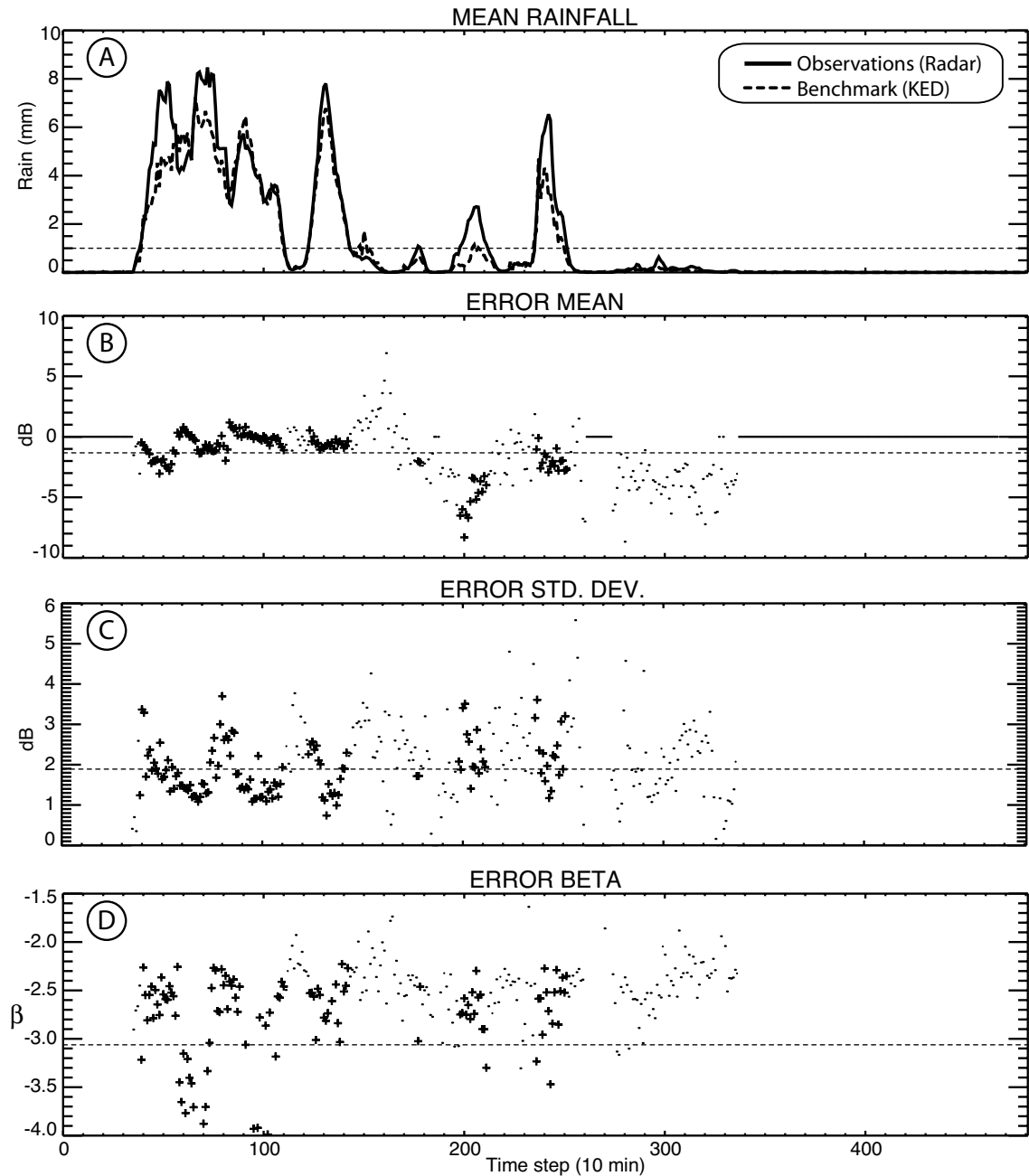
Figure 3.23: Evolution of Rainfall Mean (Panel A), μ (Panel B), σ (Panel C) and β (Panel D) for the event recorded on October 8th, 2002 from 00:00 UTC. Dashed line in Panel A represents the threshold applied to consider the parameters of a given time step in the calculus of the average parameters for the whole event. Points over this threshold are represented with crosses in panels B-C-D and points below the threshold are plot with dots. Dashed lines in panels B-C-D correspond to the mean parameter over the entire event (considering only the time steps over the specified rain threshold).

The $\mu(t)$ and $\sigma(t)$ parameters fluctuate during all event around their respective averages ($\overline{\mu}$, $\overline{\sigma}$), but $\beta(t)$ average ($\overline{\beta}$) is dominated by few time steps having a very low β, that is, highly spatially correlated, therefore smooth error fields. In order to constrain the probabilistic model parameters, the relation between the error field and the radar QPE field has been analyzed (not shown). In

particular we studied the correlation between the $\mu(t)$ parameter, which drives the mean values of the generated ensemble members, and the mean of the radar precipitation estimates at each time step. No clear relation has been extracted from this study. On the other hand, $\sigma(t)$ parameter has some correlation (inverse) with the mean of the radar precipitation estimates (explicitly not shown, but it can be seen in Figure 3.23, panels A-C). Similar results have been obtained analyzing other events.

3.3.3. Ensemble generation

The studied error structure associated to the radar precipitation estimates can be used to generate an ensemble of radar precipitation estimates (see e.g. Germann *et al.* 2009). In this work, for this purpose we isolate the benchmark QPE by rearranging equation 3.7 and we obtain equation 3.8.

$$R_{bench}(t) = R_{rad}(t) \cdot 10^{\frac{E(t)}{10}} \qquad (3.8)$$

Since the error field is unknown in real time, $E(t)$ term it is replaced in equation 3.8 by a stochastic perturbation field [$\delta_i(t)$] with the appropriate structure, giving through equation 3.9 an ensemble member [$\varepsilon_i(t)$] instead of the benchmark estimates. And because δ_i has the same statistics as E and both are assumed Gaussian, ε_i should be distributed similarly to R_{bench}.

$$\varepsilon_i(t) = R_{rad}(t) \cdot 10^{\frac{\delta_i(t)}{10}} \qquad (3.9)$$

The perturbation field $\delta_i(t)$ is generated by a simulation process. In a first step, a white noise random Gaussian fiald distributed with $\overline{\mu}$ mean and $\overline{\sigma}$ standard deviation is generated, and next the autocorrelation (using $\overline{\beta}$ parameter) is imposed using a power-law filter in the Fourier domain (see details in Pegram and Clothier 2001b). With this process we can generate as many perturbation fields $\delta_i(t)$ as needed with identical statistical properties, producing an ensemble (set of equiprobable estimates of the precipitation field) representing the uncertainty in radar QPE.

Using the average parameters obtained in the error study ($\overline{\mu}$, $\overline{\sigma}$ and $\overline{\beta}$), an ensemble of 100 members has been generated applying this methodology.
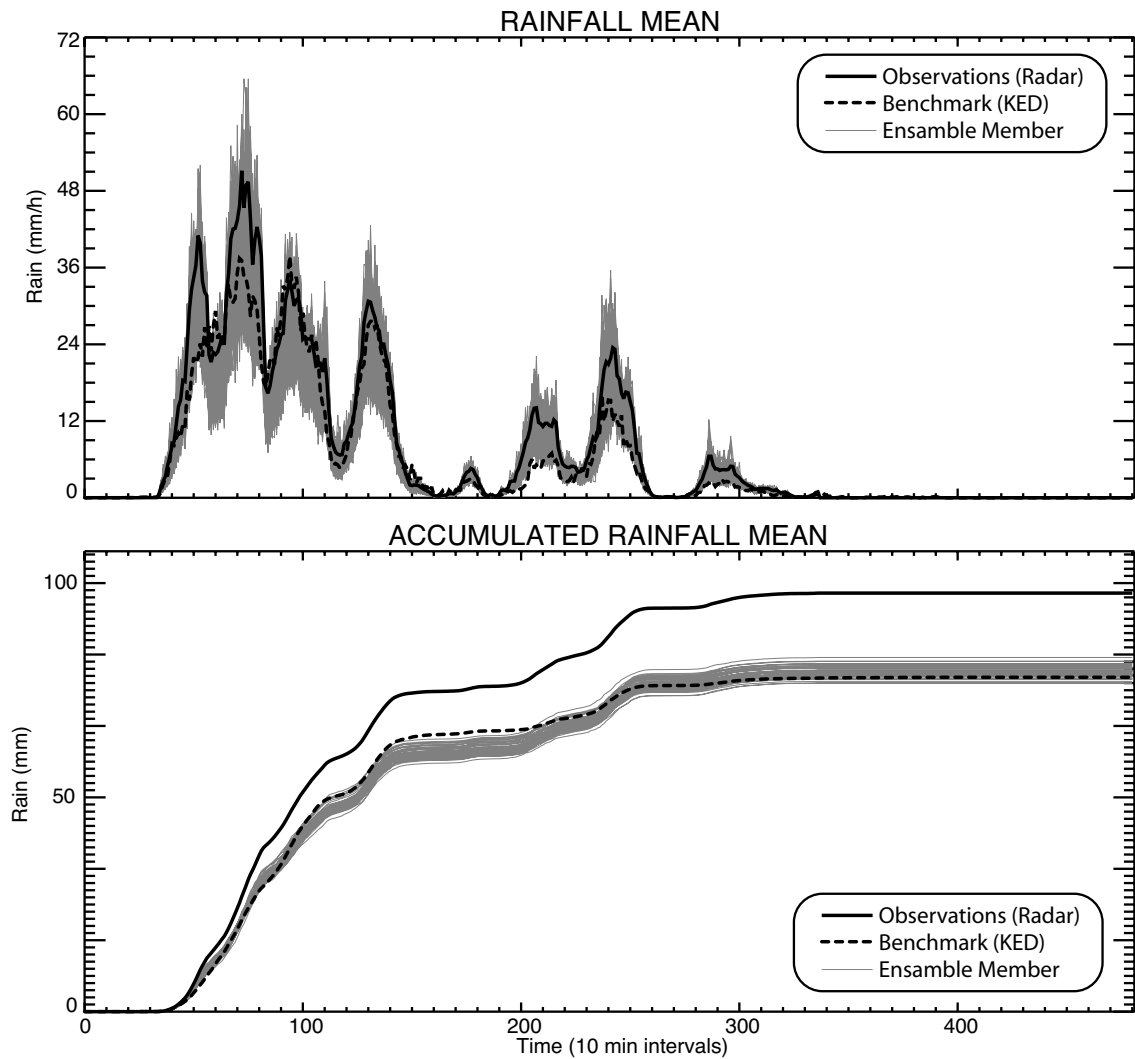
Figure 3.24: Rainfall Mean instantaneous (top) and accumulated (bottom) for the event recorded on October 8th, 2002 starting 00:00 UTC. Solid line corresponds to radar QPE, dashed line to Benchmark QPE, and each one of the 100 thin grey lines to an ensemble member.

Figure 3.24 shows the evolution along the event of the rainfall mean for the radar QPE and benchmark QPE (same as Figure 3.23, panel A) and all the ensemble members, both in instantaneous and accumulated terms. It can be seen how the uncertainty in radar QPE is translated into a spreading of the ensemble rain estimates in each time step. In the accumulated graph it can also be seen how the ensemble corrects the overestimation of radar estimates with respect to the benchmark (probably due to the climatological correction factor being too large for this event), and how all the final ensemble members accumulation values lie around the benchmark value.

Figure 3.25 shows an example of ensemble for a single time instant. It can be seen how the ensemble members are similar to the observed, the differences (noise fields) are plotted in the same figure. The spatial autocorrelation of the noise fields can be seen in the figure.

Figure 3.25: Example of ensemble generation for a single radar field. The first column (single panel) shows the real observations of the radar. The second columns shows four noise fields generated with the appropriate structure. The third column shows the four ensemble members corresponding to the noise fields of the second column (at the same instant of time as the observed field).

3.4. Summary, conclusions and future work

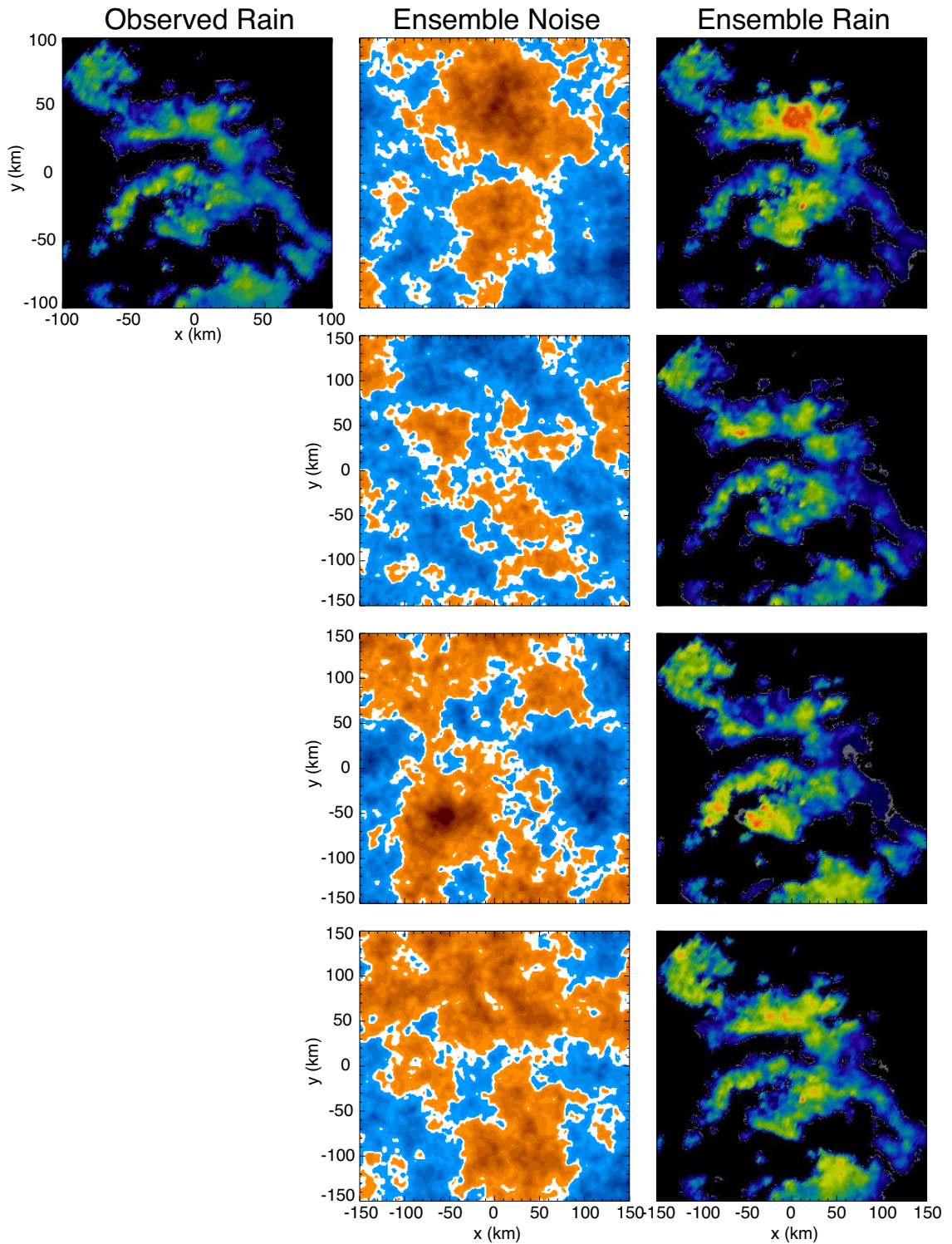The presented results show the potential of this simulation approach to study the different errors affecting radar rainfall estimates. In this first step, we characterized and quantified the errors due to range. Using this information, ensembles of radar estimates taking into account the range error could be produced by adding noise with the appropriate structure to the observations.

Comparisons of radar simulated measurements against the reference fields show the clear influence of the distance in the ground radar rainfall estimates (effects of overestimation in bright band areas and scatter and underestimation in convective areas).

The comparison of radar observation simulations at different distances against the simulation of a network of raingauges, shows the decrease of efficiency with range, but at the same time gives a "threshold" of the number of gauges necessary to obtain a reliable estimation of the limit of agreement between these two instruments. This can be useful when comparing real observations of these two instruments.

The spaceborne radar simulations show a significant scatter due to the large pixel size of this instrument, but the estimates were not as far as expected from the reference fields, and overall they exhibited little bias.

A methodology to characterize the total uncertainty in the radar QPE has been presented. It is based on a relative comparison of radar QPE against a benchmark, followed by probabilistic model that condenses the uncertainty. The parameters of this model for several events have been studied.

The error structure obtained has been used in the generation of ensembles through a simulation process. The ensemble corrects the bias between radar QPE and Benchmark QPE, and represents the uncertainty inherent in the radar estimates through the spread of its members. This presented approach has already been used in Schröter *et al.* (2010); Schröter *et al.* (2008) to estimate how the uncertainty in precipitation estimates propagates through a distributed hydrological model. The same piece of work studies the impact of precipitation input uncertainty in the estimation of model parameters during inverse parameter estimation procedures.

Future work should include rain type classification in the study of the distance error. For the spaceborne radar simulations the vertical resolution of the three-dimensional precipitation field used as reference might be increased due to the vertical resolution of this instrument. Also attenuation should be considered in future work. This might affect significantly the spaceborne radar estimates due to the low wavelength used in this instrument.

The statistical model described to characterize the global error does not fully describe all the uncertainty structure, in particular the temporal correlation is not considered. So, future work will focus on the modelling of the space-time correlation of the errors. Stratification of the parameters

depending on event characteristics will be also studied in order to extrapolate the obtained results to areas not covered by raingauges, but characterized by the same rain type.

The described methodology to generate ensembles produces rainfall fields with the increased variance respect the original radar estimates, which maybe a problem for some applications. To overcome this problem Pegram *et al.* (2010) propose a novel methodology consistent in separating the observations into signal and noise before adding the "noise" term to generate the ensemble member. The method used a given frequency in the Fourier Power Spectrum of the data to chop between noise and signal, and the removal of the noise is done cutting the low frequencies and removing the variance of all components, fact that allows, once the noise is added to generate the simulated fields, recover the original variance.

CHAPTER 4

The structure of errors in spaceborne radar measurements

4.1. Introduction

Quantitative Precipitation Estimates [QPE] are need in algorithms and methods for data assimilation in Numerical Weather Prediction [NWP] Models and in hydrologic applications. The error characteristics of the estimates obtained will be an important input for non-deterministic (i.e. probabilistic) applications.

However, very few places in the world are well covered by ground measurement instruments (raingauges, weather radars, disdrometers, …) and therefore the available resolution (both spatial and temporal) is not enough for the needs.

In order to obtain precipitation estimates globally in the world, the last step has been to include precipitation sensors in satellites. Precipitation estimation from space-based platforms is a challenge due to the limitations in weight, size and power consumption in the instruments, plus the distance of observation and orbit of the satellite that influence on the resolution of the observations (spatial and temporal, resp.). All these limitations make the precipitation estimates from space to be affected by a large uncertainty.

This chapter proposes a framework for validation of spaceborne radar estimates: methods to estimate and characterize this uncertainty and to set quantitative and reliable uncertainty thresholds through the comparison of space-born precipitation estimates against ground-based estimations. The comparisons have been done before and after classification of precipitation in rainfall types for a better description of the discrepancies. The classification will potentially allow a better evaluation the satellite algorithms under different conditions (physical validation), and also will allow for "extrapolation" of the uncertainties to regions not covered by validation data sets but characterized by the same rain type.

For this study, the Precipitation Radar [PR] onboard of the Tropical Rainfall Measuring Mission [TRMM] satellite (known as TRMM-PR) has been used as source of precipitation estimates from space. The comparison against ground data has been performed over a single radar site (Melbourne, Florida, USA) belonging to the National Weather Service; and over the Continental United States [CONUS] Radar composite.

Many comparisons of TRMM data against other instruments have been performed before: Durden *et al.* (2003) compared TRMM-PR against airbone-radar with similar characteristics; Bowman *et al.* (2003); Serra and McPhaden (2003) compared TRMM against raingauges located in buoys in the oceans; Anagnostou *et al.* (2001) used TRMM-PR to inter-calibrate a network of radars taking advantage of the constant parameters of TRMM-PR, considering this instrument the reference against which to compare the ground radars.

Also many field campaigns have been done to obtain data to compare against TRMM estimates (like TEFLUN-A and TEFLUN-B). Ciach *et al.* (1997); Gebremichael and Krajewski (2004); Habib and Krajewski (2002) did analysis of the uncertainty in the ground estimates towards a better comparison against TRMM.

Comparisons of rainfall over daily, weekly or even monthly time scales (integral properties of rainfall) suffer from temporal sampling errors of the satellite (e.g., TRMM satellite, or the future Global Precipitation Measurement [GPM] mission swarm of satellites, Hou *et al.* 2008) where the revisit time is on the order of hours or days (see Bell *et al.* 1990; Gebremichael and Krajewski 2005 for an evaluation of the impact of temporal sampling on the rainfall estimations). These comparisons are useful for assessing biases between both instruments (Fisher 2004), but for a better description of the structure of the errors, instantaneous rainfall products are used in this work.

Scatter plots of direct comparisons of space-based rain rates with ground-based estimates (pixel by pixel) are simple to calculate but noisy because of sample volume discrepancies, timing and navigation mismatches, and uncertainties in the observed-radar reflectivity rain-rate Z-R relationships in both instruments. For this reason, an alternative approach (Amitai *et al.* 2005; Amitai *et al.* 2003; Liao *et al.* 2001) of comparing space-based radar probability density functions [pdf] with pdfs derived from co-located ground-based observations is attractive for evaluating uncertainties in satellite-based precipitation products, such as those from TRMM-PR. At the same time, the distribution of rain rate is of great interest in many fields (e.g. hydrological applications such as flood forecasting, erosion prediction and urban hydrological studies depend on an accurate representation of the rainfall that does not infiltrate the soil). In particular, in arid and semi-arid climate zones, floods, runoff, and erosion strongly depend on the distribution of the rain rate rather than on the antecedent rainfall amount since the soil does not need to be saturated for triggering

such events. Systematic shifts in rain rate pdfs will have a significant impact on surface runoff production. Despite of all this, efforts to evaluate quantitative instantaneous rain rate estimates, as opposed to rainfall-accumulated amounts are rare.

4.1.1. TRMM satellite

TRMM satellite (Simpson *et al.* 1988) was launched on November 27th, 1997 as a joint mission between JAXA (Japanese Aerospace Exploration Agency; formerly NASDA) and the United States [US] National Aeronautics and Space Administration [NASA]. It was the first (and until nowadays the only) carrying an active radar onboard (built by the Communication Research Laboratory [CRL] in Japan). Due to the limitations in weight, power and size, and the need for narrow beams in order to get an acceptable resolution at ground level, TRMM-PR operates at K_u band. This makes its measurement seriously affected by attenuation due to the scatter of the hydrometeors.

TRMM is set in an inclination angle 35° and period 90 min and covers between 40°S and 40°N. The average revisit time is around 9 hours, however, since is a Low Earth Orbiting [LEO] satellite flying at 350/402 km, the revisit time is highly irregular and highly dependent on the latitude of study (Bell *et al.* 1990).

TRMM was initially set at 350 km altitude, but to increase the life of the mission was moved to 402 km in August 2001 (the loss of fuel due to the boost will be compensated by the less consumption in the new orbit). The change of the altitude of the satellite had an impact on the TRMM-PR resolution (see Table 4.1 for characteristics of TRMM-PR before and after the boost, full description can be found in Japan-Aerospace-Exploration-Agency 2006). Several authors such as DeMoss and Bowman (2007); Shin and Chiu (2008) studied the impact of the boost in the TRMM rainfall products, this issue will not be discussed in this thesis.

Table 4.1: Specifications of the TRMM-PR

	Pre-boost	After boost
Height	350 km	402 km
Velocity of nadir at ground	7 km/s	-
Power transmitted	500 W	-
PRF	2776 Hz	-
Frequency	13.8 Ghrz (K_u: 2.2 cm)	-
Beam width	0.71°	-
Pulse duration	1.6 μs	-
Number of beams	49	-
Cross track scan angle	±17°	-
Number of gates	Between 122 and 139	-
Horizontal resolution	4.3 km	5.1 km
Vertical resolution	250 m	-
Swath	220 km	250 km

The current remaining fuel in TRMM could maintain the satellite operative until 2012-2014 depending on solar activity and other factors. GPM mission (currently launch date set on 2013) will continue collecting precipitation data with a dual frequency (K_u and K_a band) precipitation radar and covering between 70ºS and 70ºN.

4.1.2. TRMM algorithms, standard products and versions

Precipitation data from TRMM-PR is structured in levels and in standard products (processed by the Precipitation Processing System [PPS] at NASA; formerly TSDIS). Figure 4.1 shows a diagram of the standard TRMM-PR products used or cited in this thesis and their interaction.
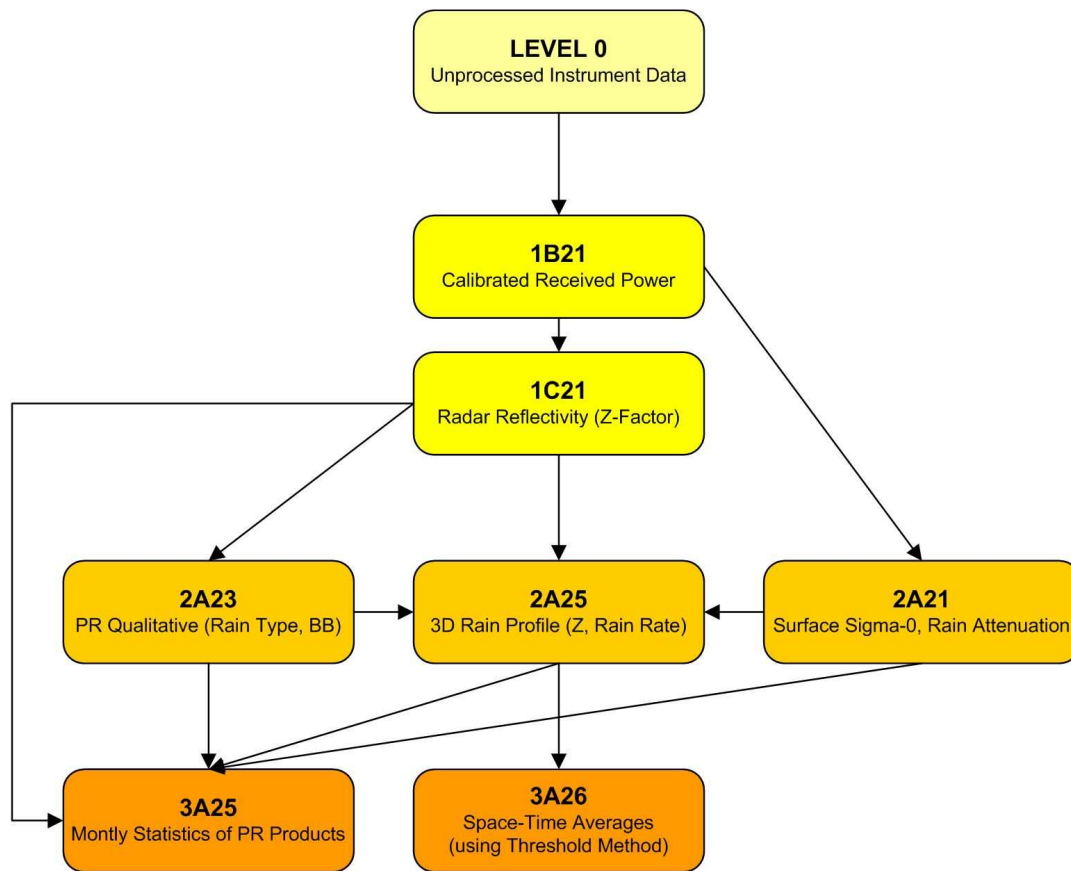
Figure 4.1: Some of the TRMM-PR standard products and its connections. Each Level of products is in different colour.

Levels 0, 1, and 2 processed products are orbital, that is, the data are stored in its original geometry (beams from the satellite and in Instant Field Of View [IFOV], the "footprint" of each beam in the surface). Level 3 products are gridded products.

TRMM-PR Level 0 products are composed of the data as recorded by the satellite instrument. Those products are processed to obtain Level 1 products such as 1B21 and 1C21. 1C21 product gives the effective reflectivity obtained applying the radar equation to the received power, without any correction for attenuation.

In Level 2 we can find the products derived from Level 1 ones. The used in this study are 2A23, 2A21 and 2A25:

- 2A23: Classification of rainfall types: convective, stratiform and "other". The product also indicates other variables as the presence of Bright Band [BB], BB height, and echotop. See Awaka *et al.* (1997) for algorithm description and Awaka *et al.* (1998) for a performance evaluation.

- 2A21: Surface σ_0, that is, the returned power (in dB) by the Earth surface. This product also classifies each IFOV in 5 groups: a) Ocean and rain, b) Ocean and no rain, c) Land and rain, d) Land and no rain, e) Others. In case of rain, the attenuation is calculated through the surface reference technique (Meneghini *et al.* 2004; Meneghini *et al.* 2000). When it is not raining, the statistics database is updated.

- 2A25: Three-dimensional reflectivity profile corrected for attenuation and surface rain rate estimates at satellite beam resolution (IFOV). This product gives the rainfall estimates and its vertical structure. This product uses the algorithm described in Iguchi *et al.* (2000) to obtain the corrected reflectivity factor. Non Uniform Beam Filling [NUBF] problem is treated in the algorithm (Kozu and Iguchi 1999). Also provides an estimation of the rainfall at ground (Near Surface rain rate variable) obtained through extrapolations with Vertical Profiles of Reflectivity [VPR] (Japan-Aerospace-Exploration-Agency 2005).

Level 3 products are composed of temporal accumulations of Level 2. 3A25 represents the monthly rain accumulation over 0.5°x0.5° and 5°x5° from the 2A25. In this level we can also find products like the 3B42 that are based on multi-satellite data involving other instruments rather than only the TRMM-PR.

TRMM mission is also composed by several Ground Validation [GV] sites: well equipped places providing data to compare against TRMM satellite. A research program was established prior to satellite launch to ensure evaluation of TRMM's precipitation retrievals (Wolff *et al.* 2005) and the GV products have been widely tested (Ciach *et al.* 1997; Gebremichael and Krajewski 2004; Habib and Krajewski 2002). Data from the GV sites is organized in levels and products as well as satellite data. The products cited in this thesis are the 1B51 (raw data from ground radar in polar coordinates); the 2A53 (instantaneous 2D rainfall estimation from ground radar in Cartesian coordinates with 2 km horizontal resolution; raingauges are used to adjust the ground radar estimates); 2A54 (Classification in rainfall types from ground radar); and the 2A55 (3D reflectivity field from ground radar).

From each TRMM product there are several versions. Between versions there are some changes in the algorithms used to obtain the products. When TRMM satellite was launched, the operative versions of the products was version 4 [V4] for the TRMM-PR products and Version 3 [V3] for the

GV products. Currently all data have been reprocessed to the new versions: Version 6 [V6] for TRMM-PR and Version 5 [V5] for GV. This work uses several versions of the products and also shows a comparison between V5 and V6 of TRMM-PR products.

A complete description of the TRMM-PR products as well as the changes between the versions can be obtained in Japan-Aerospace-Exploration-Agency (2005).

All data can be obtained through PPS website in its last version. For older versions PPS should be contact directly.

4.2. Case Studies

With the aim of characterizing the uncertainty in the precipitation estimates observed by TRMM-PR several case studies are presented. The inter-comparisons between satellite precipitation estimates and ground estimates are done under different circumstances to better evaluate the reasons of the discrepancies. Comparisons between different versions of the same TRMM-PR product (2A25 Version 5 and Version 6) are performed to show also the degree of confidence in satellite estimates.

4.2.1. Melbourne, Florida

Comparisons of TRMM-PR against the National Weather Service Radar WSR-88D radar located at the GV site of Melbourne, Florida (US), will be shown in this first inter-comparison.

4.2.1.1   Search of overpasses

The average revisit time of TRMM-PR over the GV site of Melbourne, Florida, in an area of 100 km around the radar site is approximately 12 h. If we want also a rainy overpass, we found an average frequency of twice a month. To search for rainy overpasses we used Orbit Viewer software together with the Mission Index of each year provided by PPS. This product contains the daily rain accumulation in a grid of 0.2°x0.2° based on 3A25 product and allows us to find the rainy days. At the same time it plots the flight track and orbit number, so we can identify the rainy overpasses.

Once the rainy overpasses have been identified, the TRMM-PR time of the closest IFOV in the nadir track (see Figure 4.2) to the GV radar is obtained from 2A25 product. Then from GV data, the closest volume scan in 2A53 products is selected for the comparisons. Since the GV radar provides a complete volume scan every 6 minutes, the maximum difference in time between both products is of 3 minutes.

Figure 4.3 shows the 24 rainy overpasses over the WSR-88D radar at Melbourne GV site found during 1998, the first complete year of TRMM. TRMM-PR 2A25 and GV 2A53 rain rate products are shown.
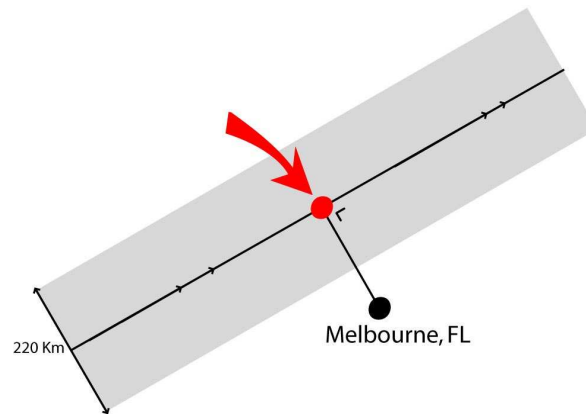
Figure 4.2: Schema of the closest TRMM-PR time to the GV radar site. Nadir track of the satellite is represented with a black line inside the satellite swath (220 km before August 2001, grey area in the figure). The IFOV in the nadir track closest to the Melbourne radar is depicted in red.

Figure 4.3: The 24 rainy overpasses over WSR-88D radar at Melbourne, Florida, GV site found during 1998. TRMM-PR 2A25 rain rate product shown in comparison to the GV 2A53 rain rate prod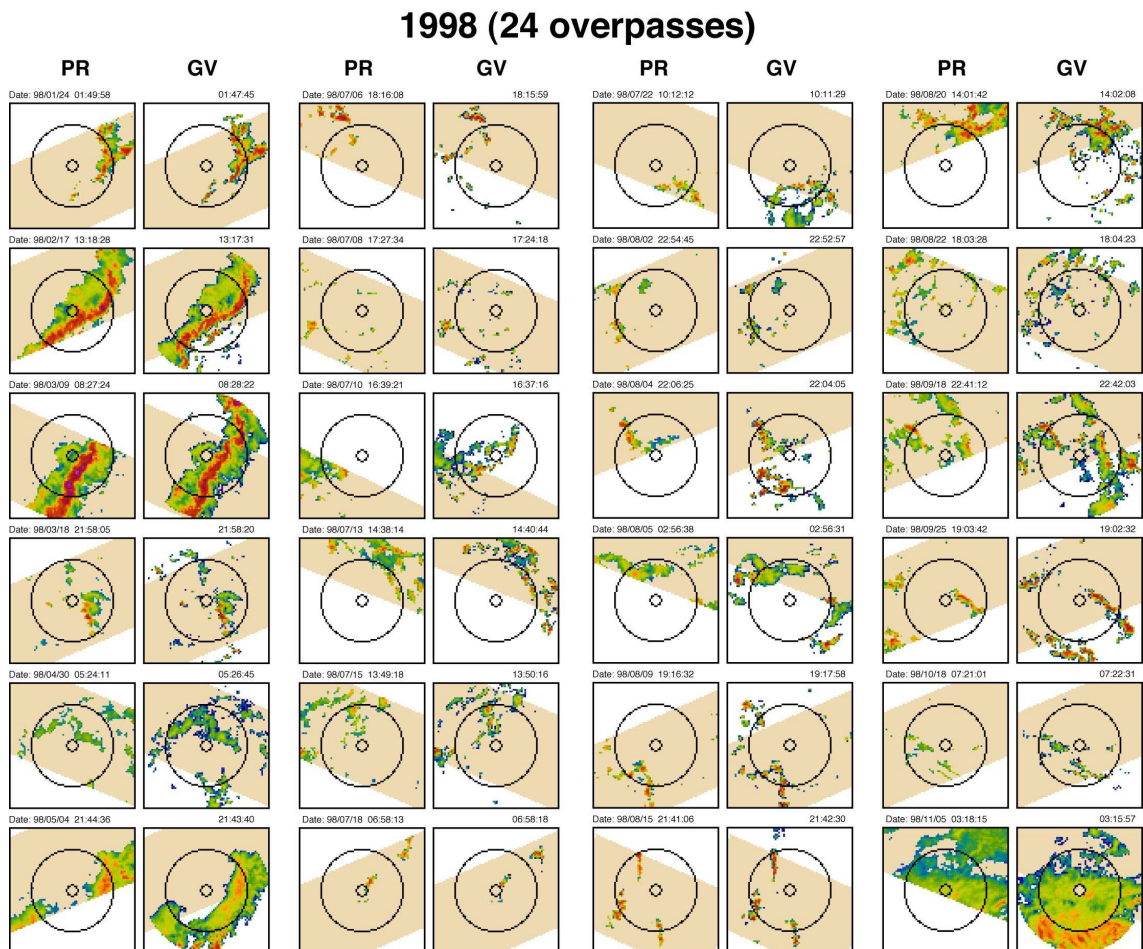uct. Date and time for both products is written in the images. Circles represent 15 and 100 km to the radar site. Brown area represents the TRMM-PR swath (220 km before August 2001).

For the first part of this study, we used 105 rainy overpasses at the Melbourne (Florida) GV site found between 1998 and 2002 distributed as Table 4.2 shows.

Table 4.2: Rainy overpasses of TRMM-PR at Melbourne, Florida GV site.

1998	24
1999	19
2000	27
2001	22
2002	13

4.2.1.2   Data matching and regridding

The comparison area used in this study is the area covered by the TRMM-PR and within a range interval of 15 to 100 km from the Melbourne, Florida, National Weather Service Radar (WSR-88D) (see Figure 4.4). TRMM-PR measures quite uniformly in all satellite swath, but ground radar precipitation estimates quality depends strongly on the distance to the ground radar, for this reason, a limit of 100 km has been set to avoid areas where the radar measures too high and with a wide beam.
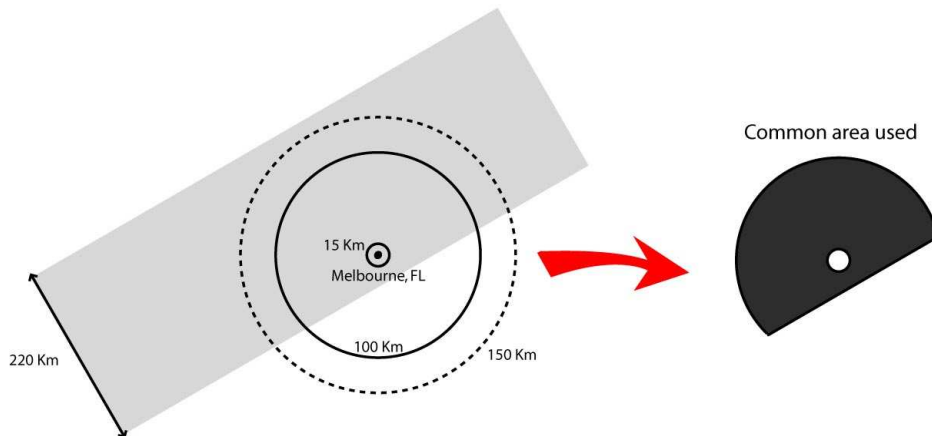
Figure 4.4: Schema of the common area used. GV radar data are taken within 15 and 100 km from the radar. TRMM-PR data are taken from inside swath.

The data of both TRMM-PR and GV radar estimates has to be transformed to a common grid for their inter-comparison. We used in this study a common grid of 4x4 km² and a field of 300x300 km² centred in the radar site (see Figure 4.5). 2A53 GV product has been averaged to the 4x4 km² common resolution.
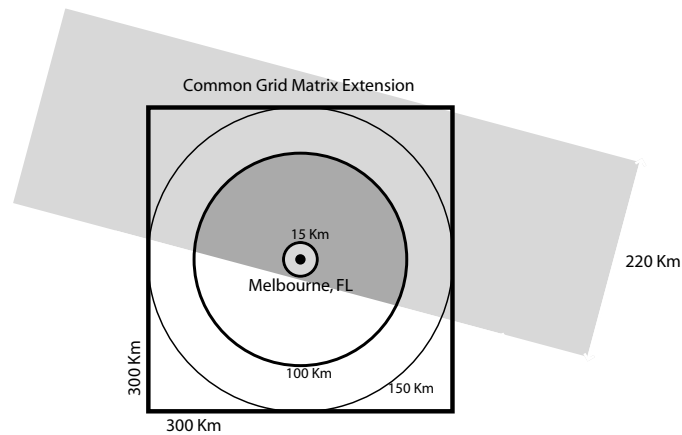
Figure 4.5: Schema of the grid obtained after the interpolation. The area inside the grid finally used for the inter-comparison is depicted in dark grey.

The gridding procedure used to transform from TRMM-PR irregular sampling into grid values is based on Delaunay triangulations (Delaunay 1934) and it is similar to the procedure described in Liao *et al.* (2001) (see a schema in Figure 4.6). The Delaunay triangulation is unique for a set of points and maximizes the minimum angle of all triangles in the resulting triangulation. This step is done over the TRMM-PR IFOV points. Then we interpolate the parameter value of each IFOV from the original product into the grid points using the triangulation. The points of the grid that are inside a triangle, get the value of the linear interpolation of the vertex coordinates taking into account the distance; the points of the grid that are not inside any triangle of the triangulation are flagged. The interpolation is done in Z power ($mm^6 \cdot m^{-3}$) values for the reflectivity fields (like the 2A25 3D reflectivity profile) and in mm/h for rain rate fields (like 2A25 near surface rain rate). In the 3D dimensional field of 2A25 reflectivity, the interpolation is done for constant altitudes at each 250 m. TRMM-PR pixels are treated as point values in the triangulation and interpolation processes and represent an area.
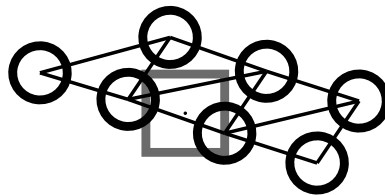

Figure 4.6: Schema of the regridding interpolation with the original TRMM-PR IFOVs, the Delaunay triangulation and a final grid pixel.

Rain rate estimates are taken from the NASA TRMM-PR and GV standard products (2A25 and 2A53, respectively).

4.2.1.3   Results

The first results that we will show are the direct comparison of TRMM-PR 2A25 precipitation estimates against the GV 2A53 estimates. The variable used in 2A25 is the "Near Surface Rain Rate", the lowest measurement of each TRMM-PR IFOV not contaminated by ground clutter.

Figure 4.7 shows the comparison over Melbourne, Florida, of three overpasses. First overpass shown is a squall line (convective case), the second is more stratiform and the third is a mix of precipitation types. We can observe that correlation between both fields is high (~0.9 for first and third overpasses and 0.7 for the second) however, differences in the retrieved rain rates of both instruments is high. In the same figure there are plotted the accumulation of each instrument and the bias between both instruments (calculated as the ratio between the sum of the rain measured by TRMM-PR in the common area and the rain measured by GV in the same area). Positive bias means an overestimation of TRMM-PR while negative bias means an underestimation of this instrument. We can see how in the convective case, TRMM-PR overestimates the GV precipitation by a 60% (Bias of 1.60) meanwhile the stratiform case it underestimates the GV precipitation by a 12% (Bias of 0.88). The third case (mix of precipitation types) seems to perform between the previous with an overestimation by TRMM-PR of 44%.
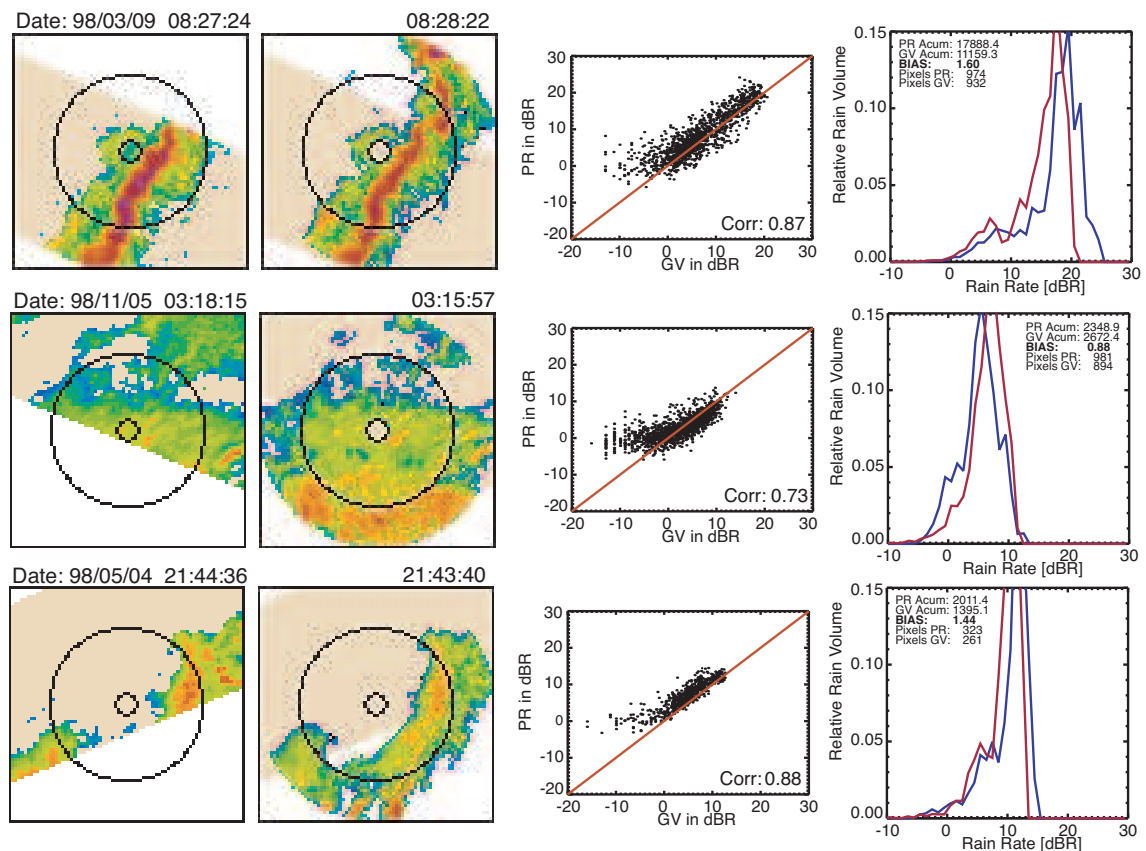

Figure 4.7: Comparison of TRMM-PR 2A25 V5 precipitation estimates against GV 2A53 V5 estimates in three overpasses at Melbourne, Florida. The first column are the TRMM-PR rainfall estimates, the second column the GV estimates both regridded to a common

grid. Circles represent 15 and 100 km distances from ground radar. Brown area is the TRMM-PR swath. Third column shows a scatter-plot of pixel-by-pixel comparison in the common area, and the correlation of both fields. Last column shows the pdf of both rainfall fields and some statistics (TRMM-PR in blue, GV in red). Pdfs are plotted in logarithmic scale: dBR=10 log(R). Date and time of each overpass is printed on top of the images.

In this study we also used Probability Density Functions [pdfs] as approach to compare satellite-based precipitation products against ground based products. The pdfs used for this study represent the distribution of rain volume by rain rate, as they are constructed according to the relative contribution made by each rain intensity bin to the total rain volume (see equation 4.1).

$$PDF(R_i) = \frac{\sum_{R_i - \Delta R}^{R_i + \Delta R} R}{\sum_{0}^{\infty} R} \qquad (4.1)$$

Weak intensities, which are detected by only one instrument, might be associated with quite a large fraction of the total rain area but with a very small fraction of the total rain amount. Therefore, the shape of this pdf is less affected by weak intensities, as they do not contribute much to the rain volume and therefore less sensitive to the instrument rain detection limits than the pdfs of occurrence. This is a good advantage for comparison of pdfs based on estimates derived from different instruments (e.g., raingauge, ground- and space-based radar), each characterized by a different detection limit.

In the pdfs shown in Figure 4.7 we can see (in the first and third overpasses) a shift towards the left of TRMM-PR curve with respect to the GV curve, denoting the overestimation of this instrument, however, we can see that the distribution of the rain rates is similar for both instruments in these cases. This overestimation of TRMM-PR is probably due an overcorrection of the attenuation (the field presents high horizontal gradients that make it difficult to estimate the NUBF parameter used in the attenuation correction algorithm 2A25: Zhang *et al.* 2004). In the second overpass a shift towards lower values of rain rate can be seen in the TRMM-PR curve indicating that this instrument retrieves lower values than the GV estimates.

In the pdf curves we can also observe the characteristics of the precipitation: the first case is clear convective having most of the volume over 10 mm/h while the second is stratiform having the rain volume below this value. The third case the pdfs performs centred around 10 mm/h.

A minimum number of pixels are necessary in order to obtain stable and not noisy pdfs, therefore it is difficult to analyze case by case over reduced areas. This leads us to use several overpasses combined.

Figure 4.8 shows the comparison of the TRMM-PR and GV pdfs based on all rainy overpasses found during 1998-2002 period in central Florida (105 rainy overpasses). From the bias, we can see that TRMM-PR estimates 4% less rain than the GV radar.
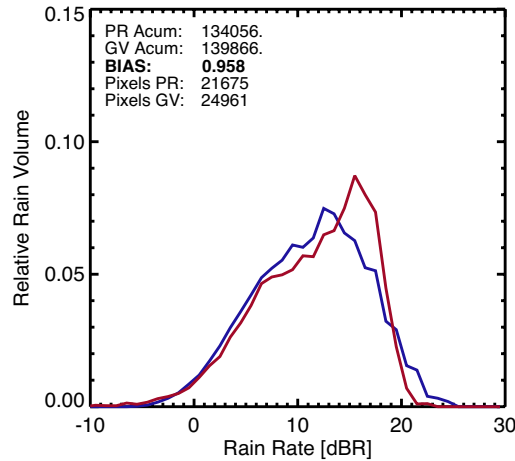
1998-2002 (105 overpasses)

Figure 4.8: Distribution of rain volume as function of rain rate (in logarithmic scale: dBR=10·log(R)) for the Melbourne, Florida, WSR-88D (GV, 2A53 V5) and TRMM-PR (2A25 V5) datasets based on 105 overpasses during 1998-2002 and co-located GV data within 15 and 100 km of ground radar site. TRMM-PR plotted in blue, GV in red. The number of rainy pixels, their rain accumulation, and the PR/GV rain volume bias are indicated in the legend.

If we analize the areas where one instrument detected rain and the other did not, we obtain that 7.5% of the rain amount measured by the GV is measured in regions where the TRMM-PR did not register any rain. In those pixels the average rain rate is 1.8 mm/h (in all GV rainy pixels the average is 6.1 mm/h) implying that probably the TRMM-PR does not detect rain in this areas due to its low sensitivity (17 dBZ). On the other hand, 3% of the TRMM-PR rain was detected in pixels in which the GV radar registered no rain, those pixels have also weak rain rates. Therefore, we assume that of the 7.5% of the events where GV detects rain and the TRMM-PR does not, 3% is associated with mismatches due to wind sorting and navigation and timing errors, while the remaining 4.5% is the result of the low detection threshold of the TRMM-PR. If we consider the GV estimates as the reference (or "truth") the results can be interpreted as the TRMM-PR underestimates the rain by 4%, but also does not detect 4.5% of the rain. On the other hand, when the TRMM-PR detects rain, it compares quite well with the ground radar estimates.

Amitai *et al.* (2005) using data from 24 TRMM-PR overpasses and collocated GV radar rain rate estimates in central Florida during 1998, compared a TRMM-PR V5 pdf with two GV pdfs based on the two different gauge adjustment schemes (V4: Z-R with fixed parameters; and V5: WPMM Rosenfeld *et al.* 1994). They found that the two GV pdf curves are almost identical compared to the TRMM-PR pdf, increasing our confidence on GV pdfs.
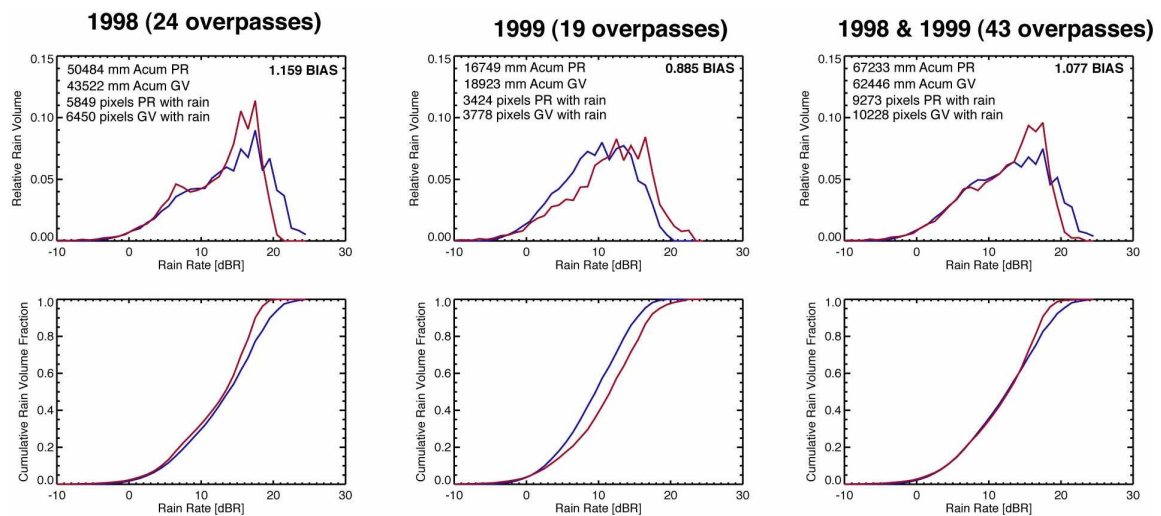
Figure 4.9: Distribution of rain volume as function of rain rate (in logarithmic scale: dBR=10·log(R)) for Melbourne, Florida, WSR-88D (GV, 2A53 V5) and TRMM-PR (2A25 V5) datasets. First column shows the 24 overpasses found in 1998, the second shows the 19 overpasses found in 1999, and the third shows both years together. TRMM-PR plotted in blue, GV in red. The number of rainy pixels, their rain accumulation, and the PR/GV rain volume bias are indicated in the legend. Second row show the corresponding Cumulative distribution Functions [cdfs].

In the Figure 4.9 we can see the pdfs for the 24 overpasses found in 1998, the 19 overpasses found in 1999 and the two years together. We can observe that the bias of the two years together is 7% of TRMM-PR overestimation of GV, but looking year by year, in 1998 there is a 16% of TRMM-PR over estimation and in 1999 there is a 12% of TRMM-PR underestimation. Looking to the pdfs shapes, we can observe differences between both years that are somehow compensated in the global pdf (in 1998 TRMM-PR curve is shifted to the high intensities and has lower peak; and in 1999 TRMM-PR curve is shifted to lower values having similar peak to the GV curve). Looking to the pdf of 1998 we can recognize the shape of the pdf for the first overpass of Figure 4.7. This is because this overpass had a high rain accumulation and it is extremely dominant even at year scale.

The changes between overpasses shown in Figure 4.7, the differences between years of Figure 4.9 and the shift in the GV pdf curve of Figure 4.8 toward high rain rates at low and medium rain intensities and vice versa for higher rain intensities suggests further analysis based on rain type classification to characterize in which situations occur these discrepancies.

4.2.1.4 Classification

After the discrepancies found in the previous section, we will use now statistical properties of precipitation (pdfs) combined with physical properties (rain type classification) to estimate the uncertainty associated to each rain type.. The aim of this classification is to allow extrapolation of

TRMM-PR estimates uncertainty to places not covered by ground equipment but characterized by same rain type. Therefore, the classification will be done using TRMM-PR variables.

In order to obtain stable pdfs (well defined) for each rain type after classification we need to analyze several overpasses together to have enough pixels in each class.

First classification schema used is the already given by TRMM-PR standard product 2A23 in convective and stratiform (Awaka *et al.* 1997). Figure 4.10 shows the pdf for both rain types of this classification. We can observe that pdfs for stratiform class are really similar despite a small shift of GV curve towards high rain rates. In the convective class we see higher differences between TRMM-PR and GV pdfs, having the GV one a higher peak. Looking to the biases (6% underestimation of TRMM-PR for stratiform class and 1% overestimation for TRMM-PR in convective class) we can observe that the global underestimation of TRMM-PR of 4% obtained in Figure 4.8 is mainly produced by the stratiform rainfall and slightly compensated by the TRMM-PR overestimation in the convective rainfall.

105 Overpasses

Figure 4.10: Distribution of rain volume as function of rain rate (in logarithmic scale: dBR=10·log(R)) for the Melbourne, Florida, WSR-88D (GV, 2A53 V5) and TRMM-PR (2A25 V5) datasets based on 105 overpasses during 1998-2002. Left panel shows the pdf for the pixels classified as stratiform according to 2A23 TRMM-PR standard product. Right panel shows the pixels classified as convective. TRMM-PR plotted in blue, GV in red. The number of rainy pixels, their rain accumulation, and the PR/GV rain volume bias for each rain type are indicated in the legend.

For a better description of the uncertainties in the different rainfall types, we used the classification scheme of Amitai (1999). This classification scheme is based on physical principles and it uses the following parameters for classification: Echo top height at 20 and 32 dBZ, horizontal reflectivity gradients above the freezing level, and the strength of the Bright Band signature. The reflectivity value of 20 dBZ was chosen as an approximation to the minimum detectable signal of PR. Reflectivities less than 32 dBZ were assumed to be little affected by attenuation.

Bright Band signature (associated with stratiform precipitation) is characterized using the "Bright Band Fraction" concept (see Rosenfeld *et al.* 1995). The 0º isotherm at Melbourne, Florida, is usually between 4 and 5 km, then the Bright Band Fraction [BBF] is defined as the ratio of the pixels having their maxima between these two heights in a 3x3 pixel² window around the pixel of interest. To consider that Bright Band is detected using the Bright Band Fraction method, a threshold in BBF should be set. Figure 4.11 shows the pdfs for 1998 and 1999 overpasses (42 overpasses) of TRMM-PR 2A25 and GV 2A53 rainfall estimates classified in two rain types using BBF at different thresholds. We selected 60% as the threshold in BBF to detect BB due to the stability of the pdfs around this value and as a compromise of been too restrictive and detecting BB in too many pixels.
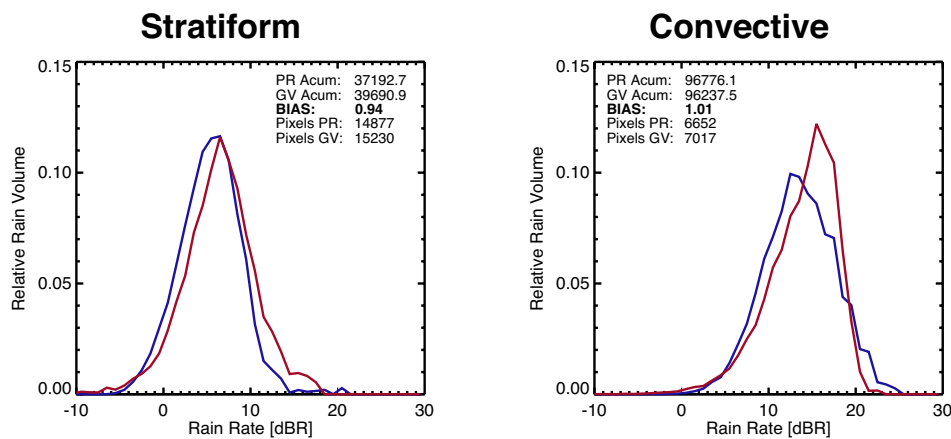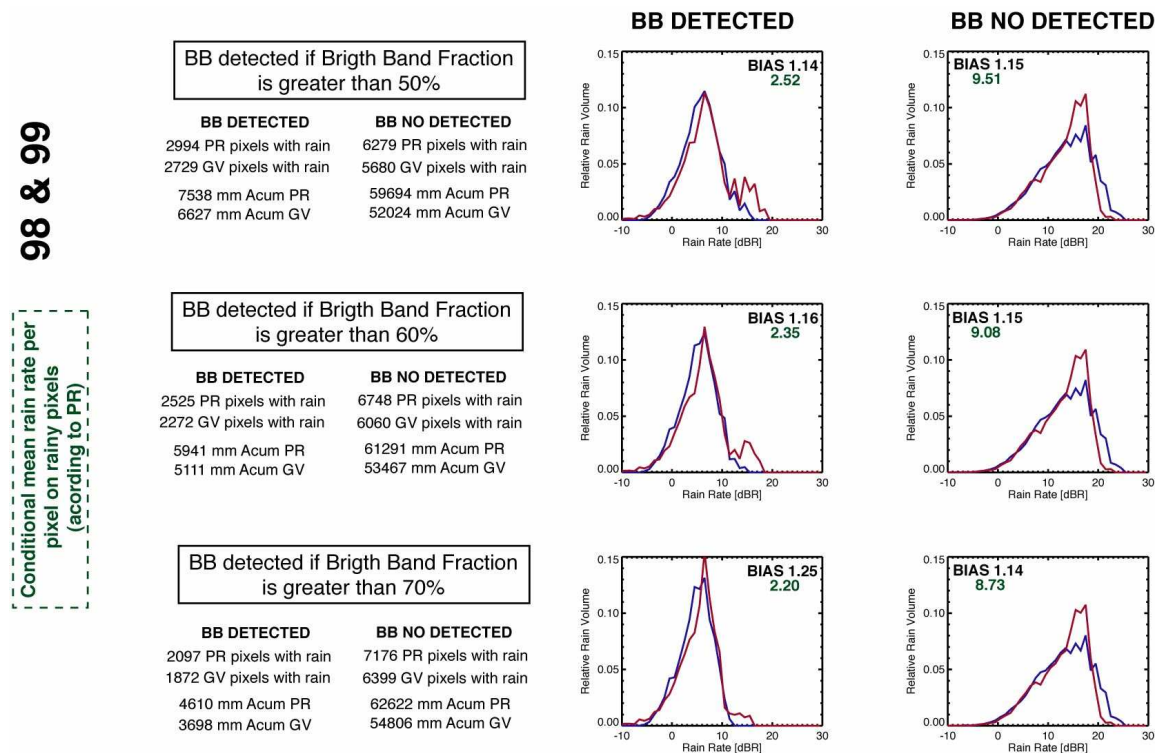

Figure 4.11: Distribution of rain volume as function of rain rate (in logarithmic scale: dBR=10·log(R)) for the Melbourne, Florida, WSR-88D (GV, 2A53 V5) and TRMM-PR (2A25 V5) datasets based on 42 overpasses during 1998-1999 period. Left panel shows the pdf for the pixels where BB has been detected using BBF. Right panel shows the pixels where BB has not been detected. Each row shows the results for a different threshold in the BBF (50%, 60% and 70%). TRMM-PR plotted in blue, GV in red. The number of rainy pixels, their rain accumulation, and the PR/GV rain volume bias for each rain type are indicated in the legend.

Another parameter used in Amitai (1999) classification scheme are the horizontal reflectivity gradients above the 0º isotherm. Horizontal gradient in the horizontal plane at height *h* above ground is calculated using equation 4.2 (P is the pixel of interest and X_i the surrounding pixels in a

3x3 window) that takes into account the distances between pixels in a window of 3x3 around the pixel of interest.

$$\nabla_H\left(h\right) = \frac{\left(\sum_{i=1,3,7,9}|X_i - P|\Big/\sqrt{2}\right) + \left(\sum_{i=2,4,6,8}|X_i - P|\right)}{9} \tag{4.2}$$

Pixels having high horizontal gradients are usually associated to convective rain, and pixels with low gradients associated with stratiform rain. Horizontal gradients are important from the point of view of spaceborne radars due to the non-uniformity of the precipitation inside the radar beam (NUBF problem). In the areas where horizontal gradients are high, the 2A25 algorithm will have problems to retrieve correctly the rain (Iguchi *et al.* 2000).

The classification scheme of Amitai (1999) uses these described variables to classify the pixels in 14 rain types (see Figure 4.12 for a description of the classes).
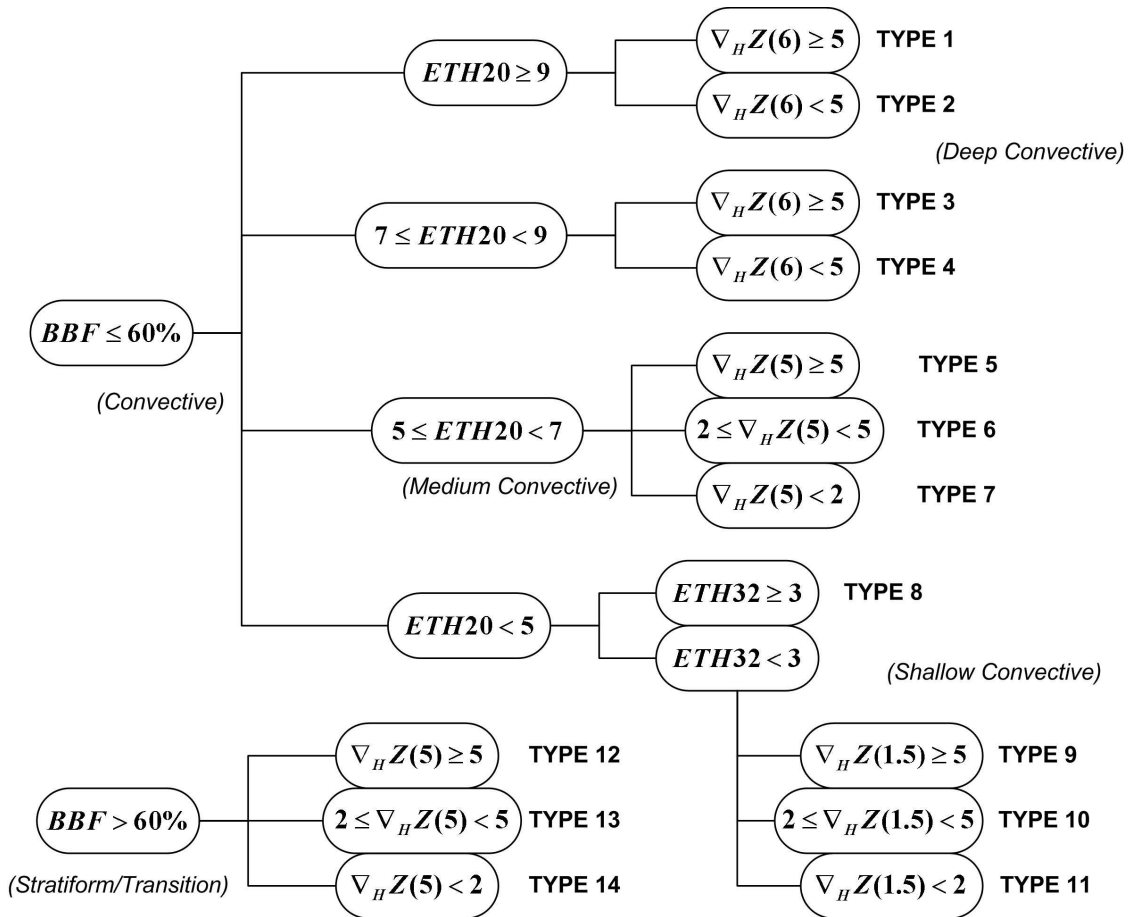
Figure 4.12: Classification schema used in this study (from Amitai 1999). BBF means the Bright Band Fraction as described in Rosenfeld *et al.* (1995), ETH*n* means Ecotop at *n* threshold (in dBZ) and $\nabla_H\left(h\right)$ is the horizontal gradient at height *h*.

Figure 4.13 shows the pdfs of each rain type resulting of this classification into 14 classes and from all 105 overpasses found in 1998-2002 period. For most rain types, the TRMM-PR pdfs are shifted

toward low rain rates relative to the GV pdfs (i.e., TRMM-PR overestimates probabilities of low rain rates, and underestimates probabilities of high rain rates). TRMM-PR overestimation at high rain rates (i.e., TRMM-PR pdf shifted toward high rain rates relative to the GV pdf) is found only in the rain types 2, 4 and 7. In these rain types the echo top were high, a bright-band signature did not exist (i.e., convective cells), but with smooth horizontal gradients. Weak horizontal gradients suggest that partial beam filling is not an issue. These types are also characterized by a higher averaged rain rate of TRMM-PR compared to that of the GV. According to Amitai *et al.* (2005) this could be because in heavy convection, a significant contribution to the total attenuation can come from mixed phase particles, and underestimating the fraction of the attenuation caused by the mixed phase region and overestimating the attenuation caused by the cloud water can yield overestimates of the near-surface rain. These three classes combined, contributed about half of the total rain amount (49% of the total TRMM-PR measured rain and 40% of the total GV measured rain). In these cases the TRMM-PR estimates exceeded the GV estimates by 18%.

The major differences in pdf shape can be seen in type 12, but it is due to the fact that there are few points in this category because areas with bright band detected and high horizontal gradients are rare.

In the same Figure 4.13 we can observe that the average rain rate per pixel for each rain type, and the trend in the average rain rate per pixel observed from type-to-type in the GV data set is in accordance with the results from the simulation performed by Amitai (1999). But looking to the TRMM-PR we can see that this is not the case suggesting that probably the GV data are more representative of the truth.
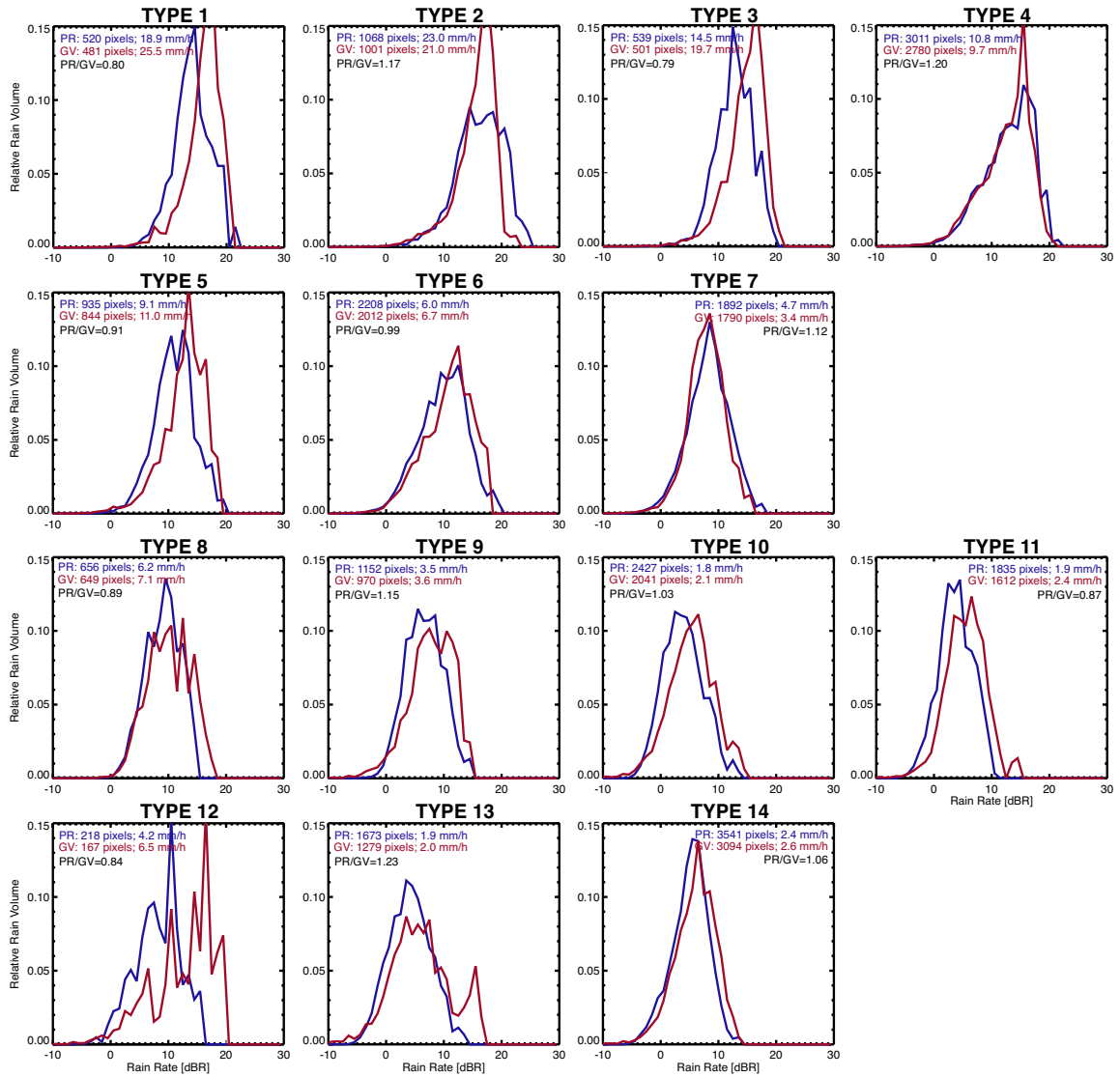
Figure 4.13:   Distribution of rain volume as function of rain rate (in logarithmic scale: dBR=10·log(R)) for the Melbourne, Florida, WSR-88D (GV, 2A53 V5) and TRMM-PR (2A25 V5) datasets based on 105 overpasses during 1998-2002. Each panel shows the pdfs for a different rain type from Figure 4.12. TRMM-PR is plotted in blue, GV in red. The number of rainy pixels, their average rain rate, and the PR/GV rain volume bias for each rain type are indicated in the legend. Figure from Amitai *et al.* (2005).

4.2.2. Is V6 better than V5?

NASA PPS is processing the data from TRMM satellite into standard products. Every time the algorithms used are changed, the version number of the product is changed and all the data from the beginning of the mission reprocessed to the new version. When the new version (Version 6 [V6]) of the 2A25 algorithm was started to be used, the natural question was how it compares to the previous version (Version 5 [V5]).

Figure 4.14: The first panel shows the TRMM-PR 2A25 Version 5 product for the March 9th, 1998 overpass in Melbourne, Florida. The second panel shows the TRMM-PR 2A25 Version 6 product for the same event. Last panel shows the GV 2A53 Version 5 product. Rings represent the 15 and 100 km distance circles from the radar site, and the lines the TRMM-PR swath limits.

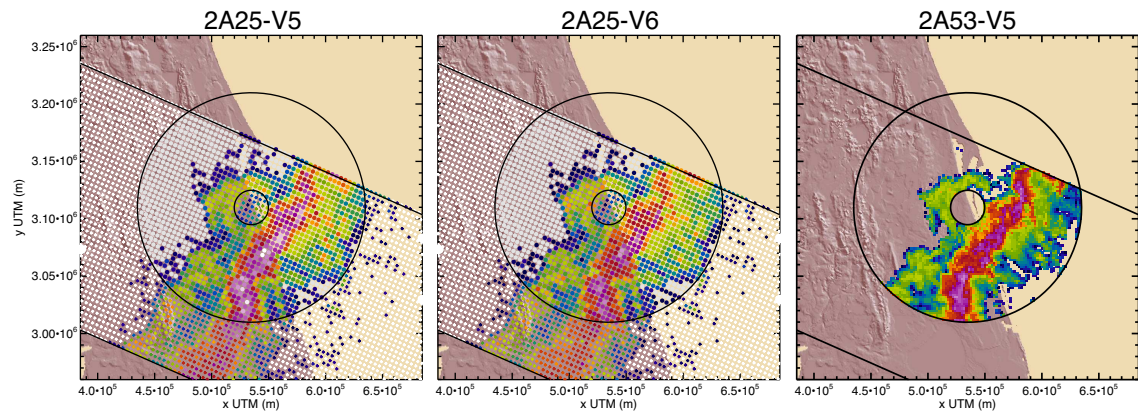Looking to Figure 4.14 we can seen that TRMM-PR 2A25 V6 product produces lower rain rates than previous version (V5) for this specific case. In the same figure we can se the GV estimates, which seem to be closer to the TRMM-PR 2A25 V6 estimates for this specific case. Is this the general case? This sub-chapter compares both versions of the TRMM-PR 2A25 product against GV 2A53 Version 5 product to show the differences between them under different conditions.

The TRMM-PR 2A25 V6 product includes a new variable called "estimated surface rain rate" as oppose to the "near surface rain rate" of V5 product (Japan-Aerospace-Exploration-Agency 2005). This new variable is based on extrapolating the rain rate values to the surface using a vertical reflectivity profile (rain type dependent) but always decreasing toward the surface. We found that TRMM-PR Version 6 overall rain amounts have been reduced compared to the previous version. The total rain amount for the 105 overpasses over central Florida of the 1998-2002 period, based on the 2A25 V6 is about 6% less than the near-surface rain rate product of 2A25 V5.

Figure 4.15 shows another example of comparison for one TRMM-PR overpass over central Florida (February 17th, 1998). Again it is clear that the TRMM-PR 2A25 retrieves less rain in convective zones in V6 than in V5. In the stratiform area, the retrievals are quite similar. The GV 2A53 V5 estimates (1 minute difference against TRMM-PR overpass) seem to perform closer to the V6 than to the V5. In the pdfs of rain by volume (calculate through equation 4.1 using a common grid described in the previous sub-chapter) we can see that the TRMM-PR V6 and the GV pdfs agree quite well despite the double peak of the satellite curve. The TRMM-PR V5 pdf is shifted towards lower rain rates and has a very different shape: it does not have values over 17-18 dBR (with a sharp end), and it gives much more probability to the bins in the range 5-15 dBR.
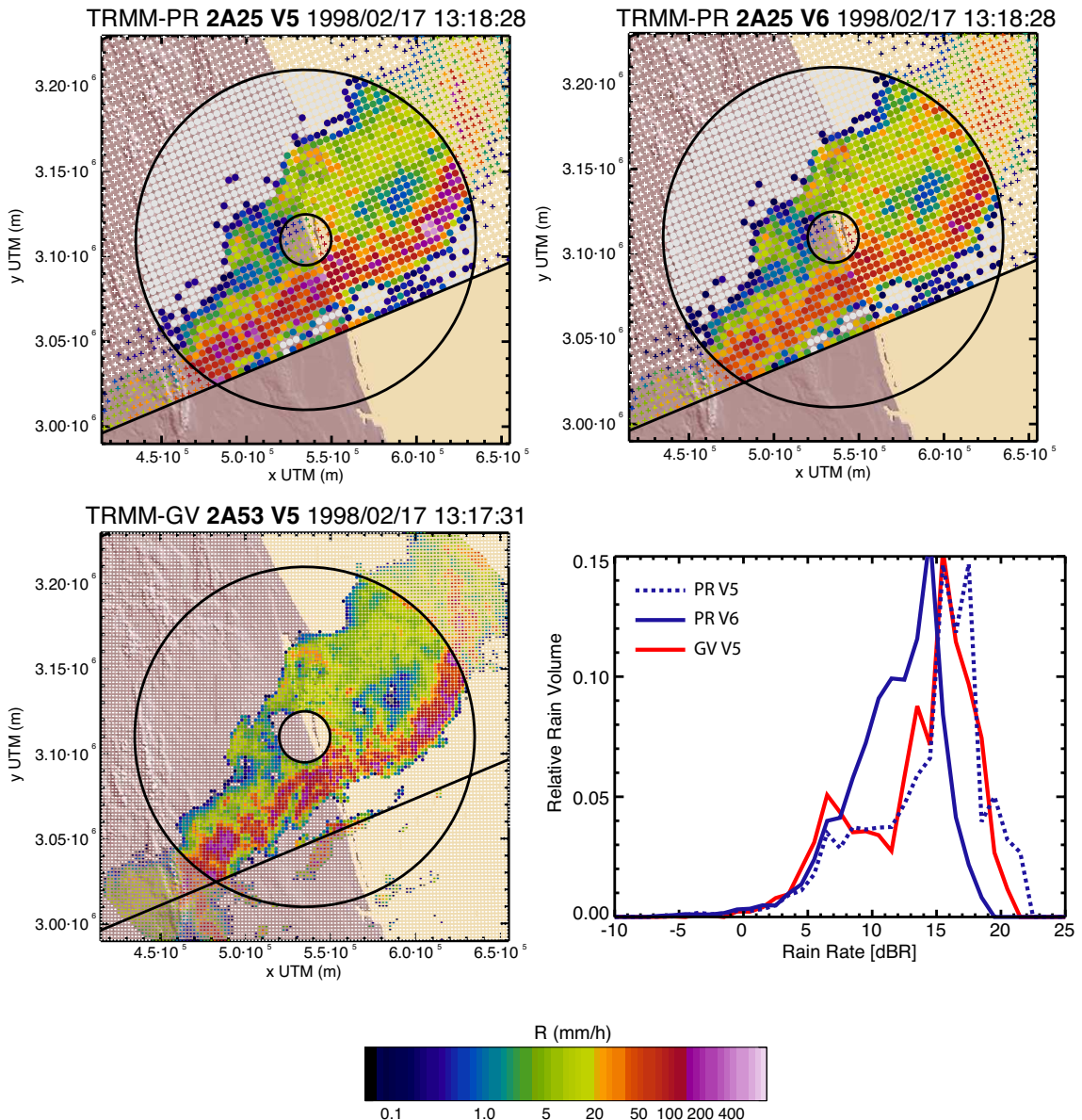
Figure 4.15: Comparison of rain rate fields and their pdfs for the event of February 17th, 1998 in central Florida. First panel shows TRMM-PR 2A25 Version 5, second panel shows TRMM-PR 2A25 Version 6, third panel shows GV 2A53 Version 5 product, and last panel shows the associated pdfs. Rings represent the 15 and 100 km distance circles from the radar site, and the lines the TRMM-PR swath limits.

A comparison of the pdfs for 209 TRMM overpasses over central Florida is shown in Figure 4.16. Two pdf curves for the TRMM-PR estimates are shown; one is based on the most recent version of the TRMM 2A25 algorithm (V6) and the other on the previous version (V5). The GV surface rain rate estimates are taken from the product 2A53 in the latest version (V5). The pdfs are calculated as described in section 4.2.1.2 and using equation 4.1. For these 209 overpasses TRMM-PR overestimated GV by 5% in its Version 5, and underestimated GV by 12% in its Version 6. Average rain rate per pixel in TRMM-PR changed from 5.0 mm/h in V5 to 4.2 mm/h in V6, compared to the 5.8 mm/h of the GV estimates. So from this point of view, the old version V5 of

satellite products seems to perform closer to the GV estimates than the new version. To look in detail where the differences occur we will use classification again.

Figure 4.16: Distribution of rain volume as function of rain rate (in logarithmic scale: dBR=10·log(R)) for the Melbourne, Florida, WSR-88D (GV, 2A53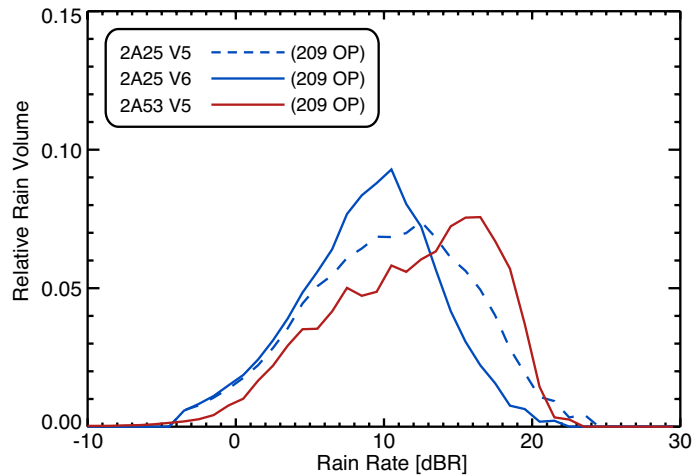 V5), TRMM-PR (2A25 V5) TRMM-PR (2A25 V6) and datasets based on 209 overpasses and co-located GV data within 15 and 100 km of ground radar site.

4.2.2.1 Classification

Figure 4.17 presents the pdfs for overpasses in central Florida with the data divided into convective and stratiform rain types. The TRMM_PR 2A-23 classification algorithm is used (Awaka *et al.* 1997) in its last version (V6) (see Japan-Aerospace-Exploration-Agency 2005 for a description of the changes between versions). Modification to the classification algorithm resulted in a slight different separation of the data sets, but we considered not affecting significantly the resulting pdfs. We can see in this figure how the three curves agree quite well for stratiform precipitation while for convective precipitation TRMM-PR curves are shifted to lower rain rates (seen also in Figure 4.10 for V5 and 105 overpasses). This effect is increased with the change from V5 to V6. The pixels not classified in the 2A23 algorithm are very few, representing 2% of the total rain amount, and without a well defined pdf (Figure 4.17, third panel).

We found that as result of changing from V5 to V6, the TRMM-PR total rain amount has been reduced by about 15%. Using the TRMM-PR 2A23 classification product, we found the convective rain was reduced by about 26% while the stratiform rain was increased by 13%. The trend observed in the three convective pdfs (Figure 4.17) dominates the trend observed in the pdfs prior to any classification (Figure 4.16). The fraction of TRMM-PR rain classified as convective is about 60%.
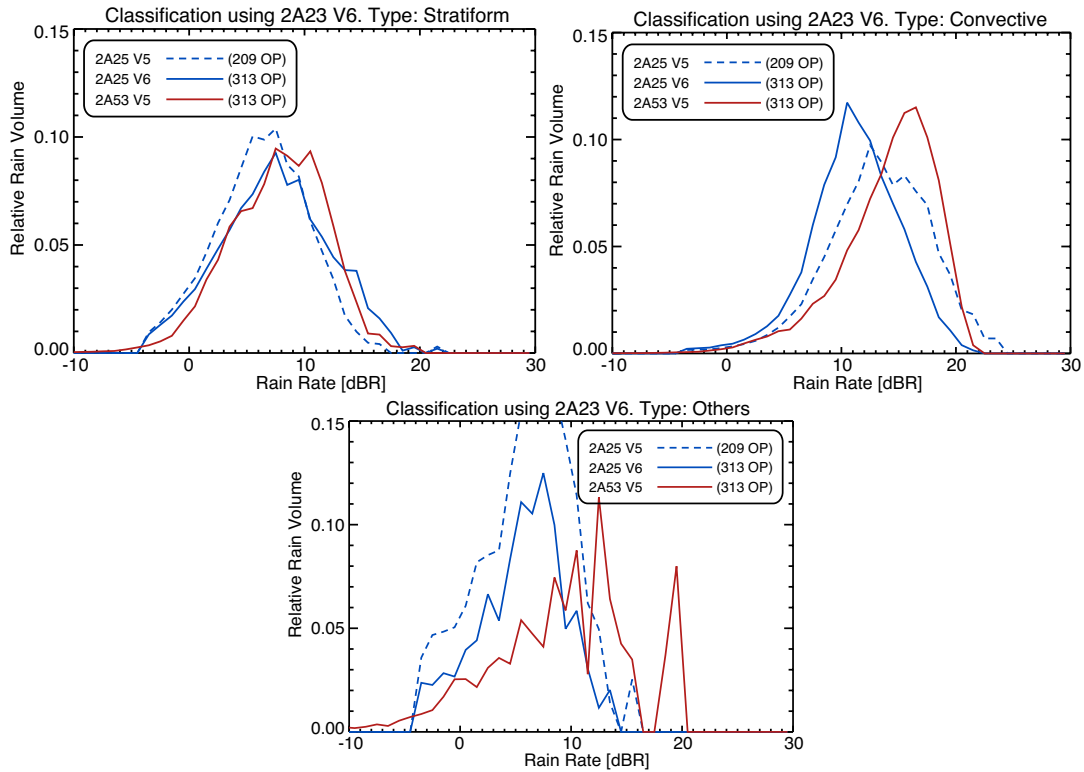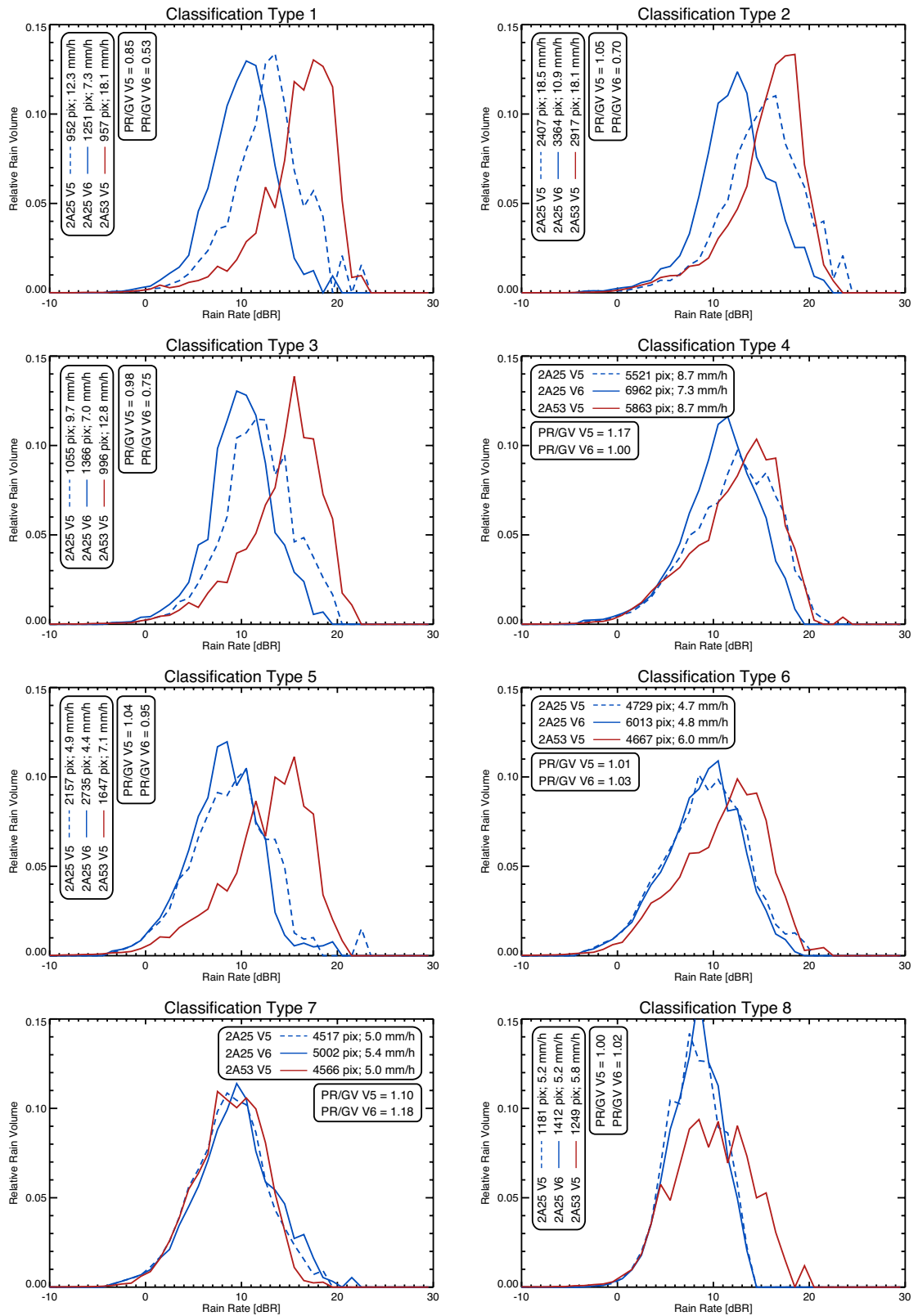
Figure 4.17: Distribution of rain volume as function of rain rate (in logarithmic scale: dBR=10·log(R)) for the Melbourne, Florida, WSR-88D (GV, 2A53 V5), TRMM-PR (2A25 V5) and TRMM-PR (2A25 V6) datasets based on 209/313 overpasses and co-located GV data within 15 and 100 km of ground radar site. The first panel shows the pixels classified as stratiform according to the TRMM 2A23 V6 standard product, second panel the pixels classified as convective, and last panel the pixels unclassified in this product.

To look at more detail into the differences between TRMM-PR 2A25 V5 and V6, we performed the classification of Amitai (1999) in 14 rain types (see Figure 4.12 and previous sub-chapter). Figure 4.18 presents the pdfs for 209 overpasses in central Florida with the data divided into rain types using this classification schema. On this figure we can see how types 7 and 14 (both characterized by low echo tops and smooth horizontal gradients) all three pdfs are very similar. In the types 9, 10 and 11, all of them characterized by low echo tops and medium horizontal gradients, differences between TRMM-PR and GV start to appear (discussed in previous sub-chapter), but not between TRMM-PR versions. We can also see in this figure that in types characterized by high eco tops and high horizontal gradients (types 1, 2, 3 and 4) there are differences between the three curves, being the TRMM-PR 2A25 V5 curve closer to the GV than the TRMM-PR 2A25 V6. These characteristics (high echo tops and high horizontal gradients) indicate strong convection, and the principal change between V5 and V6 in 2A25 product is the algorithm for attenuation correction (Japan-Aerospace-Exploration-Agency 2005); all this might indicate that V6 is not solving the attenuation problem as well as its previous version for such rainfall types.
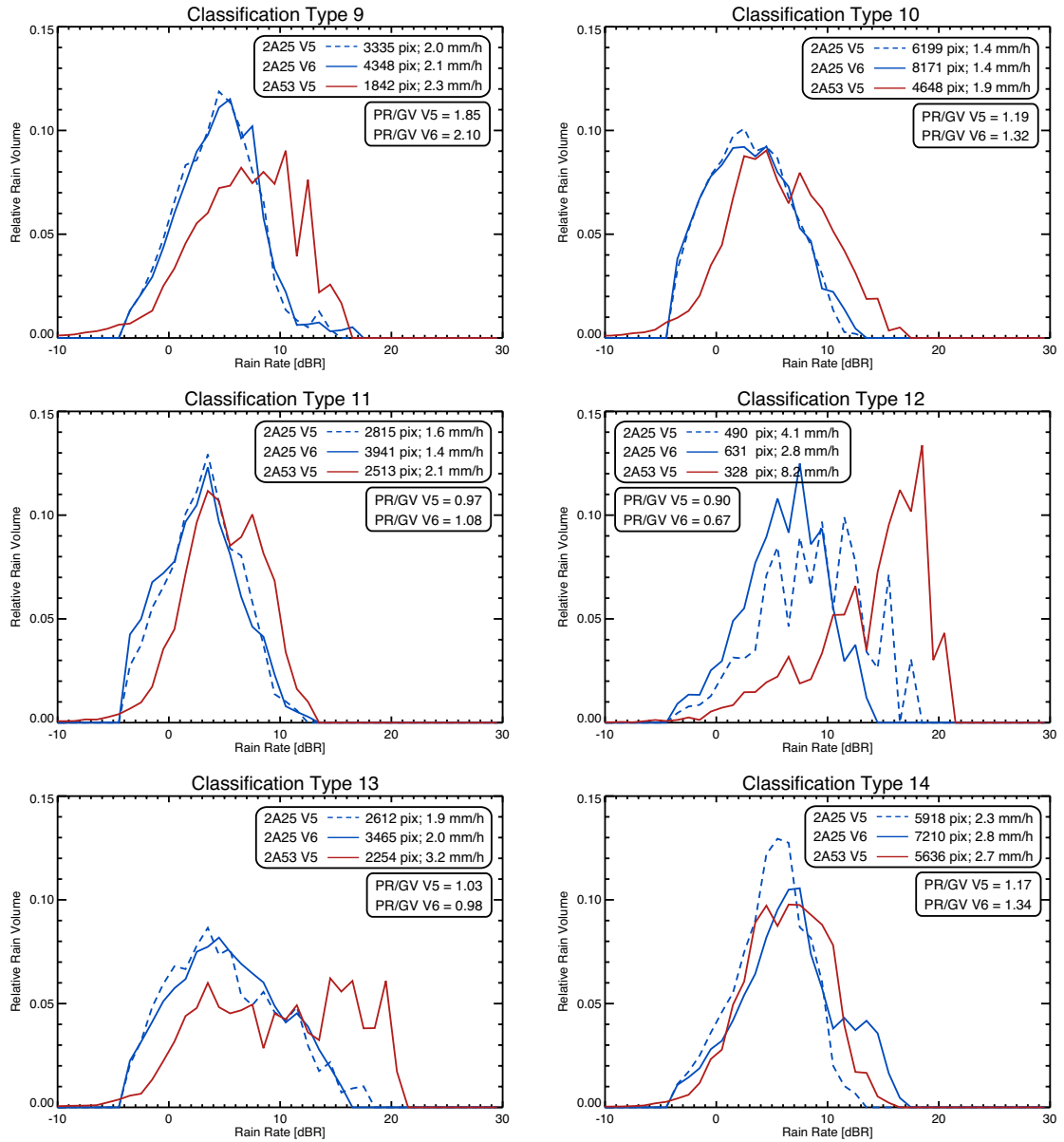
Figure 4.18: Distribution of rain volume as function of rain rate (in logarithmic scale: dBR=10·log(R)) for the Melbourne, Florida, WSR-88D (GV, 2A53 V5), TRMM-PR (2A25 V5) and TRMM-PR (2A25 V6) datasets based on 209 overpasses and co-located GV data within 15 and 100 km of ground radar site. Each panel shows one rain type according to Amitai (1999) classification (see Figure 4.12). Rainy pixels in each category, average rain rate per pixel and bias between instruments are shown in the legend of each plot.

4.2.3. CONUS Composite

Rain rate estimates obtained from spaceborne radar observations (e.g. from TRMM-PR) compared with ground radar observations reveal significant discrepancies in the shape of the pdfs and in the location of the maxima (see section 4.2.1, Amitai *et al.* 2006; Amitai *et al.* 2005). The discrepancies were found comparing the pdf of TRMM-PR products and the TRMM GV gauge adjusted radar

products available over Central Florida. However, integrating the pdf rain rates, the rainfall accumulations were found to be remarkably similar.

To check if those discrepancies in the pdfs exist in other places and to better identify and resolve such significant discrepancies, here TRMM-PR data are compared against the new National Oceanic and Atmospheric Administration [NOAA] National Severe Storms Laboratory [NSSL] experimental radar products (Q2), of high-resolution (1 km², 5 min) instantaneous rainfall rate mosaics, available over the entire continental U.S. [CONUS] (see Vasiloff *et al.* 2007 for a complete description of the product). The Q2 products are a set of several QPE products in Cartesian coordinates with 0.01° horizontal resolution over the entire CONUS. The basic product is a 3D-reflectivity mosaic consisting of 31 levels in height. The 3-D reflectivity mosaic product is obtained first transforming the volume scan base reflectivity data (quality controlled) from their native spherical coordinates onto a 3-D regular Cartesian grid for each radar, and then merging the individual radars to produce the 3-D CONUS mosaic via a distance-weighted scheme. The Q2 radar-only rain rate product, used here for comparison with TRMM-PR, is derived from the reflectivity product using the U.S. National Weather Service convective, stratiform, and tropical Z-R relations. Reflectivities higher than 49 dBZ are considered hail and assigned to this threshold value. Current Q2 radar products do not include an instantaneous gauge-adjusted rain rate mosaic.

This secction presents the first results of the TRMM-PR against Q2 comparisons based on analyzing several cases studies with the aim to provide some indication of the magnitude of the discrepancies between both estimates in these large coverage products.

4.2.3.1   Data matching and regridding

The rain rates used to derive the pdfs are based on co-located TRMM-PR and Q2 radar observations within the TRMM-PR swath. TRMM-PR estimates used are taken from 2A25 standard product in its latest version (Version 6). Only TRMM-PR overpasses over the CONUS with at least 200 rainy pixels with a rain rate greater than 10 mm/h are used in this work.

Products are matched in time taking for each pixel the Q2 rain rate value of the product that is closest in time to the TRMM-PR observation time over that specific pixel. Match in space is done by transforming both to a common grid of 0.04° horizontal resolution. The TRMM-PR conversion is based on interpolating the IFOV data through a Delaunay triangulation process as described in previous sub-chapter.

The effect of the regridding on the total rain amount, the total rainy area, and the pdf shape depends on the regridding algorithm being applied, being difficult to conserve them all in the process. In this study, we chose to keep the total rain amount, and to minimize the effects of light rain areas by using the volumetric pdf as the standard of comparison. Comparisons of the TRMM-

PR rain amount before and after regridding show changes of less than 0.5% in the rain volume. The TRMM-PR rainy area increases relative to the original TRMM-PR rainy area after regridding. This is due to the fact that pixels in the rain/no-rain boundaries get rain values after regridding if they are partially filled. The magnitude of this effect depends on the length of the boundary, that if, the frontier between rain and no-rain. However, the TRMM-PR regridded rainy area was still found to be smaller than the Q2 rainy area. This additional rainy area due to regridding is usually associated with weak intensities, and therefore, does not significantly affect the volumetric pdfs.

Figure 4.19 shows the increase in rain volume in the regridding process for the overpass of May 11th, 2008, -shown in Figure 4.23 (second panel)- depending on the threshold applied afterwards to define non rainy pixels. Figure 4.20 shows the increase in rainy area for the same event, also depending on the threshold applied afterwards to define non rainy pixels. This is an extreme case due to large number of isolated rainy IFOVs that create a large rainy area after the regridding.

Figure 4.19: Increase in rain volume after the regridding process depending on the rain rate threshold applied, based on the TRMM-PR May 11th of 2008 case shown in Figure 4.23.
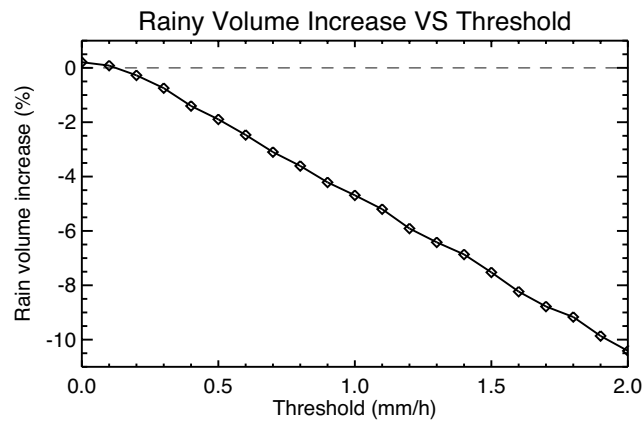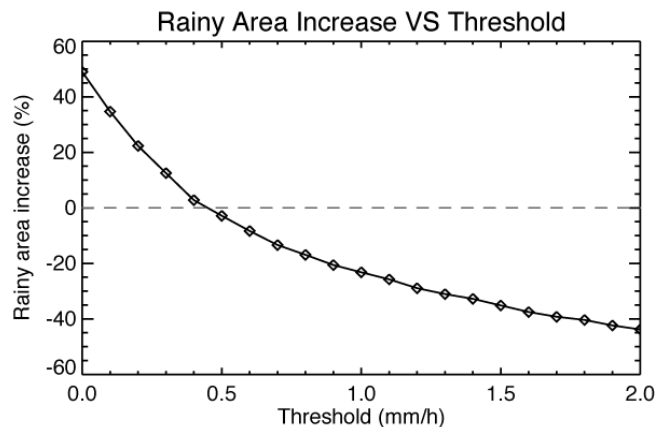

Figure 4.20: Increase in rainy area after the regridding process depending on the rain rate threshold applied, based on the TRMM-PR May 11th, 2008, case shown in Figure 4.23.

Stability of the Q2 pdfs has been studied by Amitai *et al.* (2009), showing that while correlation between TRMM-PR and Q2 fields decrease quickly, the pdf shape remains quite stable, being the

differences between consecutive Q2 products (5 min time difference) much smaller than the differences between TRMM-PR and Q2 pdfs during an overpass.

4.2.3.2 Results

A TRMM-PR rain rate estimate for an overpass in Alabama and Georgia (USA) is presented in Figure 4.21 together with Q2 rain rate estimates. The difference between both products is less than a minute. The rain volume bias between both instruments is low (6% of TRMM-PR overestimation). We can observe the sharp cut-off in the Q2 pdf due to the 49 dBZ threshold of this product, and the shift of this curve towards higher rain rates. This shift of the ground estimates towards higher values was already seen by Amitai *et al.* (2006) using a single radar site.

Figure 4.22 shows the TRMM-PR overpass in the Gulf of Mexico over the hurricane Humberto on September 13th, 2007 at 9:10 UTC. In this overpass TRMM-PR underestimates the total rain amount by 14% compared to Q2. Rain area is underestimated by TRMM-PR by a 17%, but the Q2 rainy pixels where TRMM-PR did not register rain, contribute less than 1% of the total rain volume. Also in this example can be seen a double peak in both pdfs (more defined in Q2 estimates) due to the mix of the two convective and stratiform areas.

May 11th, 2008, event (characterized by high presence of hail) is shown in Figure 4.23. At the time of the TRMM-PR overpass a tornado was reported under the nadir track of TRMM. In this case TRMM-PR overestimated Q2 by 7%.

Figure 4.24 shows the tornadic thunderstorms (84 tornadoes associated; 57 people killed) observed three times by TRMM-PR and Q2 on February 6th, 2008. We can see that shapes of the pdfs from overpasses are very similar, and in the three overpasses TRMM-PR pdfs are shifted towards lower rain rates respective to the Q2 pdfs. Differences in the peak of the distribution are larger than 5 dBR and TRMM-PR underestimated the rainfall up to a 39% probably due to the presence of hail.

Amitai *et al.* (2009) did an extensive comparison of TRMM-PR and Q2 estimates over 98 overpasses obtaining an overall bias of 0.92 (8% underestimation of TRMM-PR) and that while TRMM-PR pdf is log-normal, Q2 pdf seems to have a double peak (convective and stratiform). However, discrepancies from overpass to overpass shown in previous sub-chapter have not yet been resolved. In general TRMM-PR pdfs are shifted towards lower rain rates relative to the Q2 pdfs (in agreement with Amitai *et al.* 2006 and shown in previous sub-chapters).

Figure 4.21: TRMM-PR overpass on May 12th, 2007, at 22:30h UTC. Original resolution Q2 (first panel) and TRMM-PR 2A25 (second panel) rain rate fields and their corresponding pdfs of distribution of rain volume as function of rain rate (third panel) (in logarithmic scale: dBR=10·log(R)). Rainy pixels, average rain rate per pixel and bias between instruments are shown in the legend of the plot.
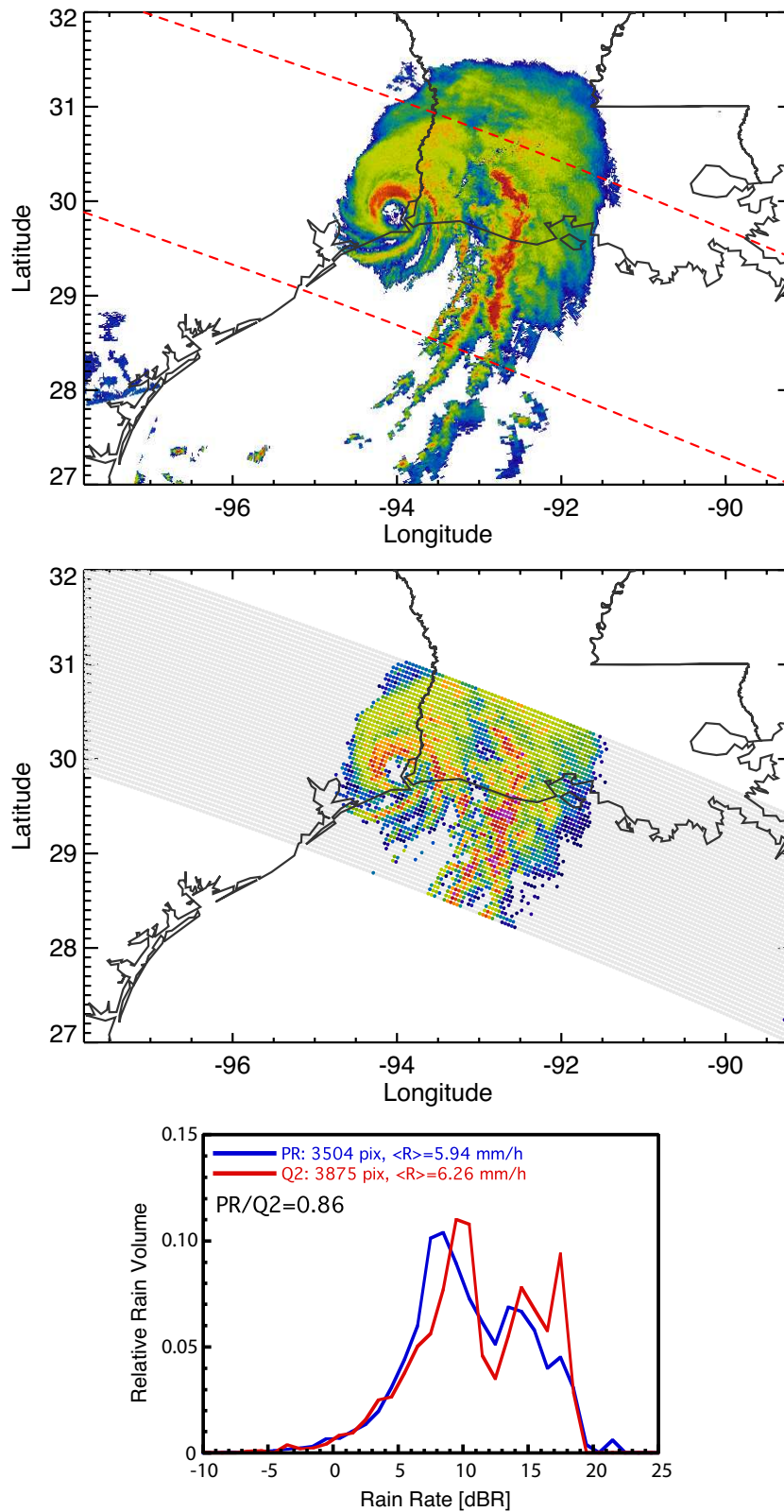
Figure 4.22: TRMM-PR overpass on September 13th, 2007, at 9:10h UTC (Hurricane Humberto). Original resolution Q2 (first panel) and TRMM-PR 2A25 (second panel) rain rate fields and their corresponding pdfs of distribution of rain volume as function of rain rate (third panel) (in logarithmic scale: dBR=10·log(R)). Rainy pixels, average rain rate per pixel and bias between instruments are shown in the legend of the plot.
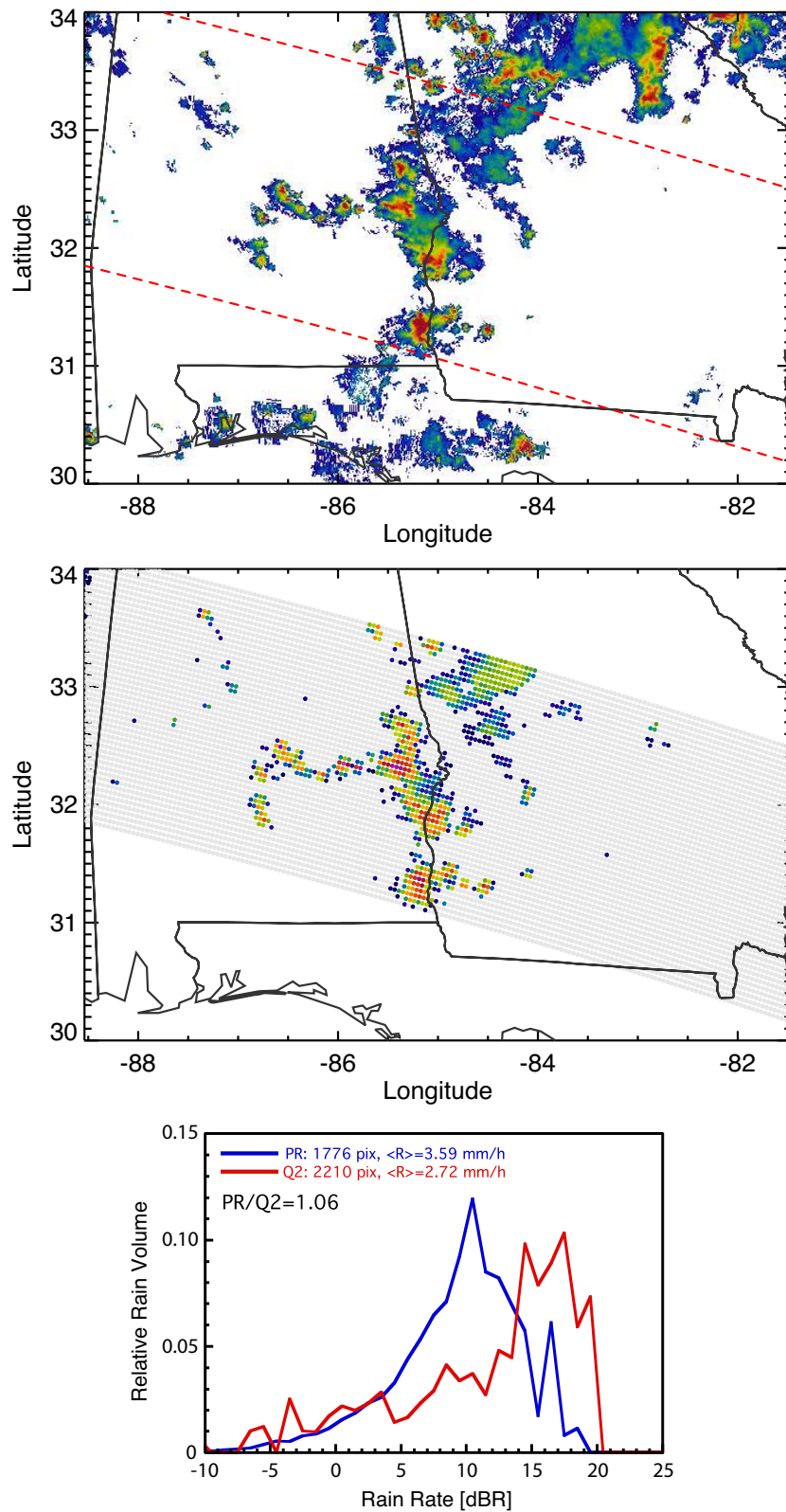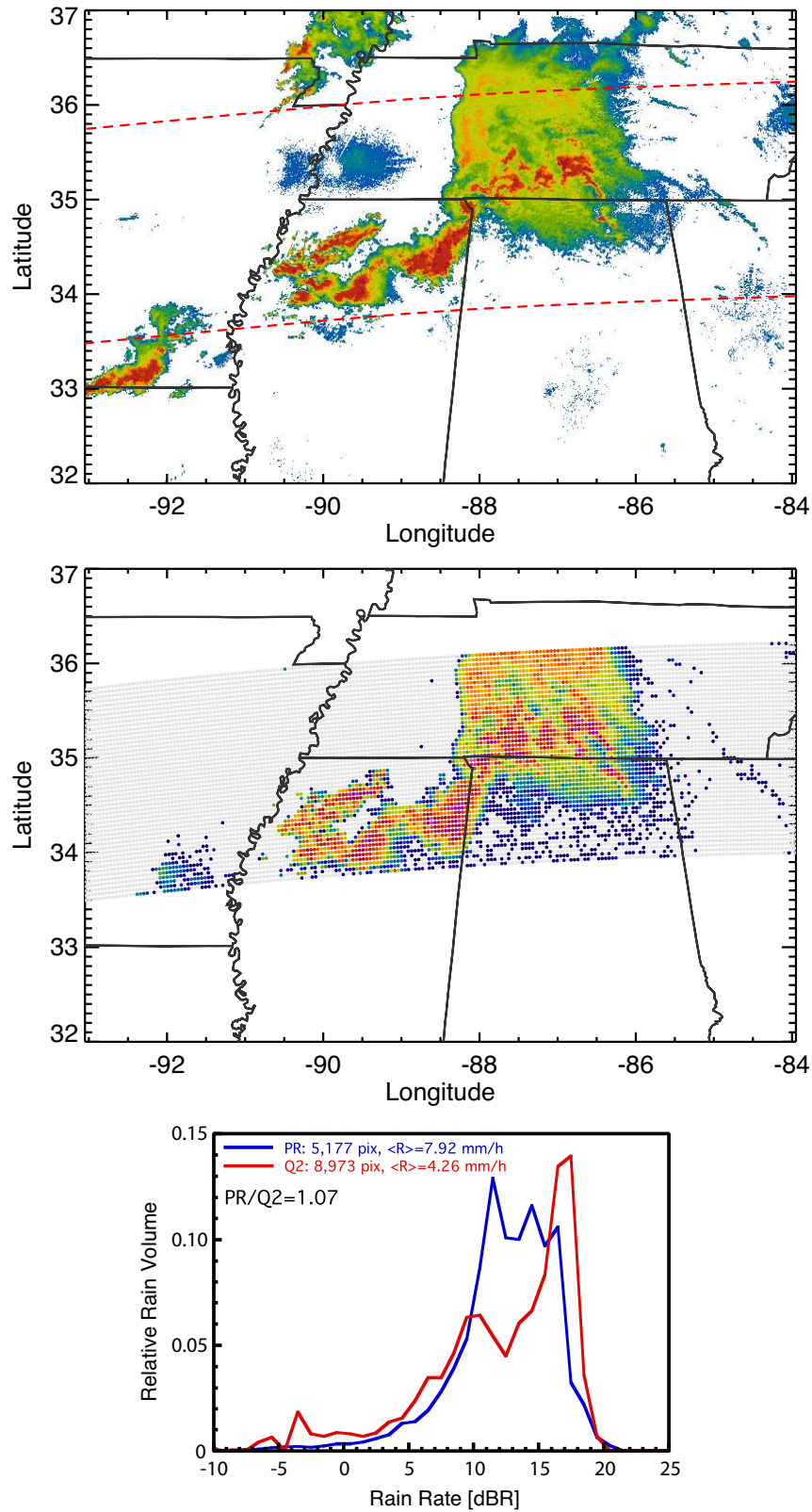
Figure 4.23: TRMM-PR overpass on May 11ᵗʰ, 2008, at 4:00h UTC. Original resolution Q2 (first panel) and TRMM-PR 2A25 (second panel) rain rate fields and their corresponding pdfs of distribution of rain volume as function of rain rate (third panel) (in logarithmic scale: dBR=10·log(R)). Rainy pixels, average rain rate per pixel and bias between instruments are shown in the legend of the plot.
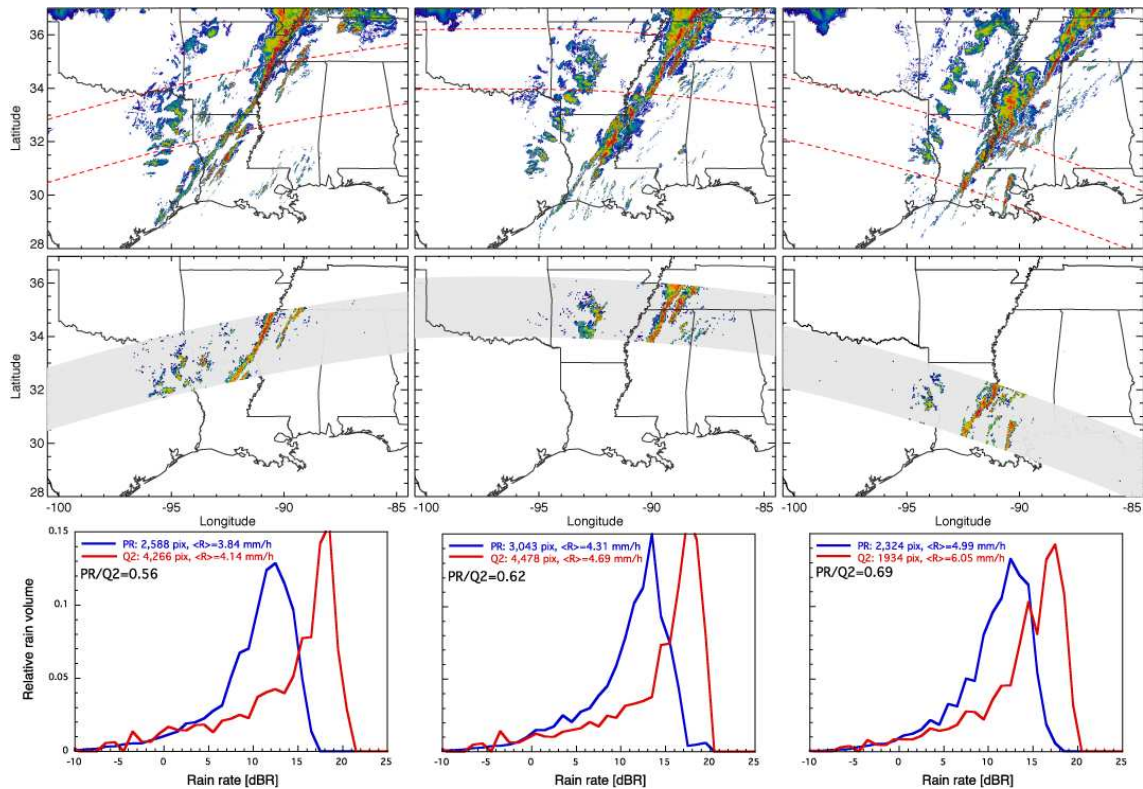
Figure 4.24: TRMM-PR overpasses on February 6th, 2008 at 3:30h, 5:10h and 6:45h UTC.. Original resolution TRMM-PR 2A25 (first panel) and Q2 (second panel) rain rate fields and their corresponding pdfs of distribution of rain volume as function of rain rate (third panel) (in logarithmic scale: dBR=10·log(R)). Rainy pixels, average rain rate per pixel and bias between instruments are shown in the legend of the plot.

## 4.3. Summary, conclusions and future work

Combining statistical and physical validation approaches provides an opportunity for verification of spaceborne radar estimates of precipitation. An example of this has been presented in this chapter, using pdfs to compare TRMM-PR against ground observations. The pdfs are not aimed to assess objectively and precisely the estimation errors, rather to evaluate statistically the relative performance of the estimates and algorithms at different conditions. They are used to detect situations of large discrepancies between the ground- and the space-based radar estimates that should be further investigated.

This comparison framework has the potential for "globalization" by extrapolating uncertainties found in TRMM-PR estimates to regions not covered by ground equipment but with same precipitation characteristics. Matching TRMM-PR pdf with the ground radar estimates can provide us with a relationship between the two rain rate estimates that could be used to adjust the spaceborne radar estimates in places not covered by ground equipment.

Results of comparing rain rate distributions from TRMM-PR 2A25 estimates with those from co-located GV radar estimates at central Florida based on the 1998-2002 period have been presented

before and after classification into rain types. The results provide a brief review of how well compare both rainfall estimates under different circumstances. Overall, we found the TRMM-PR to underestimate the rain by 4%, but also to not detect 4.5% of the rain as compared to the GV radar estimates. The differences between TRMM-PR and GV regarding the rain rate peak contribution in V5 –more than 3 dBR– and in V6 –more than 5 dBR– (see Figure 4.16) might be large for hydrological applications. The question is if this is the general case and which of the curves (satellite-based or ground-based) better represents the rain rate true distribution.

The quality of ground radar data varies from site to site. Also the TRMM-PR performance might vary with different meteorological conditions, different surfaces (e.g., land, ocean), and with distance from the nadir-line. Results presented provide us with some information on how sensitive the pdf is to different TRMM-PR algorithms. In this sense, the last two versions of TRMM-PR 2A25 rain retrieval algorithm (Version 5 and 6) have been compared between them. The discrepancies between the TRMM-PR and the GV pdfs of rain rates were found to be on the same order as the discrepancies between the two TRMM-PR pdfs based on the last two PR versions. Surprisingly, the estimates based on the previous version of TRMM-PR algorithms (V5) agreed better with the GV than the new version (V6). These problems have been recognized by NASA PPS and should be solved in next version (Version 7) now under testing and that will be released soon.

TRMM-PR has been compared on extreme events against the new high-resolution Q2 product over all CONUS, which allows a large dataset for comparison.

Q2 significantly increases the sample size of data available for comparisons compared to previous studies and also could permit classification of the data by rain type, topography, geographic region, and other parameters in order to evaluate the algorithms and products under different conditions.

Future work in TRMM-PR against ground radar comparisons should incorporate improved alignment methodologies (Bolen and Chandrasekar 2003) to reduce geometric distortions and improve the intercomparison. Also there is the need to establish uncertainty values independently for the satellite rainfall estimates and the GV estimates based on the algorithms and their assumptions. Then the overlap zone of both uncertainties could be studied.

A problem that should be further investigated is the performance of TRMM-PR 2A25 algorithm under land and ocean conditions. Figure 4.25 shows Hurricane Jeanne as seen from TRMM-PR and ground radar. In the TRMM-PR 2A25 image, it is easily to see the difference between land and ocean in the rain rate estimates, that looking to the GV radar seems not to appear. A study needs to be undertaken to determine if this is the general case or if not, the circumstances under which it occurs should be determined.
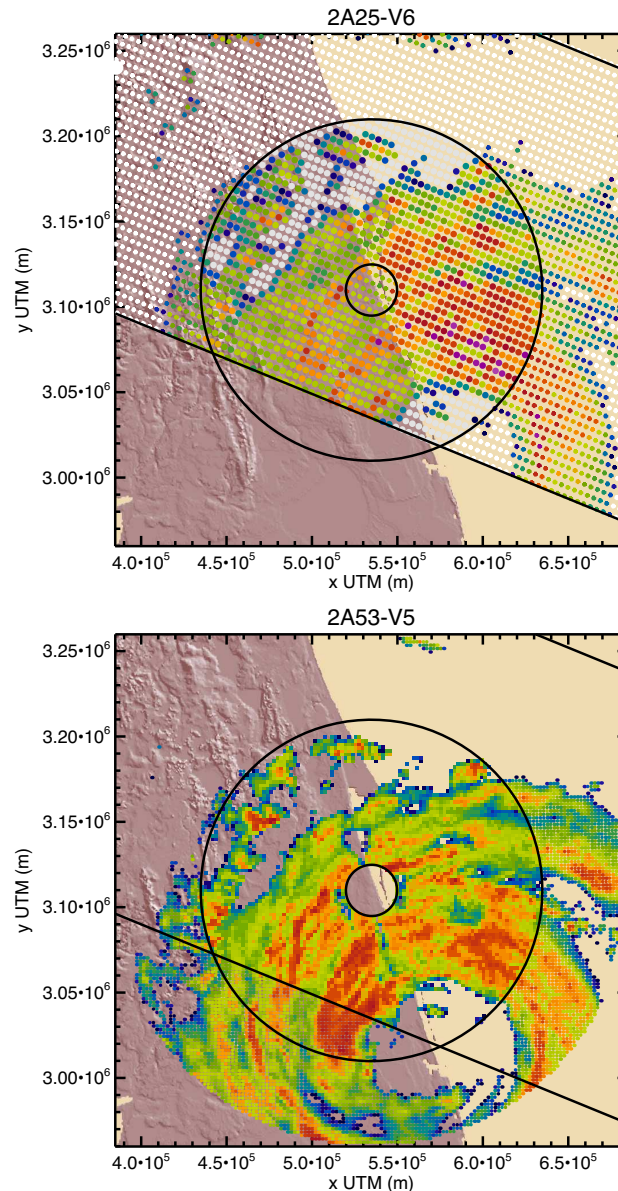
Figure 4.25: TRMM-PR orbit over central Florida on September 26th, 2004 (Hurricane Jeanne). The top panel shows the TRMM-PR 2A25 Version 6 rain rate estimates, and the bottom panel the GV 2A53 rain rate estimates. Difference between them is less than a minute.

Next step in the TRMM-PR against ground-based estimates should be the three-dimensional comparison. For example Figure 4.26 shows the TRMM-PR event of September 13th, 2008 when TRMM-PR overflew Hurricane Ike in the moment it made landfall. The same figure shows the estimates of Q2 at the same time (less than a minute difference). At the north of the hurricane eye we can see an area where TRMM-PR highly overestimates Q2. Is the attenuation overcorrected in 2A25 V6 algorithm due the presence of hail? Comparing both estimates at different heights could allow for a better understand of the discrepancies and the satellite algorithms performance.
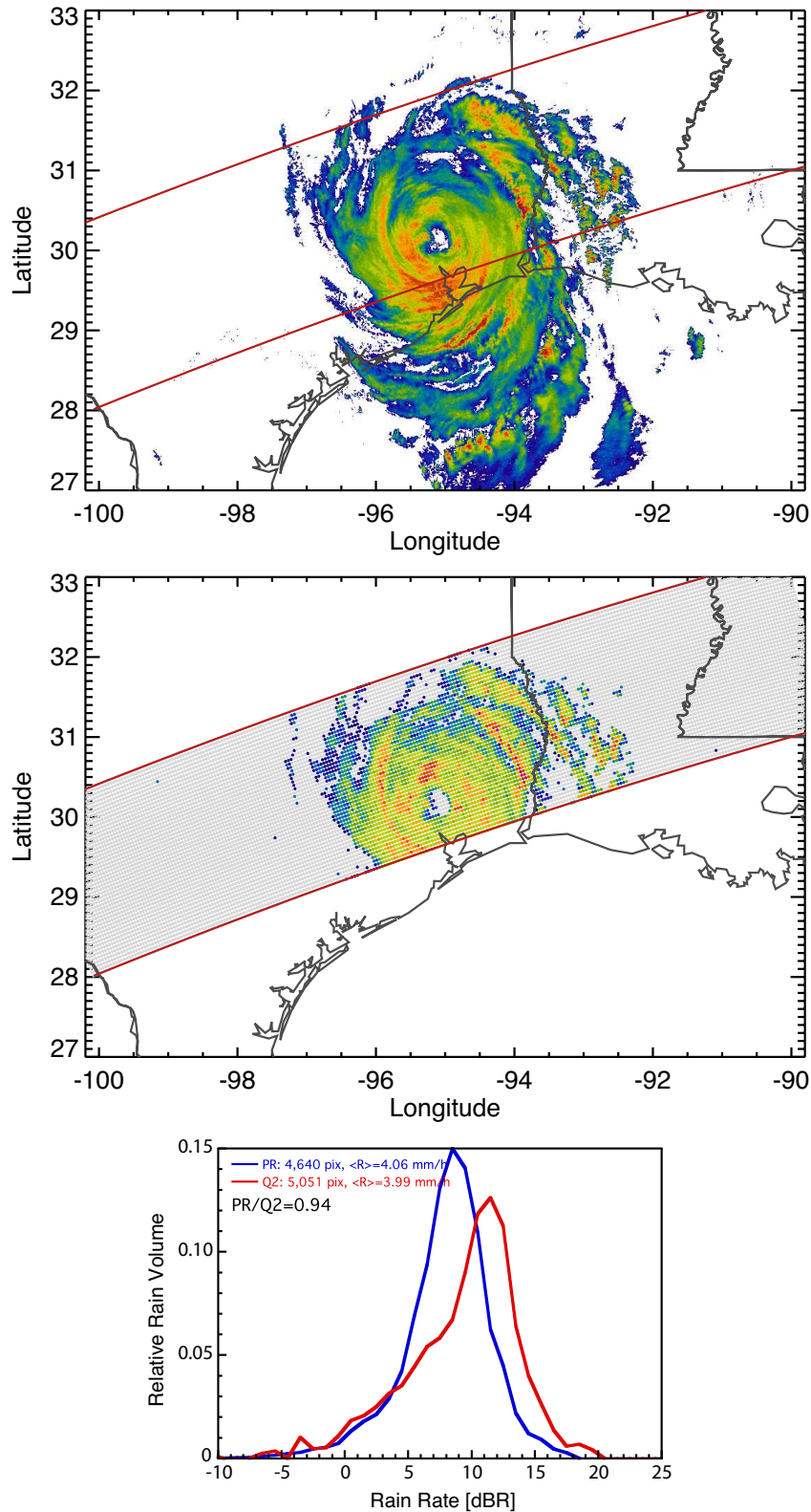
Figure 4.26: TRMM-PR overpass on September 13th, 2008, at 11:15h UTC (Hurricane Ike). Original resolution Q2 (first panel) and TRMM-PR 2A25 (second panel) rain rate fields and their corresponding pdfs of distribution of rain volume as function of rain rate (third panel) (in logarithmic scale: dBR=10·log(R)). Rainy pixels, average rain rate per pixel and bias between instruments are shown in the legend of the plot.

CHAPTER 5

General conclusions

Although many efforts have been devoted in the last years to improve radar quantitative precipitation estimates (QPE), very few works studied and characterized the uncertainty remaining in the estimates after all the algorithms were applied. In this thesis we focus on the study of the structure of precipitation (in particular in its scaling properties), and the structure of the errors associated with radar QPE, both for ground- and space-borne radars.

In the present study, two algorithms for downscaling rainfall measurements have been analyzed and a 3D downscaling algorithm proposed. Regarding the structure of the errors, we worked on the study of the overall errors affecting the measurements of both ground- and in space-borne radars an on the error related to range in the ground-radars.

5.1. Summary

In the second chapter, we compared two classical downscaling methods (one based on a Fourier transform and the other on a wavelet decomposition). The analysis was by done first upscaling the recorded rainfall series and then downscaling back to the original high-resolution with the different methods. Then we compared the scaling characteristics of the generated high-resolution series with the original recorded series at the same resolution, in order to determine which downscaling method is better reproducing the characteristics of the original recorded series. Afterwards we performed a multifractal analysis based on the generalized fractal dimension and the multifractal spectrum to also characterize the downscaling methods from this point of view.

Afterwards, we propose a downscaling technique to generate high-resolution 3D precipitation fields from volumetric radar measurements. It is based on a three-step process: a) downscaling the first radar tilt (Plan Position Indicator) measurements with a wavelet-based algorithm, b) downscaling of the remaining tilts with a homotopy of the observed Vertical Profiles of Reflectivity, and c) transforming the polar values to a Cartesian 3D grid.

In the third chapter we characterized the errors of the ground-radar estimates. First we analyzed the errors in relation with range. The study was done through physical simulation of the radar measurement process over a high-resolution precipitation field with the radar located at different ranges. We obtained statistics of the error defined as the difference between the simulated estimates and the reference field. We also simulated the measurements of a raingauge network and compared to the radar at different ranges. In a last step in the same chapter we analyzed also the global uncertainty associated to the radar QPE comparing this estimates with a benchmark.

The concept of radar QPE ensemble, including the uncertainty in the radar measurements, is also introduced in chapter three. We generated an ensemble of radar QPE based on the error characteristics obtained in the study of the same event.

Finally, chapter four deals with the uncertainty in the measurements of spaceborne radar. We performed comparisons of the Tropical Rainfall Measuring Mission Precipitation Radar [TRMM-PR] observations against ground equipment QPE over Florida, Melbourne (USA) and over the entire continental United States using the experimental high-resolution Q2 product. The comparisons have been done over a large set of TRMM overpasses and over selected extreme events. We compared TRMM-PR with ground estimates before and after classification into rain types (from TRMM-PR variables) for a better characterization of the errors under different circumstances and for a possible extrapolation of the errors to areas not covered by ground equipment but characterized by the same rainfall type.

We also compared the precipitation estimates of the last two versions of the TRMM-PR rain profiling algorithm in order to characterize the uncertainty in the TRMM-PR estimates themselves and study the discrepancies between the different retrieval algorithms.

5.2. Results and contribution of the Thesis

In each chapter of the thesis the corresponding results have been presented. This section provides a general review of them all, and the main contributions are emphasised.

We presented a framework for comparing different downscaling methods. We analyzed two methods for rainfall downscaling applied to rainfall series, both based on modelling the scaling properties of rainfall, being the main difference between them the base of functions used to describe the variability of rainfall with scale: the first, using Fourier decomposition, and the second, using the Haar wavelet. We observed that the series downscaled using the wavalet-based method reproduce the structure of heavy rain rates better than those obtained using the Fourier-based method. Also, we have shown that, although none of the analyzed methods fully reproduce the multifractal properties of self-similarity exhibited by observed rainfall time series, the wavelet-based

does it better. Since the complexity of such a downscaling method is rather limited and not time consuming, this can be considered a very efficient tool for downscaling rainfall data.

We also presented a method to downscale radar observations and generate 3D high-resolution precipitation fields. A 2D wavelet model is used for the first radar PPI and process is complemented with a vertical homotopy of the observed Vertical Profiles of Reflectivity in order to obtain a complete 3D downscaling algorithm. This technique is able to reproduce the extreme values of the rain and, in addition, improve the correlation between the generated values in the new scales. Nevertheless it is not capable of fully recovering the field correlation of the observed fields in terms of the Fourier power spectrum slope. The vertical downscaling preserves the vertical structure of rainfall observed by the radar and allows us to increase the density of reflectivity data in the vertical.

The simulation framework proposed to characterize the errors related to radar measurements, based on simulation the physical measurement process, showed its potential in characterizing the impact of errors related to range in ground radar measurements. We performed simulations of the observations over a reference field of a ground-radar at different distances and then characterized the errors in terms of their probability distribution and spatial autocorrelation. Simulating a raingauge network we obtained a "comparison threshold" of the limit of agreement between these two instruments if the radar had been located at different distances. This can be useful when comparing real observations of these two instruments.

We also presented a methodology to characterize the total uncertainty in the radar QPE based on a relative comparison of two QPE methods (radar QPE against a benchmark) followed by probabilistic model that characterizes the differences. We studied the parameters of this model for several events. The error structure obtained has been used in the generation of ensembles through a simulation process. The ensemble corrects the bias between radar QPE and Benchmark QPE, and represents the uncertainty inherent in the radar estimates through the spread of its members. This presented approach has already been used in Schröter *et al.* (2010); Schröter *et al.* (2008) to estimate how the uncertainty in precipitation estimates propagates through a distributed hydrological model.

Combining statistical and physical validation approaches provides an opportunity for verification of spaceborne radar estimates of precipitation and for extrapolating uncertainties found in TRMM-PR estimates to regions not covered by ground equipment but with same precipitation characteristics. We compared rain rate distributions from TRMM-PR 2A25 estimates with those from ground equipment previous and after classification into rain types. The results provide a brief review of how well compare both rainfall estimates under different circumstances. Overall, we found the TRMM-PR to underestimate the rain by 4%, but also to not detect 4.5% of the rain as compared to

the Ground Validation radar estimates. But when analyzing the differences under different rainfall types we found much larger discrepancies that are, somehow compensated, in the overall comparison. We found also that the discrepancies between the TRMM-PR and the ground based pdfs of rain rates were on the same order as the discrepancies between the two TRMM-PR pdfs based on the last two PR rain retrieval algorithm versions (V5 and V6), and that the estimates of V5 agree better with the ground based than the new version (V6), specially in the regions dominated by high horizontal gradients; probably due to the changes in the attenuation correction algorithms.

5.3. Lines of future work

During the development of this thesis we have identified some aspects of the work that could be improved for future studies. Also several lines of extending the present work have been identified. They are all presented in this section.

The comparison framework for downscaling methods proposed in the first chapter could be extended for 2D precipitation fields in order to compare downscaling methods over radar QPE, for example. The 2D downscaling method proposed is applied to radar data in spherical coordinates, which implies that not all the pixels have the same area. How this affects the scaling laws should be further investigated.

In the 3D downscaling process, based on the Vertical Profiles of Reflectivity homotopy, the variability of the VPRs should be studied in order to introduce a random component in the process. This would allow us to consider the variability of rainfall in the three dimensions.

Future work in the error simulation framework should include rain type classification in the study of the distance error. For the spaceborne radar simulations the vertical resolution of the three-dimensional precipitation field used as reference might be increased due to the vertical resolution of this instrument. Also attenuation should be considered in future work. This might significantly affect the spaceborne radar estimates due to the short wavelength used in this instrument.

The statistical model described to characterize the global error does not fully describe the structure of the overall error, in particular the temporal correlation is not considered. So, future work will focus on the modelling of the space-time correlation of the errors. Stratification of the parameters depending on the characteristics of each event could also be also studied in order to extrapolate the obtained results to areas not covered by raingauges, but characterized by the same rain type.

In the study of the uncertainty associated with TRMM-PR estimations, the use of the Q2 product significantly increased the sample size of data available for comparisons compared to previous studies. This could permit classification of the data not only by rain type, but also with other parameters like topography, geographic region, etc. that will allow for a better evaluation of the algorithms and products from satellite.

References

Amitai, E., 1999: Relationships between radar properties at high elevations and surface rain rate: potential use for spaceborne rainfall measurements. *Journal of Applied Meteorology*, **38**, 321-333.

Amitai, E., X. Llort, and D. Sempere-Torres, 2006: Opportunities and challenges for evaluating precipitation estimates during GPM mission. *Meteorologische Zeitschrift*, **15**, 551-557.

——, 2009: Comparison of TRMM radar rainfall estimates with NOAA next-generation QPE. *Journal of the Meteorological Society of Japan*, **87A**, 109-119.

Amitai, E., L. Liao, X. Llort, and R. Meneghini, 2005: Accuracy verification of spaceborne radar estimates of rain rate. *The Royal Meteorological Society Atmospheric Science Letters*, **6**, 2-6.

Amitai, E., L. Liao, D. B. Wolff, D. A. Marks, and D. S. Silberstein, 2003: Challenges and proposed solutions for validation of rain rate estimates from space. Preprints, *IEEE International Geosciences and Remote Sensing Symposium*, Toulouse, France, 1966-1968.

Anagnostou, E. N. and W. F. Krajewski, 1997: Simulation of radar reflectivity fields: algorithm formulation and evaluation. *Water Resources Research*, **33**, 1419-1428.

Anagnostou, E. N., C. A. Morales, and T. Dinku, 2001: The use of TRMM precipitation radar observations in determining ground radar calibration biases. *Journal of Atmospheric and Oceanic Technology*, **18**, 616-628.

Awaka, J., T. Iguchi, and K. Okamoto, 1998: Early results on rain type classification by the Tropical Rainfall Measuring Mission (TRMM) precipitation radar. Preprints, *8th URSI Commission F Open Symposium*, Aveiro, Portugal, 143-146.

Awaka, J., T. Iguchi, H. Kumagai, and K. Okamoto, 1997: Rain type classification algorithm for TRMM Precipitation Radar. Preprints, *Internation Geosciences and Remote Sensing Symposium (IGARSS)*, Singapore, 1633-1635.

Bell, T. L., 1987: A space-time stochastic model of rainfall for satellite remote sensing studies. *Journal of Geophysical Research-Atmospheres*, **92**, 9631-9643.

Bell, T. L., A. Abdullah, R. L. Martin, and G. R. North, 1990: Sampling errors for satellite-derived tropical rainfall: Monte Carlo study using a space-time stochastic model. *Journal of Geophysical Research-Atmospheres*, **95**, 2195-2205.

Bellon, A., G. Lee, and I. Zawadzki, 2005: Error statistics of VPR corrections in stratiform precipitation. *Journal of Appplied Meteorology*, **44**, 998-1015.

Berenguer, M., 2006: Hydrological uses of meteorological radar. Validation of algorithms for rainfall estimation and forecasting, Universitat Politècnica de Catalunya, 130 pp.

Berenguer, M. and I. Zawadzki, 2008: A study of the error covariance matrix of radar rainfall estimates in stratiform rain. *Weather and Forecasting*, **23**, 1085-1101.

——, 2009: A study of the error covariance matrix of radar rainfall estimates in stratiform rain. Part II: Scale dependence. *Weather and Forecasting*, **24**, 800-811.

Berenguer, M., D. Sempere-Torres, C. Corral, and R. Sánchez-Diezma, 2006: A fuzzy logic technique for Identifying nonprecipitating echoes in radar scans. *Journal of Atmospheric and Oceanic Technology*, **23**, 1157-1180.

Berne, A., G. Delrieu, J. D. Creutin, and C. Obled, 2004: Temporal and spatial resolution of rainfall measurementsrequiered for urbam hydrology. *Journal of Hydrology* 166-179.

Bevington, P. R., 1969: *Data reduction and error analysis for the physical sciences*. McGraw-Hill, 336 pp.

Block, A., W. Vonbloh, and H. J. Schellnhuber, 1990: Efficient box-counting determination of generalized fractal dimensions. *Physical Review A*, **42**, 1869-1874.

Bolen, S. M. and V. Chandrasekar, 2003: Methodology for aligning and comparing spaceborne radar and ground-based radar observations. *Journal of Atmospheric and Oceanic Technology*, **20**, 647-659.

Borga, M., 2002: Accuracy of radar rainfall estimates for streamflow simulation. *Journal of Hydrology*, **267**, 26-39.

Borga, M., E. N. Anagnostou, and W. F. Krajewski, 1997: A simulation approach for validation of a brightband correction method. *Journal of Applied Meteorology*, **36**, 1507-1518.

Bowman, K. P., A. B. Philips, and G. R. North, 2003: Comparison of TRMM rainfall retrievals with rain gauge data from the TAO/TRITON buoy array. *Geophysical Research Letters*, **30**, 1757.

Breslin, M. C. and J. A. Belward, 1999: Fractal dimensions for rainfall time series. *Mathematics and Computers in Simulation*, **48**, 437-446.

Chandrasekar, V. and V. N. Bringi, 1987: Simulation of radar reflectivity and surface measurements of rainfall. *Journal of Atmospheric and Oceanic Technology*, **4**, 464-478.

——, 1988a: Error structure of multiparameter radar and surface measurements of rainfall. Part I: Differential reflectivity. *Journal of Atmospheric and Oceanic Technology*, **5**, 783-795.

——, 1988b: Error structure of multiparameter radar and surface measurements of rainfall. Part II: X-band attenuation. *Journal of Atmospheric and Oceanic Technology*, **5**, 796-802.

Chandrasekar, V., V. N. Bringi, N. Balakrishnan, and D. S. Zrnic, 1990: Error structure of multiparameter radar and surface measurements of rainfall. Part III: Specific differential phase. *Journal of Atmospheric and Oceanic Technology*, **7**, 621-629.

Chen, H. P., X. Sun, H. X. Chen, Z. Q. Wu, and B. H. Wang, 2004: Some problems in multifractal spectrum computation using a statistical method. *New Journal of Physics*, **6**, -.

Chhabra, A. and R. V. Jensen, 1989: Direct determination of the F(alpha) singularity spectrum. *Physical Review Letters*, **62**, 1327-1330.

Ciach, G. J., W. Krajewski, and G. Villarini, 2007: Product-error-driven uncertainty model for probabilistic quantitative precipitation estimation with NEXRAD data. *Journal of Hydrometeorology*, **8**, 1325-1347.

Ciach, G. J., W. F. Krajewski, E. N. Anagnostou, M. L. Baeck, J. A. Smith, J. R. McCollum, and A. Kruger, 1997: Radar rainfall estimation for ground validation studies of the Tropical Rainfall Measuring Mission. *Journal of Applied Meteorology*, **36**, 735-747.

Deidda, R., 2000: Rainfall downscaling in a space-time multifractal framework. *Water Resources Research*, **36**, 1779-1794.

Deidda, R., R. Benzi, and F. Siccardi, 1999: Multifractal modeling of anomalous scaling laws in rainfall. *Water Resources Research*, **35**, 1853-1867.

Deidda, R., M. G. Badas, and E. Piga, 2006a: Space-time multifractality of remotely sensed rainfall fields. *Journal of Hydrology*, **322**, 2-13.

Deidda, R., M. G. Badas, A. Seoni, and E. Piga, 2006b: A meteo-hydrological forecasting chain: performance of the downscaling and rainfall-runoff steps in a small catchment. *Advances in Geosciences*, **7**, 361-369.

Delaunay, B., 1934: Sur la sphere vide. *Bulletin of Academy of Sciences of the URSS*, **6**, 793-800.

Delrieu, G., J. D. Creutin, and H. Andrieu, 1995: Simulation of radar mountain returns using a digitalized terrain model. *Journal of Atmosospheric and Oceanic Technology*, **12**, 1038-1049.

DeMoss, J. D. and K. P. Bowman, 2007: Changes in TRMM rainfall due to the orbit boost estimated from buoy rain gauge data. *Journal of Atmospheric and Oceanic Technology*, **24**, 1598-1607.

Doviak, R. J. and D. S. Zrnic, 1992: *Doppler radar and weather observations.* 2dn ed. Academic Press, 562 pp.

Durden, S. L., E. Im, Z. S. Haddad, and L. Li, 2003: Comparisons of TRMM precipitation radar and airbone radar data. *Jorunal of Applied Meteorology*, **42**, 769-774.

Fabry, F., 1996: On the determination of scale ranges for precipitation fields. *Journal of Geophysical Research-Atmospheres*, **101**, 12819-12826.

Ferraris, L., S. Gabellani, N. Rebora, and A. Provenzale, 2003a: A comparison of stochastic models for spatial rainfall downscaling. *Water Resources Research*, **39**, 1368-1383.

Ferraris, L., S. Gabellani, U. Parodi, J. von Hardenberg, and A. Provenzale, 2003b: Revisiting multifractality in rainfall fields. *Journal of Hydrometeorology*, **4**, 544-551.

Fisher, B. L., 2004: Climatological validation of TRMM TMI and PR montly rain products over Oklahoma. *Journal of Applied Meteorology*, **43**, 519-535.

Foufoula-Georgiou, E. and P. Kumar, Eds., 1995: *Wavelets in geophysics.* Academic Press, 373 pp.

Franco, M., 2008: Estimación cuantitativa de la lluvia mediante radar meteorológico. Corrección del error asociado a la variación vertical de la reflectividad, Universitat Politècnica de Catalunya, 254 pp.

Gebremichael, M. and W. F. Krajewski, 2004: Assessment of the statistical characterization of small-scale rainfall variability from radar: analysis of TRMM Ground Validation datasets. *Journal of Applied Meteorology*, **43**, 1180-1199.

——, 2005: Effect of temporal sampling on inferred rainfall spatial statistics. *Journal of Applied Meteorology*, **44**, 1626-1633.

Germann, U., M. Berenguer, D. Sempere-Torres, and G. Salvadè, 2006: Ensemble radar precipitation estimation - a new topic on the radar horizon. *Proceedings of the 4th European Conference on Radar in Hydology and Meteorology*, 559-562.

Germann, U., M. Berenguer, D. Sempere-Torres, and M. Zappa, 2009: REAL - Ensemble radar precipitation estimation for hydrology in a mountainous region. *Quaterly Journal of the Royal Meteorologycal Society*, **135**, 445-456.

Gupta, V. K., C. S. L., and T. M. Over, 1996: On scaling exponents of spatial peak flows from rainfall and river network geometry. *Journal of Hydrology*, **187**, 81-104.

Haar, A., 1910: Zur Theorie der orthogonalen Funktionensysteme. *Mathematische Annalen*, **69**, 331-371.

Habib, E. and W. F. Krajewski, 2002: Uncertainty analysis of the TRMM Ground-Validation radar-rainfall products: application to the TEFLUN-B field campaign. *Journal of Applied Meteorology*, **41**, 558-572.

Halsey, T. C., M. H. Jensen, L. P. Kadanoff, I. Procaccia, and B. I. Shraiman, 1986: Fractal measures and their singularities - the characterization of strange sets. *Physical Review A*, **33**, 1141-1151.

Harris, D. and E. Foufoula-Georgiou, 2001: Subgrid variability and stochastic downscaling of modeled clouds: Effects on radiative transfer computations for rainfall retrieval. *Journal of Geophysical Research-Atmospheres*, **106**, 10349–10362.

Harris, D., A. W. Seed, M. Menabde, and G. Austin, 1997: Factors affecting multiscaling analysis of rainfall time series. *Nonlinear Processes in Geophysics*, **4**, 137-155.

Hentschel, H. G. E. and I. Procaccia, 1983: The infinite number of generalized dimensions of fractals and strange attractors. *Physica D*, **8**, 435-444.

Hitschfeld, W. and J. Bordan, 1954: Errors inherent in the radar measurement of rainfall at attenuating wavelenghts. *Journal of Atmospheric Sciences*, **11**, 58-67.

Hou, A. Y., G. Skofronick-Jackson, C. Kummerow, and J. M. Shepherd, 2008: Global Precipitation Measurement. *Precipitation: Advances in Measurement, Estimation and Prediction*, S. Michaelides, Ed., Springer-Verlag, 131-169.

Hubbert, J. C., M. Dixon, and S. M. Ellis, 2009a: Weather radar ground clutter. Part II: real-time identification and filtering. *Journal of Atmosospheric and Oceanic Technology*, **26**, 1181-1197.

Hubbert, J. C., M. Dixon, S. M. Ellis, and G. Meymaris, 2009b: Weather radar ground clutter. Part I: identification, modelling, and simulation. *Journal of Atmosospheric and Oceanic Technology*, **26**, 1165-1180.

Iguchi, T., T. Kozu, R. Meneghini, J. Awaka, and K. Okamoto, 2000: Rain-profiling algorithm for the TRMM Precipitation Radar. *Journal of Applied Meteorology*, **39**, 2038-2052.

Japan-Aerospace-Exploration-Agency, 2005: *Tropical Rainfall Measuring Mission (TRMM), Precipitation Radar algorithm instruction manual for version 6*. 180 pp.

——, 2006: *TRMM data users Handbook*. 3rd ed. Earth Observation Center, 231 pp.

Joss, J. and A. Waldvogel, 1990: Precipitation measurement and hydrology. *Radar in Meteorology*, D. Atlas, Ed., American Meteorological Society, 577-606.

Kozu, T. and T. Iguchi, 1999: Nonuniform beamfilling correction for spaceborne radar rainfall measurement: Impacts from TOGA COARE radar data analysis. *Journal of Atmospheric and Oceanic Technology*, **16**, 1722-1735.

Krajewski, W. and K. Georgakakos, 1985: Synthesis of radar rainfall data. *Water Resources Research*, **21**, 764-768.

Krajewski, W. F. and G. J. Ciach, 2004: Towards operational probabilistic quantitative precipitation estimation using weather radar. Preprints, *6th International Symposium on Hydrologycal Applications of Weather Radar*, Melbourne, Australia.

Kucera, P. A., W. F. Krajewski, and C. B. Young, 2004: Radar beam occultation studies using GIS and DEM technology: An example study of Guam. *Journal of Atmospheric and Oceanic Technology*, **21**, 995-1006.

Lanza, L. G., J. A. Ramírez, and E. Todini, 2001: Stochastic rainfall interpolation and downscaling. *Hydrology and Earth System Sciences*, **5**, 139-143.

Lee, G., A. Seed, and I. Zawadzki, 2007: Modeling the variability of drop size distributions in space and time. *Journal of Applied Meteorology and Climatology*, **46**, 742-756.

Liao, L., R. Meneghini, and T. Iguchi, 2001: Comparisons of rain rate and reflectivity factor derived from the TRMM precipitation radar and the WSR-88D over the Melbourne, Florida, site. *Journal of Atmospheric and Oceanic Technology*, **18**, 1959-1974.

Lima, M. I. P., 1998: Multifractals and the temporal structure of rainfall, Wageningen University, 225 pp.

Llort, X., M. Berenguer, M. Franco, R. Sánchez-Diezma, and D. Sempere-Torres, 2006: 3D downscaling model for radar-based precipitation fields. *Meteorologische Zeitschrift*, **15**, 505-512.

Lovejoy, S. and B. B. Mandelbrot, 1985: Fractal properties of rain, and a fractal model. *Tellus*, **37A**, 209-232.

Lovejoy, S. and D. Schertzer, 1995: Multifractals and Rain. *New uncertainty concepts in hydrology and hydrological modelling*, A. W. Kundzewicz, Ed., Cambridge press, 62-103.

Lovejoy, S., D. Schertzer, and V. C. Allaire, 2008: The remarkable wide range spatial scaling of TRMM precipitation. *Atmospheric Research*, **90**, 10-32.

Mallat, S. G., 1989: A theory for multiresolution signal decomposition - the Wavelet representation. *IEEE Transactions on Pattern Analysis and Machine Intelligence*, **11**, 674-693.

Mandelbrot, B. B., 1982: *The fractal geometry of Nature*. Freeman, 468 pp.

Marshall, J. S. and W. M. Palmer, 1948: The distribution of raindrops with size. *Journal of Meteorology*, **5**, 165-166.

Menabde, M., A. W. Seed, D. Harris, and G. Austin, 1999: Multiaffine random field model of rainfall. *Water Resources Research*, **35**, 509-514.

Menabde, M., D. Harris, A. Seed, G. Austin, and D. Stow, 1997: Multiscaling properties of rainfall and bounded random cascades. *Water Resources Research*, **33**, 2823-2830.

Meneghini, R., T. Kozu, H. Kumagai, and W. C. Boncyk, 1992: A study of rain estimation methods from space using dual-wavelength radar measurements at near-nadir incidence over ocean. *Journal of Atmosospheric and Oceanic Technology*, **9**, 364-382.

Meneghini, R., J. A. Jones, T. Iguchi, K. Okamoto, and J. Kwiatkowski, 2004: A hybrid surface reference technique and Its application to the TRMM Precipitation Radar. *Journal of Atmospheric and Oceanic Technology*, **21**, 1645-1658.

Meneghini, R., T. Iguchi, T. Kozu, L. Liao, K. i. Okamoto, J. A. Jones, and J. Kwiatkowski, 2000: Use of the surface reference technique for path attenuation estimates from the TRMM Precipitation Radar. *Journal of Applied Meteorology*, **39**, 2053-2070.

Nash, J. E. and J. V. Sutcliffe, 1970: The river flow forecasting through conceptual models, 1. Discussion of principles. *Journal of Hydrology*, **10**, 282-290.

Nikolopoulos, E. I., A. Kruger, W. F. Krajewski, C. R. Williams, and K. S. Gage, 2008: Comparative rainfall data analysis from two vertically pointing radars, an optical disdrometer, and a rain gauge. *Nonlinear Processes in Geophysics*, **15**, 987-997.

Pegram, G. G. S. and A. N. Clothier, 2001a: High resolution space-time modelling of rainfall: the "String of Beads" model. *Journal of Hydrology*, **241**, 26-41.

——, 2001b: Downscaling rainfields in space and time, using the String of Beads model in time series mode. *Hydrology and Earth System Sciences*, **5**, 175-186.

Pegram, G. G. S., X. Llort, and D. Sempere-Torres, 2010: Radar-rainfall: Separating signal and noise fields to generate meaningful ensembles. *Atmospheric Research*, **(submitted)**, -.

Perica, S. and E. Foufoula-Georgiou, 1996a: Model for multiscale disaggregation of spatial rainfall based on coupling meteorological and scaling descriptions. *Journal of Geophysical Research-Atmospheres*, **101**, 26347-26361.

——, 1996b: Linkage of scaling and thermodynamic parameters of rainfall: Results from mid-latitude mesoscale convective systems. *Journal of Geophysical Research-Atmospheres*, **101**, 7431-7448.

Probert-Jones, J. R., 1962: The radar equation in meteorology. *Quaterly Journal of the Royal Meteorologycal Society*, **88**, 485-495.

Rebora, N., L. Ferraris, J. Hardenberg, and A. Provenzale, 2006: RainFARM: Rainfall dowscaling by a filtered autoregressive model. *Journal of Hydrometeorology*, **7**, 724-738.

Rodriguez-Iturbe, I. and P. S. Eagleson, 1987: Mathematical-models of rainstorm events in space and time. *Water Resources Research*, **23**, 181-190.

Rodriguez-Iturbe, I., D. R. Cox, and P. S. Eagleson, 1986: Spatial modelling of total storm rainfall. *Proceedings of the Royal Society A*, **403**, 27-50.

Rosenfeld, D., D. B. Wolff, and E. Amitai, 1994: The window probability matching method for rainfall measurements with radar. *Journal of Applied Meteorology*, **33**, 682-693.

Rosenfeld, D., E. Amitai, and D. B. Wolff, 1995: Classification of rain regimes by the three-dimensional properties of reflectivity fields. *Journal of Applied Meteorology*, **34**, 198-211.

Sánchez-Diezma, R., 2001: Optimización de la medida de lluvia por radar meteorológico para su aplicación hidrológica., Universitat Politècnica de Catalunya, 313 pp.

Sánchez-Diezma, R., I. Zawadzki, and D. Sempere-Torres, 2000: Identification of the bright band through the analysis of volumetric radar data. *Journal of Geophysical Research-Atmospheres*, **105**, 2225-2236.

Sánchez-Diezma, R., D. Sempere-Torres, G. Delrieu, and I. Zawadzki, 2001a: An Improved Methodology for ground clutter substitution based on a pre-classification of precipitation types. Preprints, *30th International Conference on Radar Meteorology*, Munich, Germany, 271-273.

Sánchez-Diezma, R., D. Sempere-Torres, I. Zawadzki, and J. D. Creutin, 2001b: Hydrological assessment of factors affecting the accuracy of weather radar measurements of rain. Preprints, *5th International Symposium on Hydrological Applications of Weather Radar*, Kyoto, Japan, 433-438.

Schröter, K., X. Llort, C. A. Velasco-Forero, M. Ostrowski, and D. Sempere-Torres, 2010: Implications of radar rainfall estimates uncertainty on distributed hydrological model predictions. *Atmospheric Research*, **(submitted)**, -.

Schröter, K., X. Llort, C. A. Velasco-Forero, D. Muschalla, M. Ostrowski, and D. Sempere-Torres, 2008: Accounting for uncertain radar rainfall estimates in distributed hydrological modelling. Preprints, *Internationa Symposium Weather Radar and Hydrology*, Grenoble, France.

Sempere-Torres, D., J. M. Porrà, and J. D. Creutin, 1994: A general formulation for raindrop size distribution. *Journal of Applied Meteorology*, **33**.

Sempere-Torres, D., C. Corral, J. Raso, and P. Malgrat, 1999: Use of weather radar for combined sewer overflows monitoring and control. *Journal of Environmental Engineering*, **125**, 372-380.

Serra, Y. L. and M. J. McPhaden, 2003: Multiple time- and space-scale comparisons of ATLAS buoy raingauge measurements with TRMM satellite precipitation measurements. *Journal of Applied Meteorology*, **42**, 1045-1059.

Sharif, H. O., F. L. Ogden, W. F. Krajewski, and M. Xue, 2002: Numerical simulations of radar rainfall error propagation. *Water Resources Research*, **38**, 1140-1153.

——, 2004: Statistical analysis of radar rainfall error propagation. *Journal of Hydrometeorology*, **5**, 199-212.

Sheppard, B. E., 1990: The measurement of raindrop size distributions using a small Doppler radar. *Journal of Atmosospheric and Oceanic Technology*, **7**, 225-268.

Sheppard, B. E. and P. I. Joe, 1994: Comparison of raindrop size distribution measurements by a Joss-Waldvogel disdrometer, a PMS 2DG spectrometer, and a POSS Doppler radar. *Journal of Atmosospheric and Oceanic Technology*, **11**, 874-887.

Shin, D.-B. and L. S. Chiu, 2008: Effects of TRMM boost on oceanic rainfall estimates based on microwave emission brightness temperature histograms (METH). *Journal of Atmospheric and Oceanic Technology*, **25**, 1888-1893.

Simpson, J., R. F. Adler, and G. R. North, 1988: A proposed Tropical Rainfall Measuring Mission (TRMM) Satellite. *Bulletin of the American Meteorological Society*, **69**, 278-295.

Sivakumar, B., 2001: Is a chaotic multi-fractal approach for rainfall possible? *Hydrological Processes*, **15**, 943-955.

Trapp, R. J. and C. A. Doswell, 2000: Radar data objective analysis. *Journal of Atmosospheric and Oceanic Technology*, **17**, 105-120.

Uijlenhoet, R. and A. Berne, 2008: Stochastic simulation experiment to assess radar rainfall retrieval uncertatinties associated with attenuation and its correction. *Hydrology and Earth System Sciences*, **12**, 587-601.

Vasiloff, S. V., D.-J. Seo, K. W. Howard, J. Zhang, D. H. Kitzmiller, M. G. Mullusky, W. F. Krajewski, E. A. Brandes, R. M. Rabin, D. S. Berkowitz, H. E. Brooks, J. A. McGinley, R. J. Kuligowski, and B. G. Brown, 2007: Improving QPE and very short term QPF: An initiative for a community-wide integrated approach. *Bulletin of the American Meteorological Society*, **88**, 1899-1911.

Velasco-Forero, C. A., 2009: Optimal estimation of rainfall fields for hydrological purposes in real time, Universitat Politècnica de Catalunya, 128 pp.

Velasco-Forero, C. A., D. Sempere-Torres, E. F. Cassiraga, and J. J. Gómez-Hernández, 2009: A non-parametric automatic blending methodology to estimate rainfall fields from rain gauge and radar data. *Advances in Water Resources*, **7**, 986-1002.

Venugopal, V., E. Foufoula-Georgiou, and V. Sapozhnikov, 1999: A space-time downscaling model for rainfall. *Journal of Geophysical Research-Atmospheres*, **104**, 19705-19721.

Willems, P., 2001: A spatial rainfall generator for small spatial scales. *Journal of Hydrology*, **252**, 126-144.

Wilson, J. W. and E. A. Brandes, 1979: Radar measurement of rainfall - A summary. *Butlletin of the American Meteorological Society*, **60**, 1048-1979.

Wolff, D. B., D. A. Marks, E. Amitai, D. S. Silberstein, B. L. Fisher, A. Tokay, J. Wang, and J. L. Pippitt, 2005: Ground Validation for the Tropical Rainfall Measuring Mission (TRMM). *Journal of Atmospheric and Oceanic Technology*, **22**, 365-380.

Zawadzki, I., 1973: Statistical properties of precipitation patterns. *Jorunal of Applied Meteorology*, **12**, 459-472.

——, 1984: Factors affecting the precision of radar measurement of rain. Preprints, *22th Conference on Radar Meteorology*, Zurich, Switzerland, 251-256.

——, 1987: Fractal structure and exponential decorrelation in rain. *Journal of Geophysical Research-Atmospheres*, **92**, 9586-9590.

Zawadzki, I. and A. Bellon, 2003: Error statistics of VPR corrections in stratiform precipitation. Preprints, *31st Conference on Radar Meteorology*, Seattle (WA), EUA, 225-228.

Zhang, L., D. Lu, S. Duan, and J. Liu, 2004: Small-scale rain nonuniformity and its effect on evaluation of nonuniform beam-filling error for spaceborne radar rain measurement. *Journal of Atmospheric and Oceanic Technology*, **21**, 1190-1197.